Universidad
Carlos III de Madrid
www.uc3m.es

Tesis Doctoral

CAPILLARY BREAKUP OF STRETCHED LIQUID JETS

Autor
Paula Andrea Consoli Lizzi

Director
Alejandro Sevilla Santiago
Co-director
Wilfried Coenen

DEPARTAMENTO DE INGENIERÍA TÉRMICA Y DE FLUIDOS

Leganés, Octubre 2016

Universidad
Carlos III de Madrid
www.uc3m.es

Tesis doctoral

CAPILLARY BREAKUP OF STRETCHED LIQUID JETS

Autor: Paula Andrea Consoli Lizzi

Director de Tesis: Alejandro Sevilla Santiago

Co-director de Tesis: Wilfried Coenen

Firma del Tribunal Calificador:

Firma

Presidente: Dr. Jesús Carlos Martínez Bazán

Secretario: Dr. Francisco Javier Rodríguez Rodríguez

Vocal: Dr. Francisco Javier García García

Calificación:

Leganés, 28 de Octubre de 2016

A la dignidad de los becarios

y a la Universidad entendida como empresa.

DEPARTAMENTO DE INGENIERÍA TÉRMICA Y DE FLUIDOS
Escuela Politécnica Superior

CAPILLARY BREAKUP OF STRETCHED LIQUID JETS

Autor
Paula Andrea Consoli Lizzi

Director de Tesis
Alejandro Sevilla Santiago
Co-director de Tesis
Wilfried Coenen

Leganés, Octubre 2016

In ironing out the disasters of Reality, Eternity rules out the triumphs as well. It is in meeting the great tests that mankind can most successfully rise to great heights. Out of danger and restless insecurity comes the force that pushes mankind to newer and loftier conquests. Can you understand that? Can you understand that in averting the pitfalls and miseries that beset man, Eternity prevents men from finding their own bitter and better solutions, the real solutions that come from conquering difficulty, not avoiding it.

Noys Lambent
The End of Eternity

Agradecimientos

A Alejandro que se ha esforzado en transmitirme sus admirables cualidades como investigador y ha sido un motivador insuperable. A Wil que como buen co-director supo tomar las riendas cuando hizo falta. Al Dr. Rodríguez, gran científico mejor persona, que con sus conversaciones amenas ha inspirado a más de uno a hacer ciencia. A Matías que me empujó a emprender este Doctorado. A Helio y Javi que me han enseñado sus técnicas de trabajo en el laboratorio. A Sonsoles que ha colaborado en la campaña experimental.
Gracias por hacer posible esta tesis.

A Mamá y Papá, que siempre han sido incondicionales. A Euge, con quien sé que puedo contar para toda la vida ("los hermanos sean unidos porque esa es la ley primera"). A la Tía Teresa, que ha desempeñado a la perfección su papel de hada madrina. A esas amigas de toda una vida que no necesito nombrar, y a Bruno y Davan a quienes no quiero menos. Al Dr. Cutz, el amigo que no imaginé que iba a encontrar del otro lado del océano. A Dani Malo y Alberto, quienes con un té en la mano son casi imposibles de distinguir de unos argentinos con un mate. A Dani Coches que se propuso sacarme siempre una sonrisa. A Jesús que ha sido un compañero de piso fantástico. A Miguel, Ana, Nano, Juanillo y los compañeros del departamento con quienes he compartido la relación amor–odio con la tesis y los ratos libres que quedaban entre medio. Gracias por evitar que esta doctoranda se derrumbara ante semejante tarea.

Abstract

It is well known that the Plateau-Rayleigh instability is responsible for the break-up of a liquid jet into droplets. In this process, small perturbations grow as they are convected by the jet, eventually leading to its break-up. In this thesis we investigate, both experimentally and numerically, how the stretching action of gravity affects the capillary instability mechanism. Our study focuses on liquid jets issuing from a needle into a stagnant air atmosphere, at a constant flow rate that is slightly larger than the critical flow rate at which the jet transitions from jetting to dripping. This results in a highly non-parallel meniscus region near the injector. Our main aim is to understand the role that the latter plays in the amplitude of disturbances, and to characterize the frequency of the most amplified disturbances and the resulting break-up length. The control parameters of interest in this study are the viscosity of the liquid, the diameter of the injector, and the liquid flow rate.

In the experimental campaign, we distinguish between natural and controlled break-up processes. In a natural break-up experiment, the disturbances are essentially noise coming from the ambient and the experimental facility. The disturbances are only controlled in a passive sense by designing the experimental facility to minimize their amplitude, and a wide range of frequencies are thus expected to contribute to the energy spectrum of the noise. In a controlled break-up experiment, in contrast, the disturbance is provided to the flow by means of a harmonic mechanical forcing, which induces fluctuations of the axial velocity of known amplitude and frequency at the injector outlet.
In the natural break-up experiments, we focus our attention on describing the intact length and the most amplified frequency as functions of the three control

parameters. In the controlled break-up experiments, the stimulation frequency and amplitude are swept over different flow configurations, observing a transition from chaotic to periodic break-up, and revealing the existence of a new oscillatory dripping regime under certain conditions when the amplitude of disturbances is large enough.

From the theoretical point of view, we describe the dynamics of the jet with the leading order one-dimensional mass and momentum conservation equations. The classical quasi-parallel stability theory is not valid to study the jets considered in this Thesis due to the strong axial stretching in the region near the injector outlet. We therefore propose a novel linear global frequency response analysis which, in contrast with local theory, does not make assumptions about the shape of disturbances beyond the small amplitude hypothesis. From the physical point of view, this approach reveals that the meniscus region selectively filters the outlet disturbances, providing an optimal frequency responsible for the break-up of the jet downstream. However, the linearized description is not valid neither in the final stages before break-up nor in jets subjected to large-amplitude forcing. Therefore, the nonlinear stability analysis is also addressed herein. In this approach, the evolution of the jet is obtained by numerically integrating the fully nonlinear one-dimensional conservation equations, enabling us to accurately predict the break-up length and confirming the delay in the growth of capillary disturbances due to the presence of the highly-stretched meniscus region near the injector.

Resumen

Es bien conocido que la inestabilidad de Plateau–Rayleigh es responsable de la rotura en gotas de un chorro líquido. En este proceso, pequeñas perturbaciones crecen mientras son advectadas por el flujo, hasta que se hacen lo suficientemente grandes como para provocar la rotura del chorro. En esta tesis se investiga experimental y numéricamente el efecto del estiramiento gravitatorio sobre la rotura de chorros. El estudio se centra en chorros líquidos que salen de un inyector cilíndrico a una atmósfera en reposo, con un caudal ligeramente mayor que el crítico en el que ocurre la transición de chorro a goteo. En estas condiciones, el menisco que aparece cerca del inyector es altamente no paralelo, siendo uno de los objetivos fundamentales del trabajo comprender el papel que éste desempeña en la amplitud de las perturbaciones, y caracterizar tanto la frecuencia de las perturbaciones más amplificadas como la longitud intacta resultante.

La campaña experimental se divide en dos casos: rotura natural y rotura forzada. En los experimentos de rotura natural, las perturbaciones se deben al ruido ambiente y de la instalación experimental. Las perturbaciones sólo se controlan pasivamente, diseñando la instalación de manera que su amplitud sea lo menor posible, y se tiene un rango amplio de frecuencias en el espectro del ruido. En un experimento de rotura controlada, por el contrario, las perturbaciones se imponen al flujo en forma de un forzado mecánico armónico, que se manifiesta en fluctuaciones de la velocidad axial media de amplitud y frecuencia conocidas a la salida del inyector.
En los experimentos de rotura natural, el objetivo principal es describir la longitud intacta y la frecuencia más amplificada en función de los tres parámetros de

control. En los experimentos de rotura controlada, la frecuencia y la amplitud de la estimulación se varían para distintas configuraciones del flujo, observando una transición de rotura caótica a periódica, y revelando la existencia de un régimen de goteo oscilante bajo ciertas condiciones cuando la amplitud de las perturbaciones es suficientemente grande.

Desde el punto de vista teórico, se describe la dinámica del chorro mediante las ecuaciones unidimensionales de orden principal de conservación de masa y cantidad de movimiento. La teoría de estabilidad casi-paralela no es válida para estudiar los chorros considerados en el presente trabajo debido al fuerte estiramiento axial que existe en la región cercana al inyector. Por ello proponemos un novedoso análisis lineal global de respuesta en frecuencia, que en contraste con la teoría local no hace hipótesis acerca de la forma espacial de las perturbaciones excepto su pequeña amplitud. Desde el punto de vista físico, este análisis revela que el menisco filtra selectivamente las perturbaciones que existen a la salida, proporcionando una frecuencia óptima responsable de la rotura del chorro aguas abajo. Sin embargo, la teoría lineal no es válida ni en las etapas finales previas a la rotura ni en el caso de chorros sujetos a forzado de gran amplitud. Por ello, abordamos el problema del análisis de estabilidad no lineal, en el cual la evolución del chorro se obtiene integrando las ecuaciones completas no lineales del modelo unidimensional, lo que permite predecir con precisión la longitud de rotura, y confirmando el retardo en el crecimiento de las perturbaciones en la región cercana al inyector.

Contents

CHAPTER

ONE

Introduction and theoretical background

The break-up of a liquid jet into droplets has attracted the attention of many scientists and engineers during the last centuries. This phenomenon is widely encountered in daily life, whether in the form of a thread of honey falling downwards by its own weight or in a jet of tap water falling into a sink, and also in industrial applications. For instance, drop break-up from jets is important in the technological processes of atomization, ink jet printing, fuel injection, particle sorting, drug delivery systems and manufacturing of microcapsules (see Basaran, 2002; Utada *et al.*, 2007; Kaminski *et al.*, 2016 and references therein). Small drops can be generated from streched jets resorting to techniques such as flow focusing (Gañán-Calvo, 1998), electrospinning (Doshi & Reneker, 1995), fiber spinning (Pearson & Matovich, 1969) and gravitational stretching, the latter being the simplest of all and the subject of this Thesis.

The break-up phenomenon is commonly caused by small external disturbances which grow spatially due to the capillary instability originally described by Rayleigh (1878). The break-up of jets can also be induced by other mechanisms, like aerodynamic forces acting at the jet-air interface if the relative velocity is large enough (Sterling & Sleicher, 1975), or nonlinear travelling waves of kinematic nature caused by fluctuations in the flow rate (Meier *et al.*, 1998). In the case of the capillary instability, the growth rate of the perturbations is determined by the opposite effects of the axial and radial curvatures of the interface (Savart, 1833; Plateau, 1873). The break-up is driven by surface tension, and is opposed either by viscosity in the case of highly viscous fluids, or by inertia in the case of low-viscosity fluids. Stretched jets have longer associated break-up

lengths than liquid cylinders, but the stabilizing role of axial stretching has not been studied in detail up to date.

It was Rayleigh (1878) who developed the mathematical theory which accounts for the growth of capillary disturbances, identifying the most unstable frequency responsible for the break-up of a liquid cylinder into drops, and since then the stability of a variety of jet configurations has been investigated resorting to different approaches. An excellent review of the knowledge of the physics of liquid jets is covered by Eggers & Villermaux (2008).

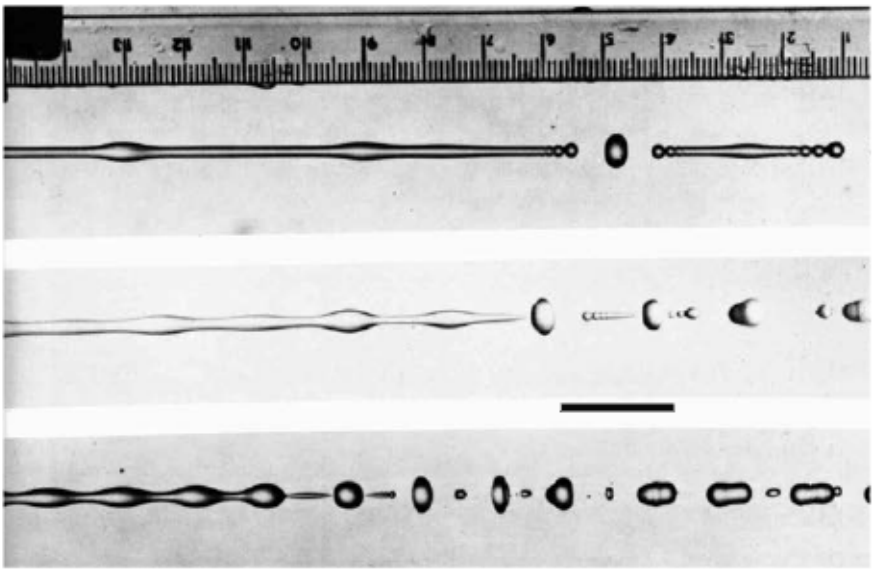

Figure 1.1: Capillary instability of a liquid jet. Water forced from a 4 mm tube is perturbed at various frequencies by a loudspeaker. The wavelength is 42, 12.5 and 4.6 diameters, the latter being nearly Rayleigh's value for maximum growth rate. The top two photographs show secondary swellings between the primary crests. Rutland & Jameson, extracted from An Album Of Fluid Motion by Van Dyke (1982).

1.1 Historical evolution of the study of capillary instability of jets

The theoretical approach to the capillary instability of jets begins with the study of the evolution of disturbances on a liquid cylinder by Rayleigh (1878), who introduced the method of normal modes. His temporal analysis revealed that axisymmetric disturbances with a wavelength greater than the circumference of the cylinder are linearly unstable and grow exponentially in time, as illustrated in Figure 1.1. This theory correctly describes the stability of jets within a range of velocities commonly referred to as the Rayleigh regime in the atomization literature (Lin & Reitz, 1998), as confirmed by many experimental studies in the past (Donnelly & Glaberson, 1966; Chauhan *et al.*, 2002; González & García, 2009).

The temporal analysis was later applied to extending cylinders by Tomotika (1936), whose work was revised by Mikami *et al.* (1975) and extended by Frankel & Weihs (1985) to include the effects of liquid inertia, and revealed that the growth of disturbances in elongational flows does not exhibit a simple exponential time dependence.

Regarding the application of the modal analysis to jets, it was pointed out by Keller *et al.* (1972) that since perturbations grow with distance, their evolution should be studied resorting to a spatial stability analysis instead of a temporal one. Indeed, the spatial analysis is the correct approach in the case of jets with velocities of the order of the capillary velocity, and is able to capture normal modes that do not arise from a temporal analysis. These spatial modes, along with the temporal dominant and subdominant capillary modes and hydrodynamic modes, have been described with detail by Guerrero *et al.* (2012).

Also of large importance to stability calculations is the development of new simple models to mathematically describe the dynamics of slender jets. García & Castellanos (1994) developed the one-dimensional equations governing the velocity and the radius of the jet that are obtained after expanding in Taylor's series in the radial direction and truncating the Navier–Stokes equations

at different orders, improving the previous inviscid formulation derived by Lee (1974). These models have been used to perform stability analyses of jets for a long time, yielding results which were recently compared by Guerrero *et al.* (2016). In particular, the leading-order equations developed also independently by Eggers & Dupont (1994), precisely describe droplet break-up for a free jet and a hanging drop, and have been widely used (see e.g. Eggers, 1993; Rubio-Rubio *et al.*, 2013 among many others) since they provide ease of computation while their solutions deviate only slightly from Navier–Stokes simulations (Ambravaneswaran *et al.*, 2002).

Both temporal and spatial analyses can be locally applied when the basic flow evolves slowly compared to the characteristic scales of perturbations. Senchenko & Bohr (2005) used this approximation to study the asymptotic stability of a viscous thread far from the injector, concluding that the spatial growth is proportional to $\exp(z^{1/8})$, where z is the dimensionless distance to the injector. The stability of jets stretched by gravity as a function of the control parameters was numerically studied using local stability theory by Amini *et al.* (2013) and Javadi *et al.* (2013), while experimental observations of the natural break-up by Nonnenmacher & Piesche (2004) and Javadi *et al.* (2013) measured the intact length and related it to the initial amplitude of disturbances. The effect of gravity on the stability of jets was also experimentally studied by Cheong & Howes (2004).

These classical analyses are limited by the failure to capture short-term characteristics and by making assumptions on the perturbation shape. A more powerful approach oriented to obtain the response of the equations governing the disturbance dynamics to input variables, as explained for instance by Schmid (2007) and Bagheri *et al.* (2009), can account for the stability of fully non-parallel flows.

Also, a linear analysis fails in describing the behavior of the jet close to break-up, as pointed out by Eggers (1997) for different surface tension driven flows. Non-linear wave interaction and the formation of drops and satellites observed in experiments (Rutland & Jameson, 1971; Chaudhary & Maxworthy, 1980*a*,*b*)

are in agreement with weakly nonlinear analyses where perturbation theory is carried to higher order in the amplitude of disturbances (Yuen, 1968; Chaudhary & Redekopp, 1980) as well as with integration of the fully nonlinear governing equations (Mansour & Lundgren, 1990). Chuech & Yan (2006) showed that a nonlinear description predicts longer intact lengths and slower growth of disturbances when compared to its linear counterpart. The numerical model by Furlani & Hanchak (2010), consisting of the integration of one-dimensional equations using the method of lines, is a good example of a nonlinear approach for predicting drop generation in the context of printing applications.

To validate these theories, a number of forcing techniques have been developed in the past to control the imposed disturbances and the subsequent break-up of capillary jets. The break-up can be induced by means of radius modulation, velocity modulation or jet vibration, their equivalences analyzed by Moallemi & Mehravan (2016). To mention some examples, experimental work where the break-up is controlled resorts to electrohydrodynamic (González & García, 2009), thermocapillary (Hanchak & Furlani, 2010), or other physical surface stimulation, or relies on pressure fluctuations induced by a moving piston (Meier *et al.*, 1992) or a piezoelectric transducer (Dong *et al.*, 2006). In addition to being a useful tool to validate stability analyses (Bogy & Talke, 1984), some of these forcing techniques can be easily adapted for applications involving drop-on-demand such as ink-jet printing. In particular, thorough experimental descriptions of the generation and measurement of the initial amplitude of disturbances and the intact length of jets are included in the works of Meier *et al.* (1992), Kalaaji *et al.* (2003) and García *et al.* (2014).

1.2 Linear stability analysis of capillary jets

A linear stability analysis describes the evolution of small disturbances. The fluid field φ is accordingly decomposed into a steady base flow plus $\mathcal{O}(\epsilon)$ distur-

bances, $\varphi(z,t) = \varphi_0(z) + \epsilon\varphi_1(z,t)$. Moreover, although unable to quantitatively describe the nonlinear behavior before break-up, it qualitatively accounts for the physical mechanisms in all the stages of the growth of perturbations (Lin & Reitz, 1998).

In this section, the linear approaches to the stability of liquid jets are briefly reviewed. In the existing literature, the evolution of disturbances on a liquid cylinder has been addressed with the method of normal modes in the form of a temporal analysis. This approach is suitable for parallel jets, although a spatial analysis reflects better the fact that in jets issuing from a nozzle disturbances evolve in space rather than in time. Similar techniques have been extended to quasi-parallel jets performing a local analysis, where the growth of perturbations is posed on a co-moving frame under the assumption that the characteristic length at which the flow varies in space is much larger than the wavelength of perturbations. For the first time, in the present Thesis we develop a linear global approach to properly account for the fully non-parallel flow in the meniscus region of gravitationally stretched liquid jets.

The *method of normal modes* has been widely used for performing stability analyses. It consits in perturbing and linearizing the governing equations around a steady solution, and assuming that the perturbations can be decomposed into independent wave-like Fourier modes, characterized by their frequency ω and wavenumber $k = 2\pi/\lambda$, where λ is the wavelength. Applying these assumptions to the linearized conservation equations, a dispersion relation $D(\omega, k) = 0$ is obtained that is only satisfied by certain frequency–wavenumber pairs of values that constitute the normal modes in the form of travelling waves of phase velocity ω/k and group velocity $\mathrm{d}\omega/\mathrm{d}k$. Rayleigh (1878) pioneered the application of this method to study the stability of an inviscid liquid cylinder. In particular, he used a *temporal stability analysis*, where it is assumed that the amplitude of these waves evolves exponentially in time, $(h_1, u_1) \propto e^{\omega t}$, where h_1 and u_1 are the perturbed radius and speed of the jet and ω is a complex number. Describing the dynamics of the jet resorting to a linearization of the Navier–Stokes

equations where the interface takes the form $h(z,t) = h_0 + \epsilon e^{\omega t}\cos(kz)$, he obtains a dispersion relation for the frequency and wavenumber of perturbations. From the physical point of view, the imaginary part $\Im(\omega)$ is the angular frequency of such disturbances, whereas the real part $\Re(\omega)$ indicates the growth or decay rate of the perturbations, so that systems where $\Re(\omega) > 0$ for at least one eigenvalue are unstable. Rayleigh concluded that the jet is unstable for axisymmetric modes whose wavelength λ is greater than the circumference of the jet $2\pi R$, as shown in Figure 1.2. In such cases, the Laplace pressure increases in constricted regions, driving the fluid outwards and further reducing the radius. On the contrary, at short wavelengths the effect of the axial curvature prevails, driving the fluid towards valleys and providing the cut-off wavelength.
Rayleigh's dispersion relation is not the mathematically simplest formulation to deal with. Since the most unstable wavelength is $\lambda_{opt} \simeq 9h_0$, the description of the amplification was later simplified keeping only the leading order terms in a long-wavelength expansion (Lee, 1974; Eggers & Villermaux, 2008),

$$\omega^2 = -\frac{1}{2}\frac{\sigma}{\rho h_0^3}\left[(kh_0)^2 - (kh_0)^4\right], \tag{1.1}$$

where σ and ρ are surface tension and density of the fluid, and h_0 is the unperturbed radius of the jet.

Under most circumstances, capillary jets are injected with a certain velocity with respect to the fixed reference frame of a nozzle, so that disturbances evolve in space rather than in time. A jet is a *convectively unstable* flow, in which perturbations remain finite at a fixed point since convection washes them downstream faster than they grow. Since oscillations on a jet are usually very small near the nozzle, such behavior is more appropriately described by requiring ω to be real and k to be complex (Keller *et al.*, 1972) and performing a *spatial stability analysis*. These spatial modes present the same frequency as the noise source, and grow or decay in space according to e^{ikz}, where k is a root of the dispersion relation $D(\omega, k) = 0$. There exists an infinite spectrum of complex roots k, the dominant mode presenting the fastest growth and positive group

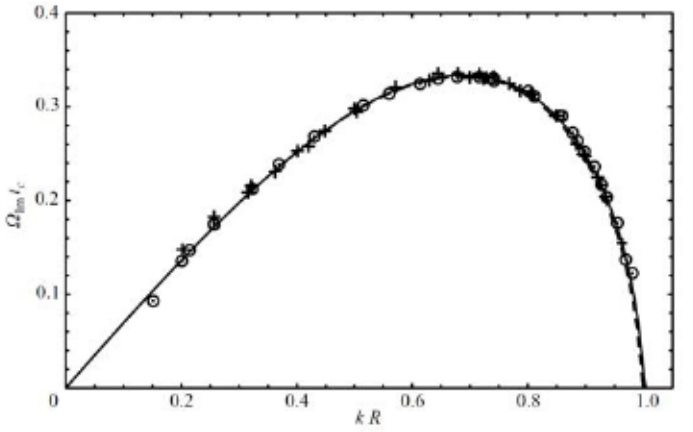

Figure 1.2: Dimensionless temporal growth rate versus wavenumber, obtained from experiments with ink, using the breakup time method (+) and the amplitude-evolution method (⊙). The lines correspond to theoretical predictions with (solid line) and without (dashed line) air effect for $Oh = 0.021$ and $We = 59$, using the spatial analysis and a translation to the temporal variables. Reproduced from the work of González & García (2009), where in the y-axis label Ω_{Im} stands for $\Im(\omega)$ and the characteristic time is $t_c = \rho R^3/\sigma$.

velocity $\partial\omega/\partial k > 0$.

In a spatial analysis, the growth rate is given by $-\Im(k^*)$, where $k^* = kh_0$ is the dimensionless wavenumber. Among the spatial modes arising from the dispersion relation, two capillary modes can be identified in both temporal and spatial analysis. The dominant capillary mode is responsible for the capillary instability, since $\Im(k^*) < 0$ when $\Re(k^*) < 1$, while the subdominant mode is always stable. Two upstream capillary modes which present large wavenumbers can only be identified in a spatial analysis, and are originated by the balance between capillarity and advective inertia. Other modes that cannot be captured by the one-dimensional model developed by Lee (1974) are the families of inertial and hydrodynamic modes (Guerrero *et al.*, 2012). These modes can coalesce, and *absolute instability* takes place when modes whose group velocities are opposite attain the same wavelength, resulting in perturbations wich grow while their group velocity remains null.

A temporal analysis is easier to implement than its spatial counterpart, but is only applicable to perturbations that grow uniformly in space. The spatial growth rates of certain modes agree well with their temporal counterparts on a cylinder when the jet velocity is high. In particular, when the Weber number is large enough, the spatial structure of disturbances along the jet is virtually uniform at the scale of one wavelength, justifying a much more simple temporal analysis performed in the jet's reference frame.

The case of parallel jets can be examined with the temporal theory first developed by Tomotika (1936), which was extended by Frankel & Weihs (1985) to include the effects of liquid inertia. They consider a basic flow subject to a temporal streching which is uniform in space, where the wavelength of perturbations is also a function of time owing to the basic elongational motion. The evolution of surface perturbations is addressed as an initial-value problem instead of an eigenvalue one. Their stability analysis reveals that the larger the initial wavenumber, the larger the amplification attained and the later it takes place.

When the stability of a quasi-parallel jet is addressed, the radius h_0 of the jet evolves in space, and consequently so do the stability properties of perturbations. In particular, if the characteristic scale at which the flow evolves is much larger than the wavelength of disturbances, it is possible to implement a *local stability analysis*. The analysis is local in the sense that a dispersion relation $D(\omega, k)$ applies at all points along the jet, interpreting $h_0 = h_0(z)$ and $k = k(z)$ as the local values of the jet radius and perturbation wave number. The amplitude of perturbations is obtained integrating the growth rate taking into account the spatial variation of h_0 and k.

In case a *local temporal analysis* is developed, the growth rate $\Re(\omega)$ has to be integrated,

$$G = \int_0^t \Re[\omega(k(0), \tau)]\, \mathrm{d}\tau = \frac{\pi}{Q} \int_0^z h_0(x)^2 \Re\{\omega[k(x), h_0(x)]\}\, \mathrm{d}x, \qquad (1.2)$$

where the time integral is transformed into a spatial one using $d\tau = dx/u_0$, and the amplification of perturbations is the exponential of equation (1.2), $\exp(G)$. In particular, an asymptotic temporal analysis is proposed by Senchenko & Bohr (2005) for a viscous fluid streaming from a small orifice and falling freely under gravity, subject to perturbations of wavelength k_o at the injector. They describe the jet with a one-dimensional model of mass and momentum conservation equations (Eggers & Dupont, 1994), deriving that far from the orifice $h_0(z) \sim z^{-1/4}$. To study the stability, the gain is computed on a co-moving frame, using the long wavelength model (1.1) to estimate the local growth rate $\Re(\omega)$. The latter is a function of a wavelength which evolves in space satisfying mass conservation, so that perturbations behave as $k = k_o h_0(z)^2/R^2$. Therefore, based on these simplifications, they pose that on a freely falling thread of fluid the amplitude of disturbances evolves as $\exp(z^{1/8})$, indicating that the growth of disturbances is slowed down with respect to the usual exponential behavior observed in a liquid cylinder. However, one limiting hypothesis is that equation (1.1) assumes an inviscid liquid, while the local Ohnesorge number increases downstream along the jet.

Another example of a local temporal analysis is the work of Javadi *et al.* (2013), in this case considering a spatial origin anywhere along the jet to *questionably* account for the effect of the meniscus in non-parallel jets.

Quasi-parallel assumptions can as well be applied to perform a *local spatial analysis* of flows which vary slowly in space, obtaining a dispersion relation at each axial coordinate. The local growth rate $-\Im[k(z)]$ is spatially integrated to yield the amplification of disturbances. This technique is used, for instance, in the work of Amini *et al.* (2013), including a discussion of the validity of this hypothesis depending on the non-parallelism of the flow.

To sum up, in a quasi-parallel jet the evolution of disturbances becomes an initial value problem coupled with an eigenvalue problem. To determine where break-up occurs, the initial amplitude of disturbances must be known, and then its spatial evolution must be computed integrating the growth rate. Even initially stable short wavelengths can amplify sufficiently downstream from the

injector, and there is not a specific wavenumber presenting maximum amplification throughout the jet.

It should be mentioned that the local stability analysis can also be implemented for slowly varying flows to identify the transition to global instability as the governing parameters are varied. In this case, the character of the instability changes from convective to absolute, corresponding in practice with a dripping regime. A spatiotemporal local analysis can identify this transition (Leib & Goldstein, 1986*a*,*b*; Le Dizès, 1997; Sevilla, 2011).

Nevertheless, the local assumptions are at least questionable when the flow presents highly non-parallel regions, such as the meniscus of the jets shown in figures 1.3 and 1.4. These flows require a more elaborate analysis, where no assumptions on the spatial shape of perturbations are made. Instead of using a classical eigenvalue analysis, a different perspective has to be considered. The *nonmodal stability theory* generalizes the stability analysis, considering it as the response of the governing equations to general input variables (Schmid, 2007). It consists of a general formulation based on a linear initial value problem, which is easily extendable to incorporate time-dependent flows, spatially varying configurations, and complex geometries, making it a useful tool for performing input–output study of flows (Barbagallo *et al.*, 2011; Bagheri *et al.*, 2009). The global frequency response analysis presented in Chapter 2 can be included among these nonmodal linear analyses.

Finally, it should be emphasized that all the analyses described above assume that the amplitude of disturbances is small. Large perturbations, wave interaction and the stages close to break-up must be described resorting to a *nonlinear analysis* (Eggers (1997); Eggers & Villermaux (2008) and references therein). This is the approach adopted in the analysis presented in Chapter 3.

1.3 Mathematical description of the jet

We consider an axisymmetric Newtonian liquid jet of density ρ and kinematic viscosity ν discharging into air at a constant flow rate Q from an injector of radius R, falling under the gravitational acceleration g, and with σ the liquid–air surface tension coefficient, as shown in Figure 1.3. The problem is posed on a cylindrical coordinate system, with z corresponding to the axial coordinate, and with the origin being located at the center of the exit section of the nozzle.

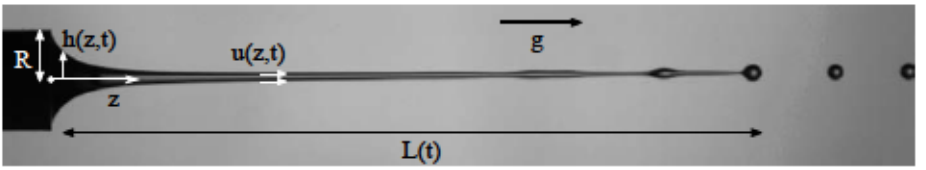

Figure 1.3: Photograph of a liquid jet stretched by gravity, where strong stretching is observed in the meniscus region near the outlet. The axial coordinate z, radius of the injector R, jet radius $h(z,t)$, axial speed $u(z,t)$ and jet length $L(t)$ are displayed as well. The arrow labeled g indicates the direction of the gravitational acceleration.

Instead of describing the flow with the Navier–Stokes equations, it is mathematically simpler to deal with a one-dimensional model. The advantage of using this formulation is a considerable reduction of calculation costs, while keeping the accuracy of results. For instance, a detailed comparison of the same leading order 1D model used throughout this Thesis with a 2D FEM algorithm is discussed in the work of Ambravaneswaran *et al.* (2002), who performed calculations of consecutive break-up events in a dripping regime. Moreover, the accuracy of several one-dimensional models when used in a local spatial analysis was assessed by Guerrero *et al.* (2016), showing good agreement with a 3D analysis. Many authors have taken advantage of these features, using one-dimensional formulations for performing stability analysis (Ambravaneswaran *et al.*, 2002; Senchenko & Bohr, 2005; Hanchak & Furlani, 2010; Amini *et al.*, 2013; Rubio-Rubio *et al.*, 2013).

In the following, we will derive the 1D model for jets presenting a typical radial length scale much smaller than the longitudinal scale. In this case, the velocity and pressure fields can be Taylor-expanded in the radial direction, and the governing equations are obtained by substituting truncated Taylor series into the Navier–Stokes equations together with appropriate boundary conditions. Depending on the order of the retained terms and the assumed velocity profile, different one-dimensional formulations such as viscous Lee, Cosserat, Parabolic and Averaged models can be deduced, as rigorously justified by García & Castellanos (1994). In this Thesis, we use the 1D model introduced by Eggers & Dupont (1994) and García & Castellanos (1994), in which only leading-order terms are retained.

The one-dimensional model is obtained starting from the Navier–Stokes equations for an axisymmetric column of liquid in cylindrical coordinates,

$$\frac{\partial \mathcal{V}}{\partial t} + \mathcal{V}\frac{\partial \mathcal{V}}{\partial r} + \mathcal{U}\frac{\partial \mathcal{V}}{\partial z} = -\frac{1}{\rho}\frac{\partial \mathcal{P}}{\partial r} + \nu\left(\frac{\partial^2 \mathcal{V}}{\partial r} + \frac{\partial^2 \mathcal{V}}{\partial z} + \frac{1}{r}\frac{\partial \mathcal{V}}{\partial r} - \frac{\mathcal{V}}{r^2}\right), \tag{1.3}$$

$$\frac{\partial \mathcal{U}}{\partial t} + \mathcal{V}\frac{\partial \mathcal{U}}{\partial r} + \mathcal{U}\frac{\partial \mathcal{U}}{\partial z} = -\frac{1}{\rho}\frac{\partial \mathcal{P}}{\partial z} + \nu\left(\frac{\partial^2 \mathcal{U}}{\partial r} + \frac{\partial^2 \mathcal{U}}{\partial z} + \frac{1}{r}\frac{\partial \mathcal{U}}{\partial r}\right) - g, \tag{1.4}$$

and

$$\frac{\partial \mathcal{V}}{\partial r} + \frac{\partial \mathcal{U}}{\partial z} + \frac{\mathcal{V}}{r}, \tag{1.5}$$

where z and r are the axial and radial coordinates, $\mathcal{U}$ and $\mathcal{V}$ are the axial and radial components of the velocity, and $\mathcal{P}$ is the pressure. These are suplemented with boundary conditions, consisting of the balance of normal and tangential forces at the air–liquid interface, and the kinematic condition at the surface, which can be found e.g. in Eggers & Dupont (1994). The fluid fields of the axysimmetric slender column are expanded in Taylor series in the radial direction,

$$\mathcal{U}(z,r) = \mathcal{U}_0 + \mathcal{U}_2 r^2 + ..., \tag{1.6}$$

$$\mathcal{V}(z,r) = -\frac{1}{2}\frac{\mathrm{d}\mathcal{U}_0}{\mathrm{d}z}r - \frac{1}{4}\frac{\mathrm{d}\mathcal{U}_2}{\mathrm{d}z}r^3 + ..., \tag{1.7}$$

and

$$\mathcal{P}(z,r) = \mathcal{P}_0 + \mathcal{P}_2 r^2 + \dots . \tag{1.8}$$

Upon substitution in the Navier–Stokes equations, and solving to lowest order, Eggers & Dupont's one-dimensional mass and momentum conservation equations are obtained (Eggers & Dupont, 1994) as

$$\frac{\partial h^2}{\partial t} + \frac{\partial (h^2 u)}{\partial z} = 0, \tag{1.9}$$

$$\frac{\partial u}{\partial t} + u\frac{\partial u}{\partial z} = -\frac{\sigma}{\rho}\frac{\partial \mathcal{C}}{\partial z} + g + \frac{3\nu}{h^2}\frac{\partial}{\partial z}\left(h^2 \frac{\partial u}{\partial z}\right), \tag{1.10}$$

where h and u are the jet radius and mean axial speed on a slice of the jet, the latter accounting for a physical velocity field which has both longitudinal and radial components. The full expression for the interfacial curvature is kept,

$$\mathcal{C} = h^{-1}\left[1 + \left(\frac{\partial h}{\partial z}\right)^2\right]^{-1/2} - \frac{\partial^2 h}{\partial z^2}\left[1 + \left(\frac{\partial h}{\partial z}\right)^2\right]^{-3/2}, \tag{1.11}$$

to provide an *exact* balance between gravity and surface tension in the meniscus region near the outlet. Moreover, the axial curvature must be preserved to study the capillary instability since it opposes to the effect of the radial curvature, being responsible for the cut-off for high frequency disturbances.

Throughout this Thesis, we describe the dynamics of the jet using equations (1.9)-(1.11), which are known to give an excellent description of gravitationally stretched jets, as Rubio-Rubio *et al.* (2013) have experimentally demonstrated.

Nondimensionalization Equations (1.9)-(1.11) are nondimensionalized using the radius and the speed of the jet at the injector as characteristic length and velocity scales, $z_c = R$ and $u_c = U$. The characteristic time at which perturbations evolve is given by the capillary time, $t_\sigma = \sqrt{\rho R^3/\sigma}$, for low viscosity jets ($Oh \leq 1$) or by the visco-capillary time, $t_\mu = \mu R/\sigma$, for more viscous fluids ($Oh > 1$).

Therefore, the dimensionless parameters in the governing equations become the Weber number $We = \rho R u_0^2/\sigma$ which compares the kinetic and surface energies, the Bond number $Bo = \rho g R^2/\sigma$ which accounts for the relative importance of gravity and surface tension, and the Ohnesorge number $Oh = \mu/(\rho R \sigma)^{1/2}$ which can be interpreted as the inverse of the Reynolds number based on the capillary velocity $v_\sigma = R/t_\sigma$. Physically, these dimensionless numbers can be associated to the three control parameters of the flow: larger values of Q, R and ν result in higher We, Bo and Oh respectively.

Finally, it should be mentioned that we attempted to balance terms in the momentum equation to obtain better scales, so that neater dimensionless equations and simple correlations between input and output parameters could be obtained. However, this task remains ongoing work, and we decided to present most results of this Thesis dimensionally. Without detracting from these drawbacks, the used characteristic scales are advantageous since they improve the stability of the numerical method.

1.4 Outline of the dissertation

The present Thesis deals with the stability of strongly stretched liquid jets, as those displayed in figures 1.3 and 1.4. These are generated by injecting fluid from a needle into a stagnant air atmosphere, at a constant flow rate that is slightly larger than the critical value at which the flow transitions from jetting to dripping. The shape of these jets is determined by three control parameters, namely the viscosity of the working fluid, the diameter of the injector and the flow rate, and, as explained before, their dynamics can be properly and efficiently described with the one-dimensional mass and momentum conservation equations. The aim of our study is to understand the role of the meniscus in the evolution of the advected disturbances in different flow configurations, which in turn will allow us to predict the break-up behavior in terms of the intact length and the most amplified disturbances.

These jets are subjected to two very distinctive sources of disturbances, namely

due to ambient noise or specifically imposed, which in the cases that we study manifest themselves as fluctuations of the axial speed at the injector exit. Since the initial conditions present different characterization depending on the origin of perturbations, the study of the evolution of their amplitude as they are advected by the jet and the eventual break-up that they originate require different experimental and theoretical approaches.

Figure 1.4: Natural break-up of a jet stretched by gravity, obtained when a fluid with kinematic viscosity $\nu = 50$ cSt is injected trhough a tube of inner diameter $D_i = 6.5$ mm at a flow rate $Q = 0.12$ ml/s.

Chapter 2 deals with the natural break-up of jets, where disturbances consist mainly of noise coming from the ambient and from the experimental facility. In this case, the latter is designed to minimize their amplitude. Although for theoretical purposes it is usually assumed that perturbations can be described as white noise, the passive control of disturbances does not guarantee, in practice, that energy is uniformly distributed among all frequencies.

We present experimental measurements of the intact length, finding that they qualitatively respond to variations of the control parameters in a similar way as more slender jets studied in previous works (Nonnenmacher & Piesche, 2004; Javadi *et al.*, 2013). We also report a parameter which, to our knowledge, has not been previously measured, namely the optimal frequency which causes the break-up.

Regarding the theoretical approach to the natural break-up, the small amplitude of velocity fluctuations suggests that a linear approach is valid during most of the amplification process, being violated only in the final stages prior to break-up. We therefore study the natural break-up resorting to linear stability analysis, in which the flow is separated into a steady basic flow plus small dis-

turbances. We initiate the discussion presenting a local spatial analysis, which is able to describe the evolution of disturbances when the basic flow is quasi-parallel. However, since this hypothesis is manifestly violated in the meniscus, we abandon the modal stability analysis and present a novel global frequency response analysis. In this input-output analysis, the response exhibits a form $\phi(x,t) = \hat{\phi}(x)e^{i\omega t}$. Based on this theoretical approach, we perform numerical calculations which enable us to capture the evolution of disturbances and in particular the damping effect of the meniscus. We also use this formalism to predict break-up, calculating the intact length and the optimal frequency.

We devote Chapter 3 to the controlled break-up of jets, analyzing experiments where mechanical forcing is used to impose velocity fluctuations at the injector of known amplitude and frequency. In this way, uncertainties regarding the energy distribution in the natural break-up are overcome. Stimulation parameters are swept over different flow configurations, observing a transition from chaotic to periodic break-up, and finally establishing an oscillatory dripping regime when the amplitude of disturbances is large enough.
To properly describe the stability of large amplitude perturbations and capture the final stages before break-up, a nonlinear analysis is performed. In our numerical approach, the evolution of the fluid field is obtained integrating the fully nonlinear one-dimensional conservation equations, enabling us to accurately predict the break up length and confirming the delay in the growth of capillary disturbances in the meniscus region.

We finally summarize the conclusions of this Thesis and indicate future works in Chapter 4.

References

AMBRAVANESWARAN, B., WILKES, E. D. & BASARAN, O. A. 2002 Drop

formation from a capillary tube: Comparison of one-dimensional and two-dimensional analyses and occurrence of satellite drops. *Phys. Fluids* 14, 2606–2621.

AMINI, G., IHME, M. & DOLATABADI, A. 2013 Liquid jet instability under gravity effects. *Phys. Rev. E* 87 (053017).

BAGHERI, S., HENNINGSON, D. S., HOEPFFNER, J. & SCHMID, P. J. 2009 Input-output analysis and control design applied to a linear model of spatially developing flows. *Appl. Mech. Rev.* 62 (020803).

BARBAGALLO, A., SIPP, D. & SCHMID, P.J. 2011 Input-output measures for model reduction and closed loop control: application to global modes. *J. Fluid Mech.* 685, 23–53.

BASARAN, O. 2002 Small-scale free surface flows with break-up: Drop formation and emerging applications. *AIChE J.* 48 (9), 1842–1847.

BOGY, D. B. & TALKE, F. E. 1984 Experimental and theoretical study of wave propagation phenomena in drop-on-demand ink jet devices. *IBM J. Res. Dev.* 28 (3), 314–321.

CHAUDHARY, K. C. & MAXWORTHY, T. 1980*a* The nonlinear instability of a liquid jet. Part 2. Experiments on jet behaviour before drodrop formation. *J. Fluid Mech.* 96, 275–286.

CHAUDHARY, K. C. & MAXWORTHY, T. 1980*b* The nonlinear instability of a liquid jet. Part 3. Experiments on satellite drop formation and control. *J. Fluid Mech.* 96, 287–297.

CHAUDHARY, K. C. & REDEKOPP, L. G. 1980 The nonlinear instability of a liquid jet. Part 1. Theory. *J. Fluid Mech.* 96, 257–274.

CHAUHAN, A., MALDARELLI, C., RUMSCHITZKI, D. & PAPAGEORGIEU, D. 2002 An experimental investigation on the convective instability of a jet. *CES* 58, 2421–2432.

CHEONG, B.S. & HOWES, T. 2004 Capillary jet instability under the influence of gravity. *CES* 59, 2145–2157.

CHUECH, S. G. & YAN, M. 2006 Application of the tvd scheme to the nonlinear instability analysis of a capillary jet. *Int. J. Numer. Meth. Fluids* 52, 1159–1174.

DONG, H., CARR, W. W. & MORRIS, J. F. 2006 An experimental study of drop-on-demand drop formation. *Phys. Fluids* 18 (072102).

DONNELLY, J. & GLABERSON, W. 1966 Experiments on the capillary instability of a liquid jet. *Proc. R. Soc. Lond. A Math. Phys. Sci.* 290, 547–556.

DOSHI, J. & RENEKER, D. H. 1995 Electrospinning process and applications of electrospun fibers. *J. Electrostatics* 35, 151–160.

EGGERS, J 1993 Universal pinching of 3d axisymmetric free-surface flow. *Phys. Rev. Lett.* 71, 3458.

EGGERS, J 1997 Nonlinear dynamics and breakup of free surface flows. *Rev. Mod. Phys.* 69, 865–929.

EGGERS, J. & DUPONT, T.F. 1994 Drop formation in a one-dimensional approximation of the navier-stokes equation. *J. Fluid Mech.* 262, 205–222.

EGGERS, J. & VILLERMAUX, E. 2008 Physics of liquid jets. *Rep. Prog. Phys.* 71, 036601.

FRANKEL, I & WEIHS, D. 1985 Stability of a capillary jet with linearly increasing axial velocity (with application to shaped charges). *J. Fluid Mech.* 155, 289–307.

FURLANI, E. P. & HANCHAK, M. S. 2010 Nonlinear analysis of the deformation and breakup of viscous microjets using the method of lines. *Int. J. Numer. Meth. Fluids* .

GAÑÁN-CALVO, A.M. 1998 Generation of steady liquid microthreads and micron-sized monodisperse sprays in gas streams. *Phys. Rev. Lett.* 80 (2), 285–288.

GARCÍA, F.J. & CASTELLANOS, A. 1994 One-dimensional models for slender axisymmetric viscous liquid jets. *Phys. Fluids* 6 (8), 2676–2689.

GARCÍA, F. J., GONZÁLEZ, H., CASTREJÓN-PITA, J. R. & CASTREJÓN-PITA, A. A. 2014 The break-up of harmonically stimulated capillary jets. *App. Phys. Lett.* 105 (094104).

GONZÁLEZ, H. & GARCÍA, F.J. 2009 The measurement of growth rates in capillary jets. *J. Fluid Mech.* 619, 179–212.

GUERRERO, J., GONZÁLEZ, H. & GARCÍA, F.J. 2012 Spatial modes of capillary jets with application to surface stimulation. *J. Fluid Mech.* 702, 354–377.

GUERRERO, J., GONZALEZ, H. & GARCIA, F. J. 2016 Spatial modes in one dimensional models for capillary jets. *Phys. Rev. E* 93 (033102), 1–9.

HANCHAK, M. S. & FURLANI, E. P. 2010 Modeling drop generation at the microscale. *NSTI Nanotech* 2.

JAVADI, A., EGGERS, J., BONN, D., HABIBI, M. & RIBE, N. M. 2013 Delayed capillary break-up of falling viscous jets. *Phys. Rev. Lett.* 110 (144501).

KALAAJI, A., LOPEZ, B., ATTANÉ, P. & SOUCEMARIANADIN, A. 2003 Breakup length of forced liquid jets. *Phys. Fluids* 15 (9).

KAMINSKI, T. S., SCHELERAB, O. & GARSTECKI, P. 2016 Droplet microfluidics for microbiology: techniques, applications and challenges. *Lab Chip* 16, 2168–2187.

KELLER, J.B., RUBINOW, S.I. & TU, Y.O. 1972 Spatial instability of a jet. *Phys. Fluids* 16, 2052–2055.

LE DIZÈS, S. 1997 Global modes in falling capillary jets. *Eur. J. Mech. B/Fluids* 16, 761–778.

LEE, C. H. 1974 Drop formation in a liquid jet. *IBM J. Res. Develop.* 18 (4).

LEIB, S. J. & GOLDSTEIN, M. E. 1986*a* Convective and absolute instability of a viscous liquid jet. *Phys. Fluids* 29 (4), 952–954.

LEIB, S. J. & GOLDSTEIN, M. E. 1986*b* The generation of capillary instabilities on a liquid jet. *J. Fluid Mech.* 168, 479–500.

LIN, S. P. & REITZ, R. D. 1998 Drop and spray formation from a liquid jet. *Annu. Rev. Fluid Mech.* (30), 85–105.

MANSOUR, N. N. & LUNDGREN, T. S. 1990 Satellite formation in capillary jet break-up. *Phys. Fluids A* 2 (7), 1141–1144.

MEIER, G.E.A., KLOPPER, A. & GRABITZ, G. 1992 The influence of kinematic waves on jet break down. *Exp. Fluids* (12), 173–180.

MEIER, G. E. A., LOOSE, S. & STASICKI, B. 1998 Unsteady liquid jets. *Applied Scientific Research* 58, 207–216.

MIKAMI, T., COX, R. G. & MASON, S.G. 1975 Break-up of extending liquid threads. *Int. J. Multiphase Flow* 2, 113–138.

MOALLEMI, N. & MEHRAVAN, K. 2016 Breakup of capillary jets with different disturbances. *Phys. Fluids* 28 (012101).

NONNENMACHER, S. & PIESCHE, M. 2004 Stability behavior of liquid jets under gravity. *Chem. Eng. Technol.* 27 (5), 529–536.

PEARSON, J.R.A. & MATOVICH, M.A. 1969 Spinning a molten threadline. *I&EC fundamentals* 8, 605–609.

PLATEAU, J. 1873 *Statique Expérimentale et Théorique des Liquides*. Gauthier-Villars et C^{ie}, Paris.

RAYLEIGH, W. S. 1878 On the instability of jets. *Proc. London Math. Soc.* 10, 4–13.

RUBIO-RUBIO, M., SEVILLA, A. & GORDILLO, J.M. 2013 On the thinnest steady threads obtained by gravitational stretching of capillary jets. *J. Fluid Mech.* 729, 471–483.

RUTLAND, D. F. & JAMESON, G. J. 1971 A non-linear effect in the capillary instability of liquid jets. *J. Fluid Mech.* 46 (2), 267–271.

SAVART, F. 1833 Memoire sur la constitution des veines liquides lancées par des orifices circulaires en mince paroi. *Ann. de Chim.* 53, 337–386.

SCHMID, P.J. 2007 Nonmodal stability theory. *Annu. Rev. Fluid Mech.* 39, 129–162.

SENCHENKO, S. & BOHR, T. 2005 Shape and stability of a viscous thread. *Phys. Rev. E* 71 (056301).

SEVILLA, A 2011 The effect of viscous relaxation on the spatiotemporal stability of capillary jets. *J. Fluid Mech.* 684, 204–226.

STERLING, A. M. & SLEICHER, C. A. 1975 The instability of capillary jets. *J. Fluid Mech.* 68, 477–495.

TOMOTIKA, S. 1936 Breaking up of a drop of viscous liquid immersed in another viscous fluid which is extending at a uniform rate. *Proc. Roy. Soc.* 153, 302–318.

UTADA, A. S., CHU, L.-Y., FERNANDEZ-NIEVES, A., LINK, D. R., HOLTZE, C. & WEITZ, D. A. 2007 Dripping, jetting, drops, and wetting: The magic of microfluidics. *MRS Bull.* 32, 702–708.

VAN DYKE, M. 1982 *An album of fluid motion*. The parabolic press.

YUEN, M. 1968 Non-linear capillary instability of a liquid jet. *J. Fluid Mech.* 33, 151–163.

CHAPTER

TWO

Natural break-up of gravitationally stretched jets

Contents

2.1 Introduction

We consider an axisymmetric Newtonian liquid jet discharging into air at constant flow rate, falling under the influence of the gravitational acceleration, as

those displayed in Figures 1.3 and 1.4. For sufficiently large values of the injected speed the jet is *globally stable* (Rubio-Rubio *et al.*, 2013), in the sense that no self-sustained resonant states, typically a dripping regime, may arise. Nevertheless, farther downstream at a certain break-up length, L_b, the Rayleigh instability causes the liquid column to disintegrate into droplets. In this chapter we study the natural break-up of these jets by means of experiments and a linear stability analysis, considering cases where the jet is subjected to velocity disturbances of small amplitude coming from noise in the experimental facility. As a consequence of the basic elongational flow, the perturbations which grow while they are advected by the jet do not exhibit a simple exponential time dependence (Tomotika, 1936; Mikami *et al.*, 1975; Frankel & Weihs, 1985).

Our research focuses on the effect of stretching on the development of capillary instabilities on jets accelerated by gravity. In general, extensional flows allow the generation of long ligaments when the stretching effect is strong enough. For instance, it has been previously observed that extending liquid bridges become as soon as the stretching is turned off (Marmottant & Villermaux, 2004). In the case of a liquid cylinder axially elongating with time in the Stokes regime, Tomotika (1936) was the first to identify the damping role of stretching, an analysis that was later revised by Mikami *et al.* (1975). These authors pointed out the important fact that initially stable perturbations of short wavelengths were elongated by the flow until they became unstable and originated the break-up of the liquid ligament. Indeed, an extending thread increases the wavelength of perturbations and decreases their amplitude (Eggers & Villermaux, 2008). In a gravitationally stretched jet, the distance between two given fluid particles increases in the axial direction due to their different velocities, and the same occurs to the radius disturbances, leading to an increment of their wavelength downstream. To comply with mass conservation, the amplitude must therefore decrease in the downstream direction, provided that this stabilizing mechanism dominates over the destabilization associated with the Plateau–Rayleigh instability.

Previus works include several experimental studies dealing with the parametric study of the natural break-up of gravitationally stretched capillary jets, where it was found that the break-up length increases with both the injected flow rate and the liquid viscosity (Nonnenmacher & Piesche, 2004; Javadi *et al.*, 2013). However, this works did not consider cases with a strong stretching in the meniscus region that appear for larger injectors and smaller flow rates closeto the jetting–dripping transition threshold. Thus, in the present Thesis we carried out experiments where three control parameters were varied, namely the liquid viscosity, the injector diameter and the liquid flow rate, to produce strongly stretched jets. Considering the hysteretic nature of the transition to global instability when injecting the fluid at low flow rates using relatively large nozzles reported by Rubio-Rubio *et al.* (2013), the characterization of the break-up phenomenon under these conditions represents a neccesary extension of the existing work. Moreover, our experiments offer information regarding the frequency of the most amplified disturbances, a parameter which, to our knowledge, has not been reported before.

The stability analysis of the natural break-up of jets can be addressed applying linear assumptions, since the amplitude of disturbances remains small during most of the amplification process. In most previous works, the stability has been studied using a modal analysis in a local formulation. An important exception is the work of Frankel & Weihs (1985) on jets with linearly increasing axial velocity, finding that, since the growth rate of a given harmonic perturbation is not constant, its temporal evolution has to be integrated to determine the dominant wavelength, which varies along the process. Moreover, in agreement with the findings of Tomotika (1936) and Mikami *et al.* (1975), break-up can be induced by initially stable disturbances. Later, the asymptotic theory due to Senchenko & Bohr (2005) revealed that spatial growth has the form $\exp(z^{1/8})$ in the free-fall region sufficiently far from the outlet. Recently, Javadi *et al.* (2013) proposed the optimization of both the frequency and the initial position of disturbances to predict its break-up. However, the latter assumption regard-

ing the spatial origin of the disturbance along the jet is questionable, and will be interpreted in this Thesis as a delayed growth of perturbations originated in the feeding system due to the presence of the meniscus near the outlet. Amini *et al.* (2013) applied local stability theory to perform a parametric study, and reported that the growth rate of perturbations increases when the Weber number is lowered or the Bond number is increased, consistent with previous works. Following this classical approach, here we present a local analysis in which the non-paralellism of the flow is taken into account by deriving a dispersion relation where leading order non-parallel terms are retained. However, such a local analysis is only valid when the basic flow is slowly varying (Amini *et al.*, 2013). In the flow configurations under study in this thesis, quasi-parallel assumptions are violated in the meniscus, what requires a fully non-parallel approach for a correct description.

In the last decades, the non-modal stability analysis technique has been developed (Reddy *et al.*, 1993; Trefethen *et al.*, 1993), motivated by the frequent failure to predict the flow structures and transitions observed in experiments with a modal approach. In practice, certain asymptotically stable flows exhibit substantial transient amplification of the input energy. Such behavior is explained by the non-normality of the linearized evolution of the operator which governs the evolution of small amplitude disturbances (Bagheri *et al.*, 2009), this being the case of convectively unstable flows (Chomaz, 2005; Schmid, 2007). In a non-modal approach, the stability analysis is addressed in an input-output formalism. The flow field is described using a state-space formulation, where the operator governing the dynamics of the system acts as a mapping of initial conditions or external excitations onto output variables (Schmid, 2007). As revieweded by Bagheri *et al.* (2009), the main tools of investigation in this framework are the impulse response, the frequency response and the transfer functions. Forcing is typically applied at a specified location as an impulsive signal to analyze frequency selection behavior, or as a harmonic signal to yield the frequency response of the linear system. Meanwhile, the transfer function

can be regarded as a generalization of the resolvent which describes the relation between inputs and outputs.

These techniques have been succesfully applied to model convectively unstable flows (see Schmid (2007), Bagheri *et al.* (2009) and references therein) which display extrinsic dynamics, being sensitive to the nature of forcing and acting as noise amplifiers. In such cases, unstable waves amplify while they are advected by the flow, and therefore at a fixed station perturbations grow initially to decay later as the tail of the wave packet passes by. In contrast, globally unstable flows behave as flow oscillators with a well-defined frequency that is rather insensitive to external forcing. In spatially developing flows, the existence of a pocket of absolute instability is a necesary but not sufficient condition for global instability (Chomaz *et al.*, 1988).

It is clear that an input-output analysis is the appropriate tool to account for a strongly spatially varying flow configuration. Therefore, in this chapter we propose a novel global frequency response analysis of liquid jets stretched by gravity. In this general linear formulation, instead of adopting the normal mode assumption, we study the response of the jet with a function of the form $\phi(x,t) = \hat{\phi}(x)e^{i\omega t}$, where $\phi(x,t)$ is a generic flow variable, $\hat{\phi}(x)$ its associated spatial structure, and ω the forcing frequency.

2.2 Linear stability analysis

In the natural break up of stretched liquid jets, the amplitude of disturbances at the nozzle outlet is small, and therefore a linear analysis provides a good description of the evolution of perturbations except for a short time interval prior to pinch-off. Since the local analysis provides insight into the spatial growth of disturbances, we derive here a dispersion relation which includes non-parallel terms, and implement a quasi-parallel spatial stability analysis based on such dispersion relation. Although the latter methodology captures the fact that the most amplified frequency varies with the axial coordinate, the quasi-parallel

assumption is violated in the meniscus region. Therefore, a global analysis is also developed, where no assumptions on the shape of disturbances is made, except for their amplitude being small.

2.2.1 Mathematical description of the jet

In this chapter we deal with small-amplitude perturbations coming from the experimental facility. Accordingly, the problem will be studied with a linear approach, in which the radius and axial velocity of the jet are decomposed into a steady basic flow plus $\mathcal{O}(\epsilon)$ disturbances,

$$\begin{aligned} h(z,t) &= h_0(z) + \epsilon h_1(z,t), \\ u(z,t) &= u_0(z) + \epsilon u_1(z,t). \end{aligned} \tag{2.1}$$

The equations 2.1 are plugged into the conservation equations, and terms with different orders of magnitude are identified to solve the basic flow and the perturbed flow field, respectively.

As discussed in the previous chapter, a one-dimensional model of the Navier–Stokes equations is able to capture the dynamics of a slender jet while presenting a very low computational cost. We therefore describe the fluid field using the equations (1.9)-(1.11) of Chapter 1.

2.2.1.1 Basic flow

The steady basic flow $h_0(z)$, $u_0(z)$ is described by the steady version of the one-dimensional conservation equations (1.9)-(1.11). In particular, the steady version of the continuity equation (1.9) relates the position of the interface and the axial velocity,

$$u_0(z) = UR^2/h_0(z)^2, \tag{2.2}$$

where U is the mean outlet velocity and R is the inner radius of the injector. Substituting (2.2) into the steady version of the momentum equation (1.10),

the following nonlinear equation for $h_0(z)$ is obtained,

$$\mathcal{N}[h_0] = 2U^2R^4\frac{h_0'}{h_0^3} + \frac{\sigma}{\rho}\left[h_0'(1+h_0'^2)^{-1/2} + \left(h_0h_0'h_0'' + h_0^2h_0'''\right)(1+h_0'^2)^{-3/2}\right.$$
$$\left. -3h_0^2h_0'h_0''^2(1+h_0'^2)^{-5/2}\right] + gh_0^2 + 6UR^2\nu\left(\frac{h_0'^2}{h_0^2} - \frac{h_0''}{h_0}\right) = 0, \tag{2.3}$$

where primes denote spatial derivatives $\frac{\partial}{\partial z}$.
Sufficiently far downstream, where gravity and inertia are the dominating contributions, the steady jets follows Torricelli's free fall law (Eggers & Villermaux, 2008)

$$h_0(z) = \left(1 + \frac{2zg}{U^2}\right)^{-1/4} R. \tag{2.4}$$

In the meniscus region near the injector, the basic flow can be estimated performing a static balance between the gravity and capillary forces. If the curvature is approximated by $\mathcal{C} \sim 1/R$, the latter balance provides

$$h_0(z) = \left(\frac{1}{R} + \frac{\rho g z}{\sigma}\right)^{-1}. \tag{2.5}$$

2.2.1.2 Perturbed field

The mass and momentum equations for the perturbed fields $h_1(z,t)$ and $u_1(z,t)$ are obtained by linearizing equations (1.9)-(1.11) around the base flow described by equation (2.3). The linearization is done by plugging the decomposition (2.1) into (1.9)-(1.11), expanding in Taylor series and keeping only $\mathcal{O}(\epsilon)$ terms. Since the base flow is non-parallel, perturbations are governed by a pair of linear partial differential equations with variable coefficients, namely

$$\frac{\partial h_1}{\partial t} = \frac{-u_0'}{2}\,h_1 - u_0\,\frac{\partial h_1}{\partial z} - h_0'\,u_1 - \frac{h_0}{2}\,\frac{\partial u_1}{\partial z}, \tag{2.6}$$

$$\frac{\partial u_1}{\partial t} + u_0\,\frac{\partial u_1}{\partial z} + u_0'\,u_1 = -\frac{\sigma}{\rho}\frac{\partial \mathcal{C}}{\partial z} + 3\nu\left[\frac{2u_0'}{h_0}\,\frac{\partial h_1}{\partial z} + \frac{\partial^2 u_1}{\partial z^2} + \frac{2h_0'}{h_0}\,\frac{\partial u_1}{\partial z} - \frac{2u_0'h_0'}{h_0^2}h_1\right], \tag{2.7}$$

where h_0, h_0', h_0'', h_0''', u_0 and u_0' correspond to the steady base flow and its axial derivatives, and the linearized axial derivative of the mean curvature is

$$\frac{\partial \mathcal{C}}{\partial z} = \left(\frac{2h_0'}{{h_0}^3\sqrt{1+{h_0'}^2}} + \frac{h_0' h_0''}{h_0^2\left(1+h_0'^2\right)^{3/2}} \right) h_1 + \left(\frac{-1}{{h_0}^2\sqrt{1+{h_0'}^2}} + \frac{-\frac{h_0''}{h_0} + \frac{{h_0'}^2}{h_0^2}}{\left(1+{h_0'}^2\right)^{3/2}} + 3\frac{\frac{{h_0'}^2 h_0''}{h_0} + h_0''' h_0' + h_0''^2}{\left(1+h_0'^2\right)^{5/2}} - \frac{15 h_0''^2 h_0'^2}{\left(1+h_0'^2\right)^{7/2}} \right) \frac{\partial h_1}{\partial z} + \left(\frac{-h_0'}{h_0\left(1+h_0'^2\right)^{3/2}} + \frac{6h_0' h_0''}{\left(1+h_0'^2\right)^{5/2}} \right) \frac{\partial^2 h_1}{\partial z^2} - \frac{1}{\left(1+h_0'^2\right)^{3/2}} \frac{\partial^3 h_1}{\partial z^3}. \tag{2.8}$$

2.2.2 Local stability analysis

In a local analysis, it is assumed that the scale of perturbations is locally negligible compared to the characteristic length of spatial evolution of the jet, $\lambda \ll \Delta Z_c$. Therefore, each wavelength can be studied considering that the base flow upstream and downstream of it remains constant. Under these conditions, parallel stability analysis can be performed at each station, obtaining a local dispersion relation for the pair (ω, k).

In this section we present a quasi-parallel formulation which consits of deriving a dispersion relation where non-parallel terms are kept and performing a local spatial analysis. Although this approach is not valid for strongly stretched jets, it is useful to gain understanding about the axial evolution of small disturbances. The details of the spatial analysis can be consulted in detail in the Master Thesis by Consoli-Lizzi (2012).

2.2.2.1 Local dispersion relation

The local approach is based on perturbing the solution to equations (1.9)-(1.11), and assuming normal modes of the travelling-wave form $(h_1, u_1) = (\hat{h}_1, \hat{u}_1)e^{\mathfrak{i}(kz-\omega t)}$, to obtain a dispersion relation that includes nonparallel terms. The evolution of the amplitude of disturbances is tracked by locally computing and integrating the spatial growth rate.

The steady basic flow $h_0(z)$, $u_0(z)$ is obtained by solving equations (2.2)-(2.3). The amplitude of radius and velocity disturbances $\hat{h}_1, \hat{u}_1$ can be related using the mass conservation equation (2.6),

$$\hat{u}_1 = \hat{h}_1 \frac{i\omega - u_0'/2 - u_0 ik}{h_0' + h_0/2ik}. \tag{2.9}$$

The normal modes assumption are also introduced in the momentum equation (2.7), and after substituting equation (2.9) and eliminating the common exponential factor, the following dispersion relation is obtained,

$$\begin{aligned} D(\omega,k) = -\frac{\sigma}{\rho}\Bigg[& \left(\frac{2h_0'}{{h_0}^3\sqrt{1+{h_0'}^2}} + \frac{h_0'h_0''}{{h_0}^2\left(1+{h_0'}^2\right)^{3/2}} \right) + \\ & \left(\frac{-1}{{h_0}^2\sqrt{1+{h_0'}^2}} + \frac{-\frac{h_0''}{h_0} + \frac{{h_0'}^2}{h_0^2}}{(1+{h_0'}^2)^{3/2}} + 3\frac{\frac{{h_0'}^2 h_0''}{h_0} + h_0'''h_0' + {h_0''}^2}{(1+{h_0'}^2)^{5/2}} - \right. \\ & \left. \frac{15{h_0''}^2{h_0'}^2}{\left(1+{h_0'}^2\right)^{7/2}} \right) ik - \left(\frac{-h_0'}{h_0\left(1+{h_0'}^2\right)^{3/2}} + \frac{6h_0'h_0''}{\left(1+{h_0'}^2\right)^{5/2}} \right) k^2 + \\ & \frac{ik^3}{\left(1+{h_0'}^2\right)^{3/2}} \Bigg] + 6\nu\frac{u_0\left(-h_0' + ih_0k\right)}{{h_0}^2} + \frac{i\omega - 1/2h_0' - iu_0k}{h_0' + 1/2ih_0k} \\ & \left[-u_0' + i\left(6\nu\frac{h_0'}{h_0} - u_0\right)k + i\omega - 3\nu k^2 \right] = 0, \end{aligned} \tag{2.10}$$

This dispersion relation (2.10) presents four spatial modes, just like the one obtained from Lee's one-dimensional formulation for an inviscid liquid jet (Lee, 1974), which reads

$$D_{Lee}(\omega,k) = k^4 - \frac{k^2}{R^2} + 2\omega^2\frac{\rho}{R\sigma} = 0, \tag{2.11}$$

but in contrast to the latter dispersion relation, (2.10) includes non-parallel and viscous effects.

In fact, we have verified that the dispersion relation derived by Guerrero *et al.* (2012) from a viscous Lee model,

$$D_{v\ Lee}(\omega,k) = -\frac{R\sigma}{\rho}k^4 - 6i\nu k^3 + k^2\left(\frac{\sigma}{R\rho} + 6i\nu\omega + 2U^2\right) - 4Uk\omega + 2\omega^2 = 0,$$

(2.12)

can be retrieved from the dispersion relation (2.10). In Consoli-Lizzi (2012), a *local* formulation of the dispersion relation (2.10) was proposed: local characteristic scales based on the basic flow were adopted for both the perturbed radius and velocity, namely $z_c = h_0(z)$ and $u_c = u_0(z)$, and as a result the local values of the dimensionless parameters $We_l(z) = \rho h_0(z) u_0(z)^2/\sigma$ and $Oh_l(z) = \rho g h_0(z)^2/\sigma$ naturally arise. Also, for a clearer interpretation of the non-parallel terms, we adopted a different scale for axial variations of the base flow, in which spatial derivatives of $h_0(z)$ and $u_0(z)$ were of order unity due to the balance between inertia and gravity. The use of the scaling $Z_c = U^2/g$ which accounts for axial variations resulted in the introduction of different powers of the Bond number $Bo = \rho g R^2/\sigma$ in the non-parallel terms. For instance, when introducing dimensionless variables indicated with superscript *, a term with $h_0'' = Bo^2/We^2 h_0^{*''}$ appears, which vanishes in the case of the parallel basic flow described by equation (2.12).

2.2.2.2 Stability analysis

Four spatial modes satisfy the dispersion relation (2.10), as shown in Figure 2.1(a) for a slender jet with $\nu = 1$ cSt, $R = 1$ mm and $Q = 1.6$ ml/s. Among these modes, the *dominant capillary mode* (Guerrero *et al.*, 2012) represented as solution 3 in Figure 2.1 is responsible for the break-up of the jet. It can be identified at the nozzle exit as the branch of dimensionless $k^*(\omega^*)$ with $\Im(k^*) < 0$ for $\omega^* \sim 1$ and $\Re(k^*) > 0$, where $k^* = kR$ and $\omega^* = \omega t_\sigma$ if $Oh \simeq 1$ or $\omega^* = \omega t_\mu$ if $Oh > 1$.

As the basic flow stretches downstream, the dispersion relation and its solutions vary with the axial coordinate. Given a frequency ω, a Newton–Raphson method implemented on an adaptive spatial mesh with a seed value given by the three last eigenvalues enables the tracking of the dominant capillary mode along the jet, as displayed in Figure 2.1(b). Notice that the maximum growth

rate decreases and moves to larger frequencies as the axial coordinate increases. This is due to the increase in the local Weber number as the flow accelerates, $We_l(z) = We h_0^*(z)^-3$.

Since the growth rate of perturbations depends on z, it is necesary to integrate

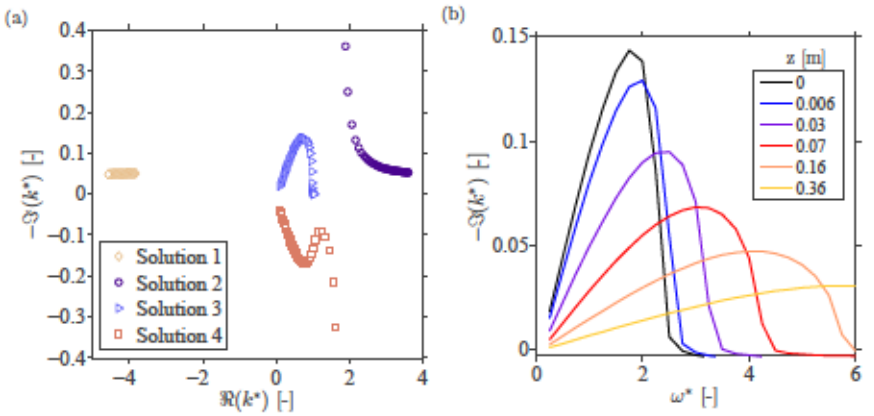

Figure 2.1: Solutions to the dispersion relation (2.10). (a) Visualization in the complex k^* plane of the four spatial branches of the dispersion relation for $\omega^* \in [0\ 4]$ at the injector exit $z = 0$. Solution 3 is the dominant capillary mode. (b) Dimensionless spatial growth rate $-\Im(k^*)$ as a function of frequency ω^*, showing the evolution of the dispersion relation at different axial positions z.

along the jet to obtain the evolution of the disturbance amplitude. For a given frequency, the gain G is defined as

$$G(z) = \int_0^z -\Im(k)dz \tag{2.13}$$

As pointed out by Frankel & Weihs (1985) in a temporal setting, modes that are initially damped become unstable as they propagate downstream, growing quickly in a first stage and decelerating afterwards. Figure 2.2(a) reveals that modes with larger wavelength travel a longer distance before presenting a maximum growth rate and are subject to it for a longer time. As a result, their accumulated gain overcomes that of modes with shorter wavelength. Break-up takes place when a certain critical gain, G_c, is reached. The value of G_c is defined by the initial amplitude due to the noise of the experimental facility,

ϵ/R, and decreases with the distance to the injector, as the radius of the jet is reduced. At the station L_b where the breakup occurs, the critical gain is

$$G_c(L_b) = \ln\left(\frac{h_0(L_b)}{\epsilon}\right) = \ln\left(\frac{R}{\epsilon}\right) + \ln\left(\frac{h_0(L_b)}{R}\right) \tag{2.14}$$

In other words, as shown in Figure 2.2(b), breakup is produced by the first global frequency ω_b whose accumulated gain reaches the critical value for the smallest possible axial coordinate.

Note that in the example treated with this local approach, unlike the natural break-up which we study experimentally, the contact line does not remain pinned at the injector wall but exhibits fluctuations of amplitude ϵ/R, a deffi-ciency of the model that will be overcome by the global approach presented in section 2.2.3.

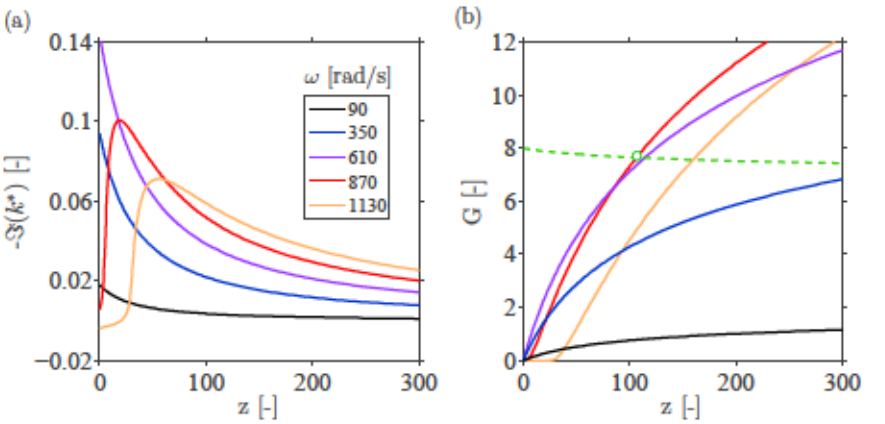

Figure 2.2: Growth of disturbances predicted by the local analysis for different frequencies ω. (a) Spatial evolution of the dimensionless growth rate $-\Im(k^*)$. (b) Spatial evolution of the accumulated gain G (solid lines) and of the critical gain G_c (dashed line) when $G_c(0) = 8$. Break up takes place at $L_b = 0.1$ m for $\omega_b = 870$ rad/s.

2.2.2.3 Limitations of the local analysis

In a local analysis, each wavelength is studied considering that the base flow upstream and downstream of it remains constant. For example, Amini *et al.* (2013) used a weakly non-parallel approximation and justified their approach by introducing a dimensionless parameter γ that measures the degree of non-parallelism, verifying that its value remained smaller than one. The parameter γ compares the streamwise inhomogeneities of the mean flow and the wavelength of the instability, $\gamma = \frac{\lambda}{u_0/(\mathrm{d}u_0/\mathrm{d}z)}$. However, they indicate that for jets with $Bo \sim 1$ and $We < 5$, γ is close to 1. This is the case for many of the experiments carried out in this Thesis, where therefore the parallel assumptions are not valid. The slenderness of a typical basic flow analized in the present work, in particular $Bo = 1.8$ and $We = 0.02$, is illustrated in Figure 2.3. Close to the injector, the wavelength of disturbances with $\omega = 100$ rad/s is of the same order as the characteristic length at which the radius of the basic jet evolves axially, $\Delta Z_c = \frac{h_0}{\mathrm{d}h_0/\mathrm{d}z}$.

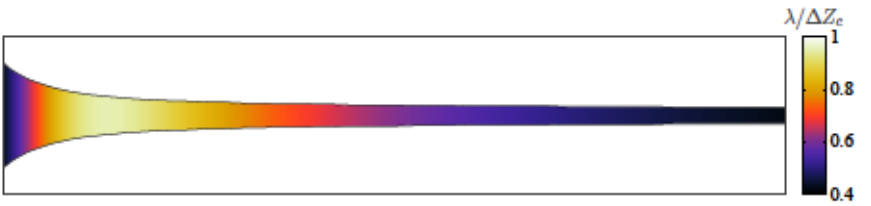

Figure 2.3: Steady jet of liquid with ν=50 cSt issuing from a tube with R=2 mm at Q =0.2 ml/s. Isocontours comparing the characteristic length of perturbations λ with the characteristic length at which the radius of the jet evolves axially ΔZ_c. The frequency of disturbances is $\omega = 100$ rad/s.

Although parallel assumptions are valid sufficiently far from the injector, this approach is not able to properly describe the evolution of disturbances in the near field. It can be anticipated that a substantial damping of their amplitude occurs in this region, an effect that is not properly captured when locally com-

puting the growth rate of the dominant capillary mode. In jets with $Bo \sim \mathcal{O}(1)$, frequencies which induce breakup correspond to initially short, stable wavelengths, which increase their length as they move downstream. Indeed, we have performed a local analysis for several jets with $Bo \sim 1$ and $We > 1$, adopting the negative spatial growth rate observed for the dominant capillary mode in this region. Predictions arising from this approach are questionable, since for a fixed initial amplitude of disturbances, ϵ/R, calculations suggest that the intact length decays when We increases, in contrast to experimental observations (Consoli-Lizzi, 2012).

Regarding the formulation by Javadi *et al.* (2013), they resort to an optimization of both the frequency and spatial origin of disturbances. In particular, the optimal initial position was found in the work of Javadi *et al.* (2013) to strongly depend on the values of the control parameters, a conclusion that rises doubts as to the validity of the underlying theory.

2.2.3 Global frequency response analysis

In a *global* approach the spatial shape of the disturbance is computed as part of the solution through a linear frequency response analysis. Here, the evolution of disturbances is addressed as the output of the jet to the input given by the forcing. The different tools available for performing an input–output analysis were reviewed by Bagheri *et al.* (2009), who exemplify the procedure with the Ginzburg–Landau equation. It is usual in a non-modal analysis to describe the behavior of the solution $q(t)$ using the state-space formulation,

$$\begin{aligned} \frac{\mathrm{d}q}{\mathrm{d}t} &= A\,q(t) + B\,u(t), \\ y(t) &= C\,q(t), \\ q(0) &= q_0, \end{aligned} \tag{2.15}$$

where A is the operator containing the discretized governing equations, B and C are matrices which govern the type and location of the input $u(t)$ and output $y(t)$, and the initial condition is q_0. The formal solution to the system (2.15)

has the form

$$y(t) = C\, e^{At} q_0 + C \int_0^t e^{A(t-\tau)} B\, u(\tau)\, \mathrm{d}\tau \tag{2.16}$$

where the first term in the right-hand side is the homogeneous solution, and the second corresponds the particular solution arising from the forcing $B\, u(t)$. If an initial condition $q_0 = 0$ is adopted, an input-output relation is retrieved which describes the transfer behavior of an input signal $u(t)$ as it passes through the linear system given by the operator A.

In the case where the frequency response to a purely harmonic forcing is examined, the input has the form $u(t) = e^{i\omega t}$. Assuming that the operator A corresponds to a globally stable state and $t \to \infty$, equation (2.16) yields

$$y(t) = |G(i\omega)| e^{(i\omega t + \varphi)} \tag{2.17}$$

where the transfer matrix is $G(i\omega) = C(i\omega I - A)^{-1} B$. Since the system is linear, the output presents the same frequency as the input, ω, with a phase shift Arg $G(i\omega)$ and an amplitude $|G(i\omega)|$. Therefore, in this analysis the transfer function $G(i\omega)$ fully describes the input-output behavior of the system.

To describe the linearized dynamics of the jet, we use the equations (1.9)-(1.11) supplemented with a forcing of the exit velocity of small amplitude ϵ and a pinned contact line at the injector. The flow is accordingly decomposed into a steady base jet plus $\mathcal{O}(\epsilon)$ disturbances, $[h(z,t), u(z,t)] = [h_0(z), u_0(z)] + \epsilon[h_1(z,t), u_1(z,t)]$. Denoting the perturbed fields $\phi(z,t) = [h_1(z,t), u_1(z,t)]$, the frequency response of the jet can be obtained by solving the linear PDE system

$$\frac{\partial \phi}{\partial t} = \mathcal{A}\phi, \quad \phi(0,t) = e^{i\omega t}. \tag{2.18}$$

for a given real frequency ω. As corresponds to a linear theory, it is assumed that different frequencies of the input do not interact and can be analyzed separately. In equation (2.18), the operator $\mathcal{A}$ contains the governing equations linearized around the steady base flow. The large-time response of the system presents the same frequency as the input, $\phi(z,t;\omega) = \hat{\phi}(z;\omega)\, e^{i\omega t}$ where

$\hat{\phi}(z;\omega) = [\hat{h}_1(z;\omega), \hat{u}_1(z;\omega)]$, with the spatial structure of the response formally given by

$$\hat{\phi}(z;\omega) = (i\omega\bar{\mathcal{I}} - \bar{\mathcal{A}})^{-1} b, \tag{2.19}$$

where $\hat{\phi}(z;\omega)$ is complex, the amplitude of perturbations being given by its modulus. The operators $\bar{\mathcal{I}}$ and $\bar{\mathcal{A}}$, and the vector b, incorporate the boundary conditions at $z = 0$.

When studying the natural break-up of a jet, it was assumed in the present work that all frequencies present the same initial amplitude, and thus $|\hat{\phi}(z;\omega)|$ is calculated for several frequencies. To predict the position L_b at which pinching occurs as well as the most amplified frequency at that axial location, ω_b, the amplitude ϵ of perturbations at the injector must be known. The break-up of the jet is considered to take place at the position where the amplitude of disturbances equals the local radius of the jet, $\epsilon\,|h_1(z = L_b;\omega_b)| = h_0(z = L_b)$, for the smallest possible value of L_b.

The radius of the steady base flow $h_0(z)$ is described by the nonlinear equation (2.3). To obtain a numerical solution, the spatial derivatives in the nonlinear boundary value problem are discretized. This is accomplished resorting to differentiation matrices, which are derived from the spectral collocation method described by Rubio-Rubio *et al.* (2013). The discrete derivative operators used in our work are based on the first, second and third order Chebyshev interpolants, D_1, D_2 and D_3, according to the subroutines developed by Weideman & Reddy (2000). The differential problem is thereby converted to a matrix problem, which is solved to find approximations to the function values at the collocation nodes. Since the Chebyshev interval is $y \in [-1, 1]$, it is mapped onto the physical domain $z \in [0, L]$ according to the transfromation

$$z = \frac{\beta L(1+y)}{2\beta + L(1-y)}, \tag{2.20}$$

where β is a clustering parameter which is determined to optimize the accuracy of the model. Typical values of β increase with the dimensionless length of

the physical domain, $\beta \geq 0.6L$. As a result of the metrics introduced by the mapping, derivatives in physical space must be obtained applying the chain rule (Rubio-Rubio *et al.*, 2013),

$$\begin{aligned}
\frac{\partial}{\partial z} &= \frac{\partial y}{\partial z} D_1, \\
\frac{\partial^2}{\partial z^2} &= \frac{\partial^y}{\partial z^2} D_1 + \left(\frac{\partial}{\partial z}\right)^2 D_2 \\
\frac{\partial^3}{\partial z^3} &= \frac{\partial^3 y}{\partial z^3} D_1 + 3\frac{\partial^2 y}{\partial z^2}\frac{\partial y}{\partial z} D_2 + \left(\frac{\partial y}{\partial z}\right)^3 D_3.
\end{aligned} \tag{2.21}$$

The number of collocation points, N, was determined by the dimensionless length of the domain and the slenderness of the jet, with typical values $N \geq 1.4L$. Larger values of N are necessary when the jet approaches the jetting-dripping transition, or when the stability of disturbances of frequencies larger than 500 rad/s is studied.

To obtain a solution for the base flow, an iterative Newton–Raphson method is implemented, knowing that this approach provides excellent agreement with experiments, as demonstrated by Rubio-Rubio *et al.* (2013). Since a nonlinear differential functional $\mathcal{N}$ operates on h_0, a linear operator $\mathcal{L}$ acting on Δh_0 is introduced, so that $\mathcal{N}[h_0] + \mathcal{L}[\Delta h_0] = 0$. The problem is discretized and $\mathcal{L}$ is formulated as a matrix M,

$$\begin{aligned}
M =& U^2 R^4 \left[\frac{2}{h_0^3}\mathcal{D}^1 - \frac{6h_0'}{h_0^4}\mathcal{I}\right] + \frac{\sigma}{\rho} h_0^2 \sum_{i=1}^{4} s^{2i-1}\,\mathcal{T}_i + 2g\,h_0\mathcal{I} + \\
& 6UR^2\nu \left[\frac{2h_0'}{h^2}\mathcal{D}^1 - \frac{2h_0'^2}{h_0^3}\mathcal{I} - \frac{1}{h_0}\mathcal{D}^2 + \frac{h_0''}{h_0^2}\mathcal{I}\right],
\end{aligned} \tag{2.22}$$

where $\mathcal{I}$ is the identity operator and $\mathcal{D}^n = \mathrm{d}^n/\mathrm{d}z^n$ is the n-th axial derivative operator. Curvature terms are those already presented in equation (2.8).

Therefore in equation (2.22) we have $s(z) = [1 + (h_0')^2]^{-1/2}$ and

$$\mathcal{T}_1 = \frac{1}{h_0^2}\mathcal{D} - \frac{2h_0'}{h_0^3}\mathcal{I}, \tag{2.23}$$

$$\mathcal{T}_2 = \mathcal{D}^3 + \frac{h_0'}{h_0}\mathcal{D}^2 - \left[\frac{(h_0')^2}{h_0^2} + \frac{h_0''}{h_0}\right]\mathcal{D} - \frac{h_0'\,h_0''}{h_0^2}\mathcal{I}, \tag{2.24}$$

$$\mathcal{T}_3 = -6\,h_0'\,h_0''\,\mathcal{D}^2 - 3\left[\frac{(h_0')^2\,h_0''}{h_0} + (h_0'')^2 + h_0'\,h_0'''\right]\mathcal{D}, \tag{2.25}$$

$$\mathcal{T}_4 = 15\,(h_0'')^2\,(h_0')^2\,\mathcal{D}. \tag{2.26}$$

When solving the base flow, the seed solution at the collocation points z is given by Torricelli's law (2.4), and at each step an increment $\Delta h_{0\,n} = -M\backslash\mathcal{N}[h_{0\,n-1}]$ is added to the previous solution, iterating until the residual of equation (2.3) is below a predefined tolerance.

Once the steady basic solution $h_0(z)$ is obtained at the N Chebyshev collocation points, the discrete axial velocity $u_0(z)$ is obtained using equation (2.2), and spatial derivatives are calculated resorting to the differentiation matrices D_t.

Regarding the perturbed field, the problem is formulated also in matrix form. If the vector $\phi(z,t) = [h_1(z,t), u_1(z,t)]$ and the matrix $\mathcal{A}$ containing the governing equations (2.6)-(2.8) are introduced, the linearized system reads

$$\frac{\partial}{\partial t}\begin{bmatrix} h_1 \\ u_1 \end{bmatrix} = \begin{bmatrix} \mathcal{A}_h^c & \mathcal{A}_u^c \\ \mathcal{A}_h^m & \mathcal{A}_u^m \end{bmatrix}\begin{bmatrix} h_1 \\ u_1 \end{bmatrix}, \tag{2.27}$$

where the linear differential operators are

$$\mathcal{A}_h^c = -\frac{Q}{h_0^2}\mathcal{D} + \frac{Q\,h_0'}{h_0^3}\mathcal{I}, \tag{2.28}$$

$$\mathcal{A}_u^c = -\frac{h_0}{2}\mathcal{D} - h_0'\mathcal{I}, \tag{2.29}$$

$$\mathcal{A}_h^m = \sum_{t=1}^{4} s^{2t-1}\,\mathcal{T}_t - 12\nu Q\left(\frac{h_0'}{h_0^4}\mathcal{D} - \frac{(h_0')^2}{h_0^5}\mathcal{I}\right), \tag{2.30}$$

$$\mathcal{A}_u^m = 3\nu\left(\mathcal{D}^2 + \frac{2h_0'}{h_0}\mathcal{D}\right) - \frac{Q}{h_0^2}\mathcal{D} + \frac{2Q\,h_0'}{h_0^3}\mathcal{I}. \tag{2.31}$$

Boundary conditions have to be incorporated in (2.19) to calculate the spatial structure of the response. In particular, as explained before, in the experiments that were described with equation (2.27), we considered the evolution of disturbances that consist of fluctuating velocity while the contact line remains pinned, and therefore the only non-zero element of b corresponds to $u_1(0,t) = 1$. Once numerical values of $u_1(z,t)$ and $h_1(z,t)$ are solved, they have to be accordingly multiplied by the desired input amplitude. Since this linearized problem uses the Chebyshev's discretization scheme, the computation of $\hat{\phi}(z;\omega)$ is conveniently reduced to the solution of an inhomogeneous linear system, constituting a very efficient procedure to obtain the evolution of small disturbances.

2.3 Experimental set-up

The aim of the experimental campaign is to perform a parametrical study to assess the effect of the liquid viscosity, the injector size and the flow rate on the natural break-up of gravitationally stretched jets. Jets are generated using silicone oils with kinematic viscosities of 50, 100 and 200 cSt, injected through tubes with diameters ranging from 2.5 to 7 mm. Images of the break-up are acquired with a high-speed camera and analyzed with a home-made dedicated MATLAB® script.

The experimental set-up was designed to minimize disturbances coming from the ambient and the facility, although the energy distribution cannot be guaranteed to be uniformly distributed among all frequencies. Despite the fact that the mean velocity remains constant, the ambient noise introduces small fluctuations at the injector, while the contact line remains pinned. The mean flow rate at which the fluid is injected is close to the jetting-dripping transition to obtain a basic flow with a pronounced meniscus close to the injector.

2.3.1 General set-up

A sketch of the experimental facility is shown in Figure 2.4. It was originally designed and built for the present study. To minimize external disturbances such as vibrations and air currents, the injection system is placed on a leveled vibration isolation table, inside a PMMA chamber. Inside the chamber, a pole gives support to the injector, guaranteeing the verticality of the tube while allowing regulation of the height at which it is placed. A Harvard Apparatus PHD Ultra Syringe Pump (A) allows the selection of the flow rate and impulses the fluid through a 4mm Legris tube. The silicone oil exits the injector (B) and accelerates under gavity, resulting in a stretched jet which breaks up downtream. A high-speed camera (C) acquires images of the break-up region at 1000 Hz, which are recorded using a computer (D). The images are later analized with a MATLAB® script in order to obtain the temporal evolution of the intact length and radius of the jet, as well as the volume of the detached liquid droplets.

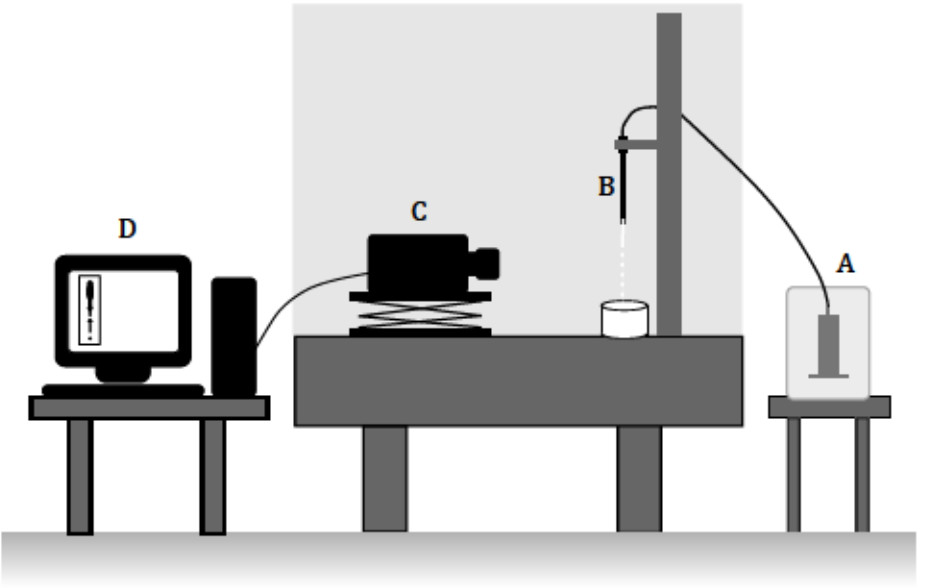

Figure 2.4: Scheme of the experimental facility used to study the natural break-up.

Materials The liquid jets are generated using Sigma-Aldrich silicone oils injected through stainless steel Tubca tubes. The materials have been selected to assess the influence of viscosity and size of the injector, and are listed in Tables 3.1 and 3.2.

The tubes are named after their outer diameter D_o. However, only their inner diameter D_i is relevant to the flow, since the wall of the injectors are trimmed at their end to ensure the pinning of the contact line at the inner radius. The tube length l_i is sufficiently large to guarantee a fully developed Poiseuille velocity profile at the outlet.

Although the working fluids cover a wide range of kinematic viscosities, they present similar densities and surface tensions. The maximum force that the syringe pump can exert limited the upper viscosity value to $\nu = 200$ cSt, a value for which flow rates $Q \leq 0.6$ ml/s could be injected. The ambient temperature during the experiments was 25.0 ± 2.3 °C, so that the relative variations in viscosity were always below 2%. It should also be noted that the viscosity of the liquids was too small for recoiling to be observed after the break-up events.

ν [mm^2 s^{-1}]	ρ [kg m^{-3}]	σ [mN m^{-1}]
50	960	20.8
100	965	20.9
200	970	21.1

Table 2.1: Properties at 25°C of the silicon oils used in the experiments.

D_e [mm]	D_i [mm]	l_i [mm]
2.5	2	170
4.5	4	225
6	5.5	225
7	6.5	225

Table 2.2: Dimensions of the injectors used used in the experiments.

2.3.2 Experimental procedure

The basic flow in each experiment is determined by the kinematic viscosity of the fluid ν, the injector diameter D_i and the constant flow rate Q. The latter was imposed using the syringe pump, after verifying that the advance of the piston did not introduce energy in an unstable frequency. We checked this experimentally by substituting the pump by a pressurized chamber and incorporating fuses to the feeding line to control the flow rate, and observed that the intact lengths were smaller than those obtained with the syringe pump. Since flow rates were close to the jetting–dripping transition, an important feature of the pump was the possibility of programming the injection, starting with a constant flow rate which was linearly decreased until the target value was reached. This was essential in the case of jets with the lowest velocities, where it was mandatory to first inject a higher flow rate to generate the jet and then reduce it to the desired value. This is related to the hysteretic behavior of the jetting–dripping transition at high Bond numbers (Clanet & Lasheras, 1999; Rubio-Rubio *et al.*, 2013; Rubio-Rubio, 2016). Moreover, it was toilsome in the case of the tubes with highest diameter to guarantee that capillary forces prevented the ambient air from entering the injector when the experiment was stopped. Therefore, higher initial flow rates were demanded for larger tubes to get rid of the bubbles before performing valid measurements of the jet break-up.

Once the jet was established, the height of the injector was regulated to locate the break-up region within the scope of the high-speed camera. The jet under study was uniformly illuminated with backlighting and a light diffuser. Typically, images were acquired during 5 s at 1 kHz. The latter value of the temporal resolution was chosen due to the fact that the highest observed interfacial disturbance frequencies were always below 200 Hz. Two types of videos were recorded: The first type aimed to capture the temporal evolution of the instantaneous jet length and the detachment of drops and ligaments from its downstream end. Since the break-up length presented a substantial dispersion,

the axial region of interest was large, with a length usually ranging between 8 and 15 cm. Therefore, a second type of video with a greater magnification was also required, in order to capture in detail the temporal evolution of the jet radius at several selected stations, and recorded along 3.5 cm in the axial direction of the jet. These movies were recorded slightly upstream, at a ditance from the injector smaller than the break-up length, where the amplitude of perturbations could be easily measured to determine the frequency of the dominant disturbances.

For given values of ν, D_t and Q, the experiments were repeated a minimum of three times, ensuring to eliminate the influence of particular conditions at the laboratory, such as accidental noise or temperature variations.

The postprocessing of the movies was performed with a MATLAB® script which was specifically developed for the present study. As stated before, in the first type of acquisitions the aim was to determine the temporal evolution of the jet length and its radius, and to compute the volume of the detached drops and ligaments. To this end, each frame was enhanced and analyzed. Then, the image contours corresponding to the liquid–air interface were detected, and the fluid elements were classified as filament, ligaments or drops. The jet length, $L(t)$, was measured in each frame and stored, and whenever it decreased with respect to the previous time step, a pinching event was detected at a distance L_b. In those cases, the fluid elements which had just detached were identified as drops or ligaments according to their aspect ratio, and their volume was computed. Following this procedure, the information about the evolution of the jet length, pinching frequencies and distribution of drop sizes became available.

To study the frequency of the most unstable perturbations, the videos with greater zoom were analyzed. After enhancement and contour detection, the local radius was stored as a funtion of time at several axial positions. Subsequently, a spectral analysis was performed at each coordinate to extract the frequency of the most amplified disturbances. Although it would have also been interesting to study the perturbations closer to the injector, their small amplitude made this impossible with the available experimental resources.

2.4 Results

2.4.1 Experimental results

The experiments performed cover values of the Weber number ranging from 0.002 to 3.79, and values of the Bond number from 0.45 to 4.77.

Let us first present the results of a typical natural break-up experiment. Small velocity fluctuations coming from the experimental facility are convected downstream, until they produce the pinching of the jet when their amplitude becomes sufficiently large. Since initial disturbances are of small amplitude, the associated fluctuations of the jet radius can not be distinguished with our equipment close to the injector. Therefore, our observations focus on the region of the jet close to the break-up position. Figure 2.5 shows a short temporal sequence of the natural break-up observed in our experiment of a jet with $\nu = 50$ cSt, $D_i = 6.5$ mm and $Q = 0.17$ ml/s, which will hereafter be referred to as the reference jet. In the captured region, the amplitude of disturbances is of the order of the local radius of the jet. The disturbed interface does not present the initial sinusoidal shape anymore but exhibits mass accumulations at certain places along the jet. Quasi-spherical drops are connected by thin threads, a fact that has been pointed out by many authors (see Eggers & Villermaux (2008) and references therein). Break-up takes place at the upper or lower throats connecting the bulges to the threads, resulting in the detachment of drops and/or ligaments. The latter can subsequently break into several pieces for high enough viscosities, and then evolve into smaller satellite drops (spherules).
Figure 2.6 shows a longer record of the temporal evolution of the jet length $L(t)$ for the reference case. It can be observed that pinchings occur at different positions L_b without a clear preferred frequency. These deviations are explained by the fact that the experiment presents only natural noise, and therefore a wide range of perturbations of several amplitudes and wavelengths grow simultaneously along the jet, as observed in Figure 2.5. Ligaments of different lengths,

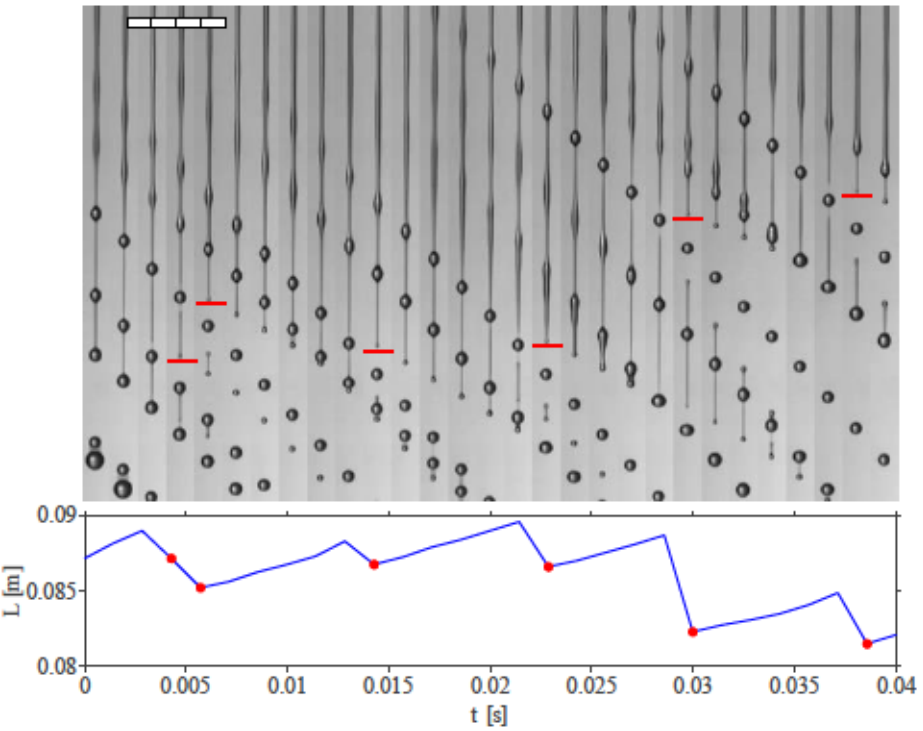

Figure 2.5: Break-up of the reference jet for which $\nu = 50$ cSt, $D_i = 6.5$ mm and $Q = 0.17$ ml/s. Top: Short sequence of images displayed at 500 Hz, at a distance of 7.1 cm from the injector. The white rectangle serves as a 1 cm long reference, and lines highlight pinching lengths. Botttom: Plot of the jet length $L(t)$, where dots indicate pinching lengths L_b.

comprising one or more wavelengths, detach from the jet.

Again for the reference case, Figure 2.7 presents a temporal series of the volume of the detached fluid elements. Drops and ligaments are distinguished according to their aspect ratio: drops originate when pinching occurs just above a tip bulge, and two types of ligaments are observed, namely those coming from a valley, in which case the volume of the satellite drop which later forms is small, and those comprising several wavelengths, from which one or more larger drops evolve. Pinching is irregular, without an observable periodicity in the volume

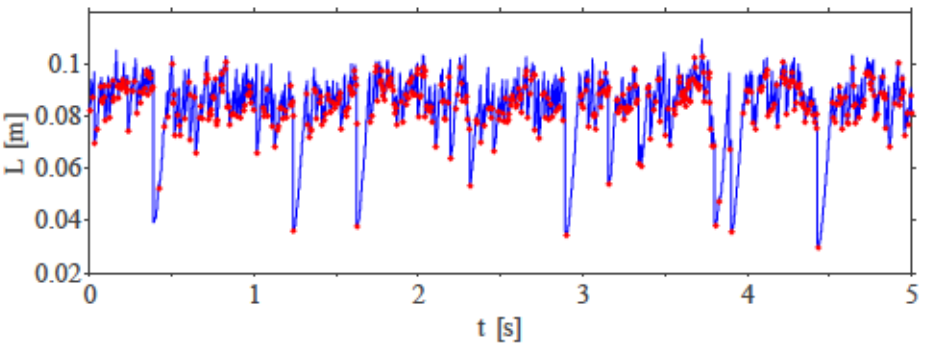

Figure 2.6: Temporal evolution of the jet length $L(t)$ of the reference jet. Dots indicate pinching lengths L_b.

or shape of the detached liquid volumes.

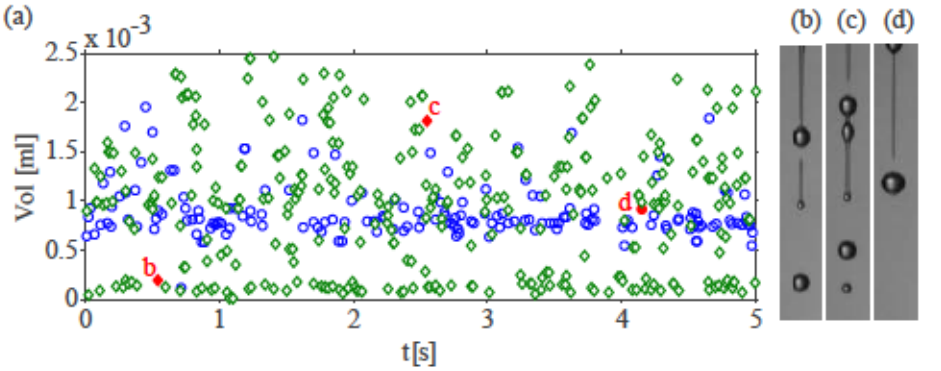

Figure 2.7: (a) Temporal series displaying the volume of the detached drops (circles) and ligaments (diamonds) for the reference jet. The labeled filled markers are illustrated with photographs on the right: (b) is a ligament of small volume consisting of a single valley, (c) is a larger ligament comprising several wavelengths and (d) is a single drop.

Further information can be extracted from the experimental measurements when the previous data regarding the pinching position and volumes is presented in the histograms displayed in Figure 2.8. Although presenting a large

dispersion, the pinching position in Figure 2.8(a) shows that the largest number of break-up events occur for $L_b = 0.09$ m, a value which will be used to characterize the experiment when presenting the results of parametric sweeps. This value must be accompanied by the standard deviation of L_b to provide a complete description of the break-up length. It can also be observed in Figure 2.8(a) that the distribution is not symmetric, presenting a slightly wider range of break-up locations upstream of the most repeated pinching position. We have observed that for natural break-up experiments, the measured L_b can be fitted to a Weibull probability density function,

$$f(x|a,b) = \frac{b}{a}\left(\frac{x}{a}\right)^{b-1} e^{-(x/a)^b}, \tag{2.32}$$

where scale parameter a and the dimensionless shape parameter b are positive. In particular, Weibull parameters take the values $a = 0.089$ m and $b = 12.2$ for the fit displayed as a solid line in Figure 2.8(a). As illustrated in Figure 2.9, the Weibull probability density function describes the distribution of L_b in the natural break-up of different stretched jets.

Regarding the detached volumes, Figure 2.8(b) reveals that ligaments present a large dispersion. However, a peak in the histogram is observed for the small volumes which correspond to the detachment of a single liquid bridge between two bulges, which corresponds to the event shown in Figure 2.7(b). On the other hand, Figure 2.8(c) shows that the volume of single drops presents less dispersion. Nevertheless, it is clear from Figures 2.8(b) and 2.8(c) that the natural break-up of gravitationally stretched jets is not suitable for monodisperse drop production, and that forcing the jet is necessary to reach this objective, as studied in Chapter 3.

Let us now assess the effect of variations of the parameters on the break-up dynamics. We still present as a reference case the jet with $\nu = 50$ cSt, $D_t = 6.5$ mm and $Q = 0.17$ ml/s. To ease visual comparison with other configurations, a fragment of the temporal series of $L(t)$ and photographs of selected consecutive break-up events is shown in Figure 2.10. When the injected flow rate

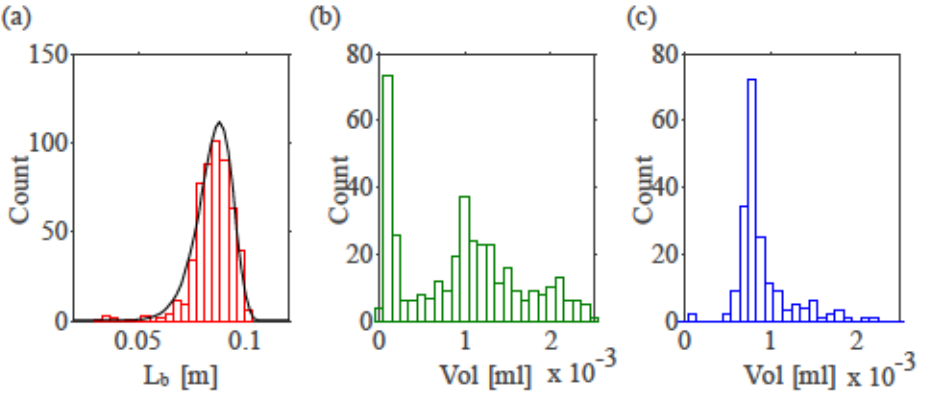

Figure 2.8: Histograms of parameters measured in the natural break-up of the reference jet. Pinching length L_b (a), including a Weibull fit (solid line). Volume of the detached drops (b) and ligaments (c).

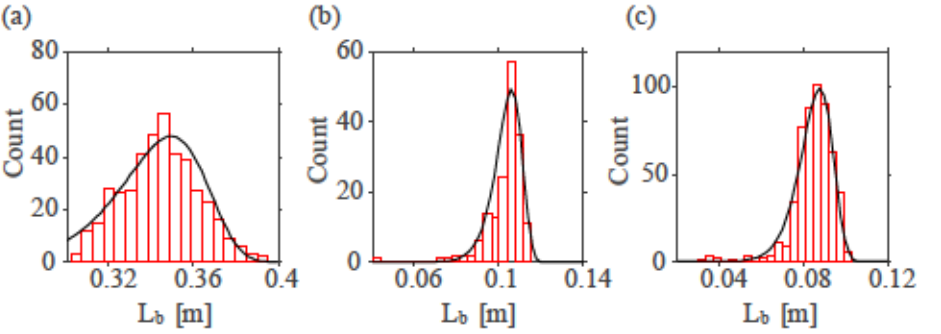

Figure 2.9: Histograms of the pinching length L_b, including a Weibull fit (solid line) for different jets: (a) Jet with $\nu = 50$ cSt, $D_i = 6.5$ mm and $Q = 0.9$ ml/s, where Weibull fit parameters are $a = 0.35$ m and $b = 18.1$, (b) Jet with $\nu = 50$ cSt, $D_i = 2$ mm and $Q = 0.17$ ml/s, Weibull parameters $a = 0.11$ m and $b = 18.7$, and (c) Jet with $\nu = 50$ cSt, $D_i = 6.5$ mm and $Q = 0.17$ ml/s, Weibull parameters $a = 0.09$ m and $b = 12.2$.

Q is increased while keeping the same liquid and injector, pinching occurs as displayed in Figure 2.11. For a jet with $\nu = 50$ cSt, $D_i = 6.5$ mm and $Q = 0.9$ ml/s, the behavior resembles that observed for a lower flow rate, but the intact length increases from $L_b = 0.09$ m to $L_b = 0.35$ m. When the fluid and flow

rate remain the same but a smaller injector is used, as in the case of a jet with $\nu = 50$ cSt, $D_i = 2$ mm and $Q = 0.17$ ml/s displayed on Figure 2.12, we only appreciate a slight increment on the pinching length to $L_b = 0.11$ m. However, the qualitative behavior presents significative changes when the viscosity is increased. In particular, Figure 2.13 for a jet with $\nu = 200$ cSt, $D_i = 6.5$ mm and $Q = 0.17$ ml/s shows that the break-up length duplicates with respect to the reference case to $L_b = 0.19$ m, while bulges are connected by very thin threads, a fact which is well documented in the existing literature (Eggers & Villermaux, 2008). In this case, it is observed that pinching takes place when these threads break at several positions simultaneously, originating multiple satellite drops.

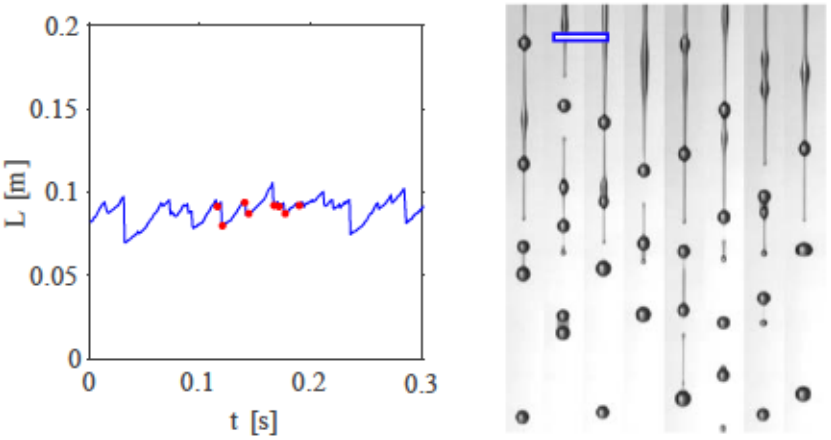

Figure 2.10: Temporal evolution of the length $L(t)$ of a jet with ν=50 cSt, D_i=6.5 mm and Q=0.17 ml/s. Dots indicate selected consecutive pinching events which are displayed on the right. The scale bar on the photographs is 1 cm long.

The measurements of the break-up length L_b are presented in Figures 2.14 and 2.15 as a function of the flow rate, Q. The plotted value of L_b is given for each jet by the most observed value and the associated standard deviation. It is important to emphasize that these error bars do not correspond to measuring errors or dispersion between different realizations under the same nominal conditions, but refer to the intrinsec fluctuations already discussed for Figure

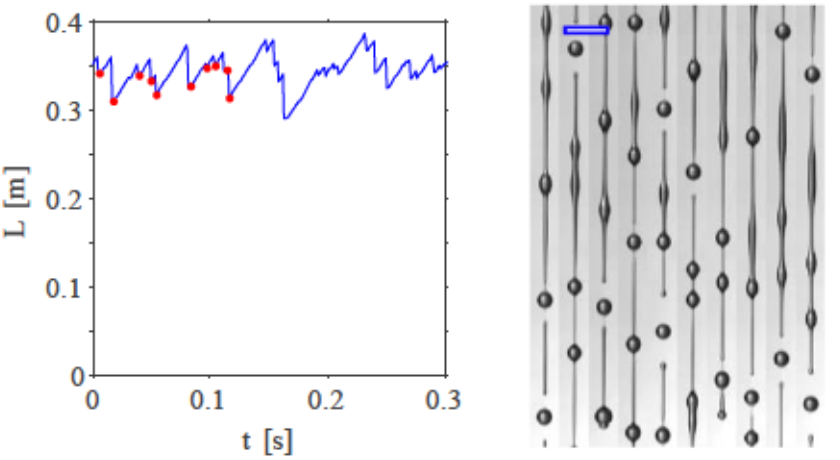

Figure 2.11: Temporal evolution of the length $L(t)$ of a jet with ν=50 cSt, D_i=6.5 mm and Q=0.9 ml/s. Dots indicate selected consecutive pinching events which are displayed on the right. The scale bar on the photographs is 1 cm long.

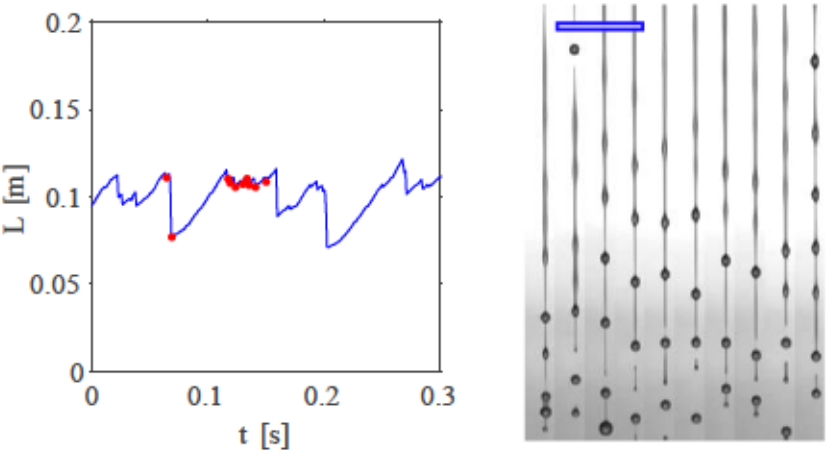

Figure 2.12: Temporal evolution of the length $L(t)$ of a jet with ν=50 cSt, D_i=2 mm and Q=0.17 ml/s. Dots indicate selected consecutive pinching events which are displayed on the right. The scale bar on the photographs is 1 cm long.

2.8(a). Since the data were acquired for several realizations of the same conditions, for simplicity we present the mean values of each parameter.

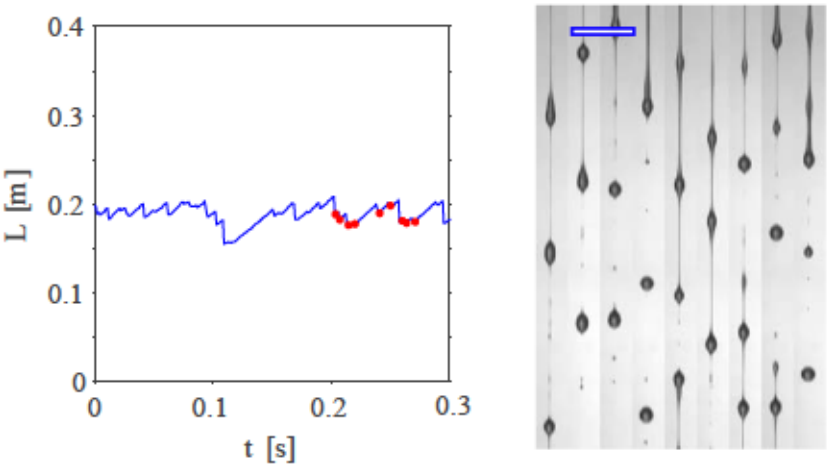

Figure 2.13: Temporal evolution of the length $L(t)$ of a jet with ν=200 cSt, D_i=6.5 mm and Q=0.17 ml/s. Dots indicate selected consecutive pinching events which are displayed on the right. The scale bar on the photographs is 1 cm long.

Figure 2.14 shows the dependence of the pinching length with the flow rate and injector diameter, for two different working liquids. For a fixed injector and liquid, the break-up length increases with Q as expected, with a mildly faster increase close to the critical value of Q associated with the jetting-dripping transition. When the fluid rate is kept constant, the use of larger injectors results in a slight decrease of the break-up length, at a position where, according to numerical calculations, all unperturbed jets would present very similar local radii. The effect of varying the working fluid is clearly appreciated in Figure 2.15. Increasing the viscosity raises the break-up length, with a substantial difference between $\nu = 100$ and $\nu = 200$ cSt. Measurements for an injector of $D_i = 2$ mm, shown in Figure 2.15(a) are consistent with the observations reported by Javadi *et al.* (2013).

It is essential to interpret these results taking into account the fact that the relative amplitude of the perturbed speed at the tube $\epsilon \equiv u_1(0)/u_0(0)$ is not the same in all these experiments. Higher viscosities are likely to damp noise

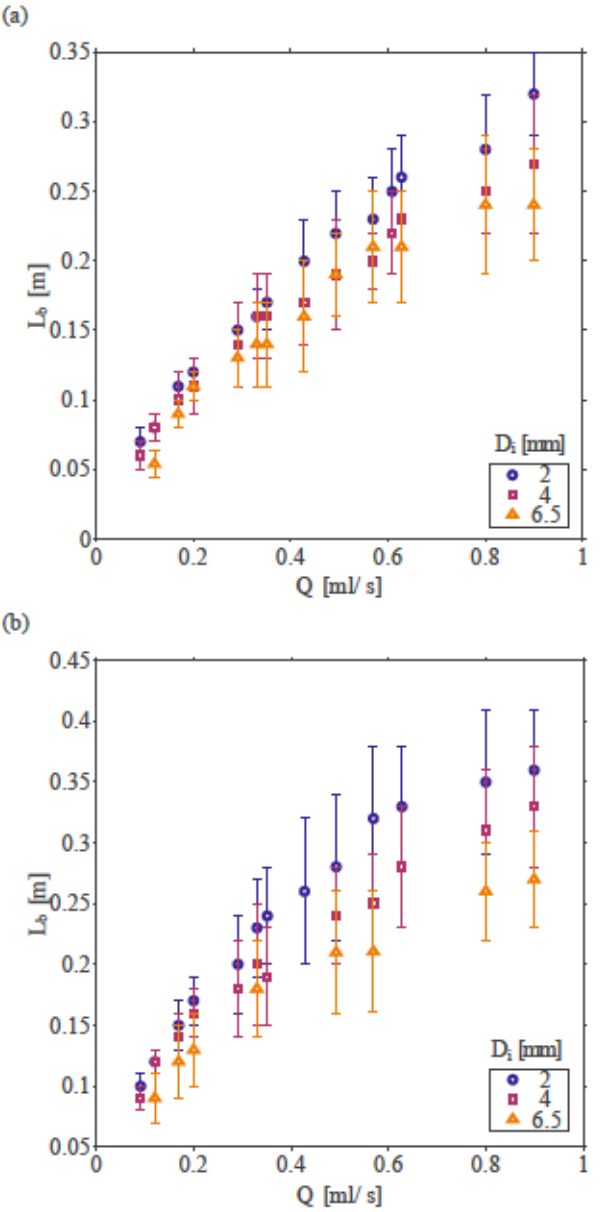

Figure 2.14: Break-up length L_b of unforced jets as a function of the flow rate Q, for different injector diameters D_i. The working fluid's kinematic viscosity is $\nu = 50$ cSt (a) and $\nu = 100$ cSt (b).

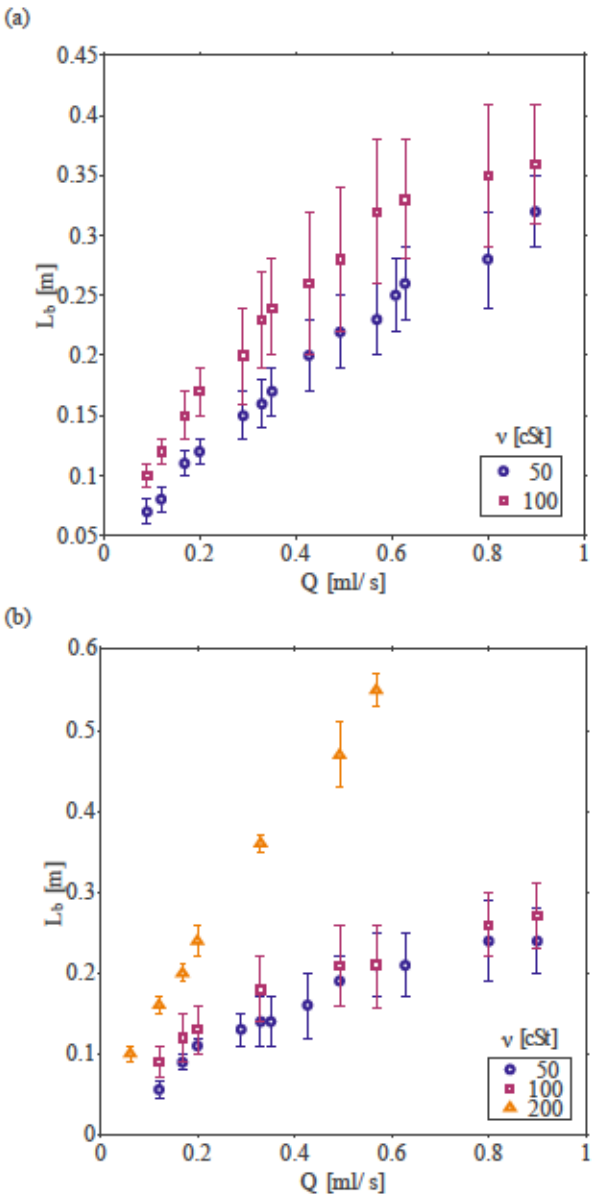

Figure 2.15: Break-up length L_b of unforced jets as a function of the flow rate Q, for fluids of different kinematic viscosity ν. The inner diameter of the injector is $D_i = 2$ mm (a) and $D_i = 6.5$ mm (b).

from the feeding line and therefore decrease the perturbed speed u_1. Meanwhile, larger tubes and lower flow rates reduce the basic speed u_0, increasing ϵ up to 10 times in our experiments. This disparity in ϵ conceals the damping of perturbations produced by either a more pronounced meniscus or an increase in the liquid viscosity.

We also extracted information regarding the frequency of disturbances responsible for the natural break-up, a parameter which had not been reported before for axially stretched jets as far as we know. We measured the most amplified frequency, ω_b, by performing a signal analysis on the temporal evolution of the radius of the jet at several fixed positions. The time series were averaged and post-processed using Welch's power spectral density estimate, using a minimum of 8 Hamming windows with 50% overlap. The value of ω_b was extracted from the dominant frequency in the spectrum. Figure 2.16(b) is an example of a typical spectrum in which, despite the data presenting a large dispersion, the most amplified frequency can be clearly identified.
Figure 2.16(a) presents the most amplified frequency ω_b as a function of the flow rate Q for three different fluid and nozzle combinations. For fixed values of ν and D_t, increasing Q results in higher values of ω_b. The experiments with $\nu = 50$ and $\nu = 200$ and the same injector size $D_t = 6.5$ mm, suggest that for a fixed flow rate ω_b slightly increases with the liquid viscosity. When comparing these results with those obtained with a smaller injector, $D_t = 4$ mm, and an intermediate viscosity of $\nu = 100$ cSt, the results indicate that ω_b decreses when using injectors of smaller diameter.

To ensure a good estimation of ω_b, we also implemented other methodologies. The power spectral density of the jet length $L(t)$ did not exhibit clear energy peaks at a preferential frequency, and was therefore discarded as a method for estimating ω_b. Another technique to measure ω_b is based on the assumption of non-dispersive disturbances. Specifically, since in the break-up region the local Weber number is high, the equation $\omega = k\ u_0$ can be used to relate the

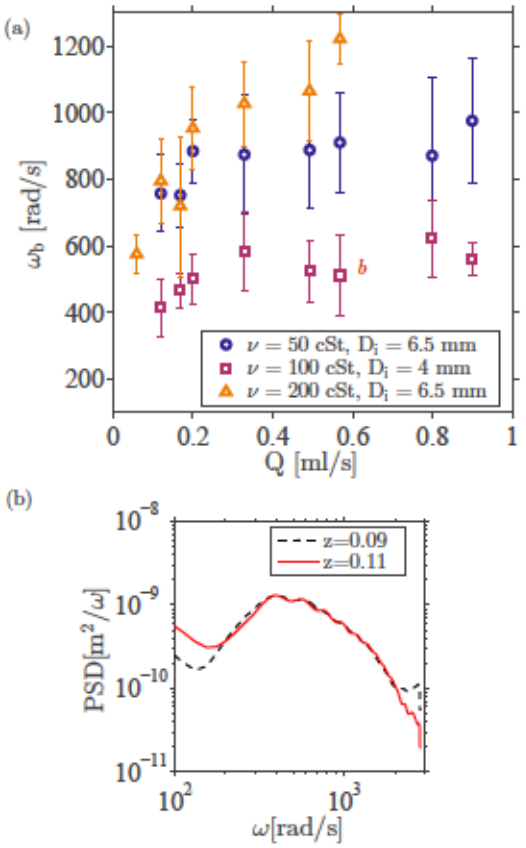

Figure 2.16: Frequency ω_b of the most amplified disturbances as a function of the flow rate Q (a), for three different flow configurations where the viscosity of the working fluid ν and the injector diameter D_i are varied. A detail of the marker referenced as b, with $\nu = 100$ cSt, $D_i = 4$ mm and $Q = 0.6$ ml/s, is shown in (b), where the spectra at two axial positions, $z = 0.09$ m and $z = 0.11$ m, exhibit peaks of energy at $\omega_b \simeq 400$ rad/s.

frequency ω, the local wavenumber k and the local base flow velocity u_0. The wavelength λ was obtained from photographs using a home-made MATLAB® script that measured the distance between consecutive bulges, allowing the estimation of the wavenumber, $k = 2\pi/\lambda$. The velocity of the basic flow $u_0(z)$ was computed by solving equation (2.3), checking that its value was consistent

with the velocity extracted from tracking the bulges advected by the jet. Figure 2.17 illustrates the use of this technique for a single time step, where for a jet with $\nu = 50$ cSt, $D_i = 6.5$ mm and $Q = 0.2$ ml/s the most observed perturbations present $\omega_b = 900$ rad/s, in agreement with measurements obtained from the signal analysis of $h(t)$ explained before. It should be mentioned that the measurement of ω_b from the wavelength is not always as robust as performing the signal analysis of radius fluctuations. Indeed, swellings appear between the crests of primary disturbances, a nonlinear effect which was experimentally observed for the first time by Rutland & Jameson (1971), and it is difficult to develop an image analysis routine that is able to distinguish both phenomena to properly measure the value of λ.

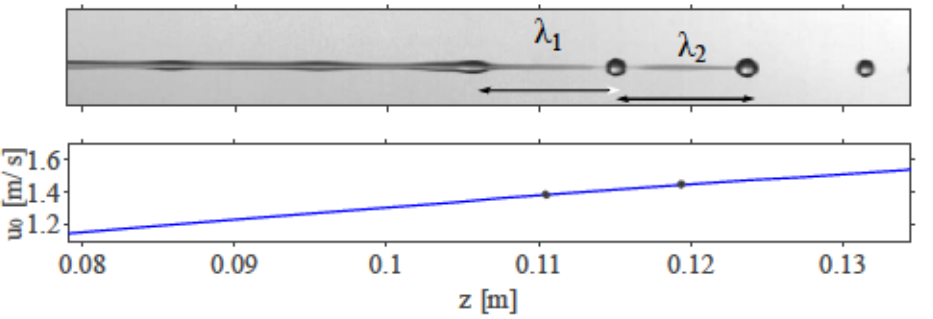

Figure 2.17: Estimation of the frequency of the most amplified disturbances for the natural break-up of a jet with $\nu = 50$ cSt, $D_i = 6.5$ mm and $Q = 0.2$ ml/s. Top: experiment where the wavelength λ is measured. Bottom: numerically calculated mean axial speed $u_0(z)$. The calculated $\omega_b = 900$ rad/s.

2.4.2 Results of the global frequency response analysis

A novel global frequency response analysis (GFRA) was implemented to examine the growth of disturbances of different frequencies on stretched jets. After validating this methodology with local stability theory, we will present a parametric study of the spatial evolution of perturbations, that allows the prediction of the pinching length and the most amplified frequency.

2.4.2.1 Validation

To validate the GFRA we consider the case of an infinite liquid cylinder, for which the classical parallel stability analysis can be applied and where, thus, both the local and global analyses should yield identical results.
Figure 2.18 illustrates the validation for a cylindrical jet with $\nu = 50$ cSt, $Q = 2$ ml/s and $D_t = 2$ mm. In the local spatial analysis, the dispersion relation for a cylinder derived by Guerrero *et al.* (2012) after perturbing and linearizing the one-dimensional equations (1.9)-(1.10) reads

$$D(\omega,k) = k^2\frac{\sigma}{\rho R^2} - k^4\frac{\sigma}{\rho} + \omega^2\frac{2}{R} - \frac{4Uk\omega}{R} + \frac{6\nu i k^2\omega}{R} + \frac{2U^2k^2}{R} - \frac{6\nu i k^3 U}{R} = 0. \quad (2.33)$$

The inset in Figure 2.18 presents the growth rate $-\Im(k^*)$ corresponding to the dominant capillary mode as a function of the frequency ω^*, obtained from equation (2.33). The most amplified frequency is $\omega_b = 320$ rad/s, which presents a growth rate $-\Im(k^*) = 0.047$. The main plot in Figure 2.18 presents results from the GFRA, showing the spatial evolution of the amplitude of the radius disturbance, $h_1(z)$ for different frequencies. After an initial region affected by the exit boundary condition, the amplification is exponential in space, indicating that the spatial growth rate becomes constant sufficiently far from the outlet. Indeed, when the slope of $h_1(z)$ in the latter region is compared with the growth rate in the inset of Figure 2.18, the agreement is perfect.

Our validation study was extended to different liquid viscosities and jet velocities, always finding that the spatial amplification predicted by our analysis perfectly reproduces the local dispersion relation for any frequency.

2.4.2.2 Amplification of disturbances

To study the evolution of the amplitude of inlet velocity disturbances, let us qualitatively examine the results for the reference case of a jet with $\nu = 50$ cSt,

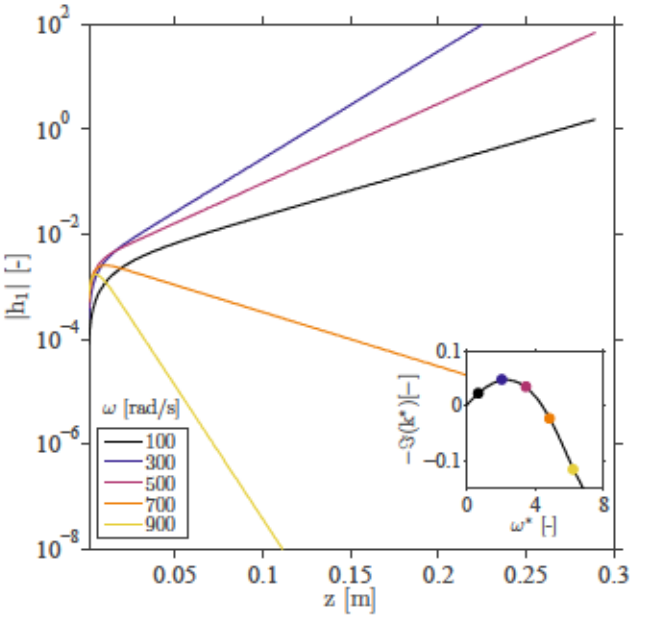

Figure 2.18: Comparison between results from a classical parallel spatial analysis and the global frequency response of a liquid cylinder with $\nu = 50$ cSt, $Q = 2$ ml/s and $R = 1$ mm. Main plot: Spatial evolution of the amplitude of the perturbed radius $h_1(z)$ calculated using the GFRA for different frequencies ω. Inset: Dimensionless growth rate $\Im(k^*)$ and frequency ω^* from the local dispersion relation, where the characteritic timescale is given by $t_\sigma = 0.007$ s. Dots indicate the growth rate obtained with the GFRA.

$Q = 0.2$ ml/s and $R = 2$ mm.

Figure 2.19 shows the response of the jet radius to velocity disturbances of frequency $\omega = 400$ rad/s at a fixed time. Due to the stretching effect of the base flow, the disturbance wavelength increases downstream. We also present the spatial evolution of the amplitude, which exhibits a substantial damping in the region near the exit, indicating the stabilizing effect of stretching on the Plateau-Rayleigh instability. When z becomes sufficiently large, the elongation rate of the base jet becomes too small to stabilize the capillary instability, and

disturbances begin to grow downstream. This stabilizing effect is just the spatial counterpart of the temporal kinematic mechanism described by Tomotika (1936), where a liquid cylinder was uniformly stretched, so that its radius and the wavelength of perturbations are both a function of time. Such a cylinder breaks up into drops, corresponding to initially stable wavelengths which are stretched until they become unstable.

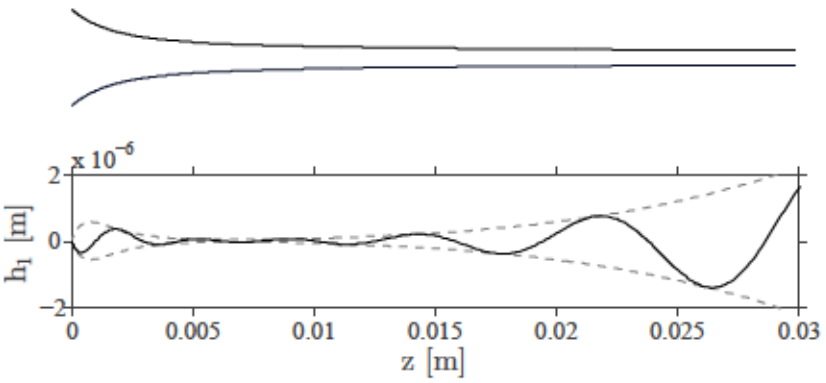

Figure 2.19: Response of the perturbed jet radius close to the injector, corresponding to an input frequency $\omega = 400$ rad/s on the reference jet. Dashed lines indicate the spatial evolution of the amplitude h_1, while the solid line is the response at a fixed time, $\Re(\hat{h}_1)$. At the top, the radius of the basic jet h_0 allows visualization the non-parallelism of this region of the flow.

Figure 2.20 shows the spatial growth of the radius of disturbances, $h_1(z)$, for different frequencies ω. It can be observed that the amplitude of perturbations does not present the exponential dependence found in non-stretching jets. In particular, we have compared our results with the asymptotic theory proposed by Senchenko & Bohr (2005). These authors found that $|\hat{h}_1| \propto \exp\left(z^{1/8}\right)$ as $z \to \infty$ in the free-fall region, a result independent of the frequency and viscosity contrary to our experimental and numerical findings. Moreover, in contrast with the parallel case, the most amplified frequency in the global analysis varies with the axial coordinate. Although disturbances with higher frequencies

present larger initial dampings, they are able to gain more energy downstream, implying the existence of an *optimal frequency* ω_b.

The damping near the meniscus zone takes place because mass conservation requires an amplitude reduction accompanying the strong elongation, although for higher frequencies other effects, that have not been specifically studied, are responsible for the non-monotonic decay seen in Figure 2.20. A local interpretation provides insight on the amplifying mechanism in the quasi-parallel region located far from the meniscus, whose extension increases as the local elongation rate diminishes, and, correspondingly, the *locally* most unstable perturbations present maximum growth rate .

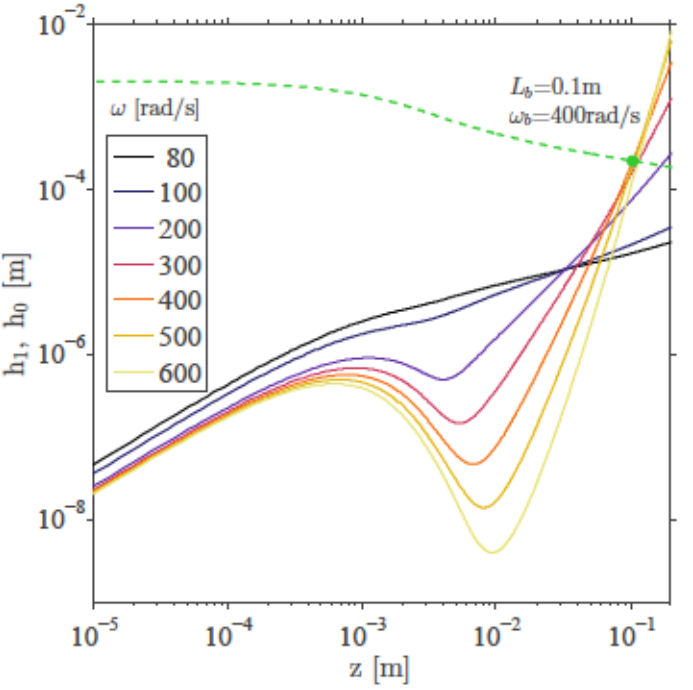

Figure 2.20: Spatial evolution of the amplitude of the perturbed radius $h_1(z)$ for the reference jet for different frequencies ω and an initial amplitude $\epsilon = 0.01$. Break up takes place at a distance $L_b = 0.11$ m where the amplitude of the optimal frequency $\omega_b = 400$ rad/s equals the local radius of the jet h_0 (dashed line).

Note that in Figure 2.20 the amplitude of the radius disturbance at the injector exit is zero, since velocity fluctuations occur while the contact line remains pinned. For a further understanding of the process, Figure 2.21 shows the amplification of the perturbation velocity $|\hat{u}_1(z)|$, normalized by its value at the injector exit. As in the previous figure, the initial damping of higher frequencies can be clearly appreciated, and we indicate the position z_m at which each frequency takes its minimum value. This is the distance to the injector where it would be optimal to induce a disturbance of a given frequency in order to minimize the intact length of the jet for that perturbation. We have also plotted for each frequency the position at which perturbations would be destabilized according to the local theory, at z_{dl} accomplishing the Rayleigh cut-off $k(z_{dl})h_0(z_{dl}) = 1$, assuming a non-dispersive behavior $k(z) = \omega/u_0(z)$. Although part of the damping can be attributed to the fact that high-frequency perturbations initially remain stable until they are sufficiently elongated, the difference between z_m and z_{dl}, which is different for different basic flows, indicates some additional stabilization is provided by the meniscus. Higher frequencies do not only present larger damping, but the position z_m is located further downstream. In Figure 2.21 we also indicate the position at which disturbances recover unitary amplitude, z_r, which can be interpreted as the delay in the growth due to the presence of the meniscus, and which has been dentified in the present Thesis for the first time. As in Figure 2.20, we observe, in agreement with the work of Frankel & Weihs (1985), that although shorter wavelengths start to grow later, they present larger magnification sufficiently far downstream.

2.4.2.3 Parametric study

The amplification predicted by linear theory does not extend indefinitely, since the nonlinearity eventually becomes important when the perturbation grows. However, since the growth is approximately exponential, these final stages take

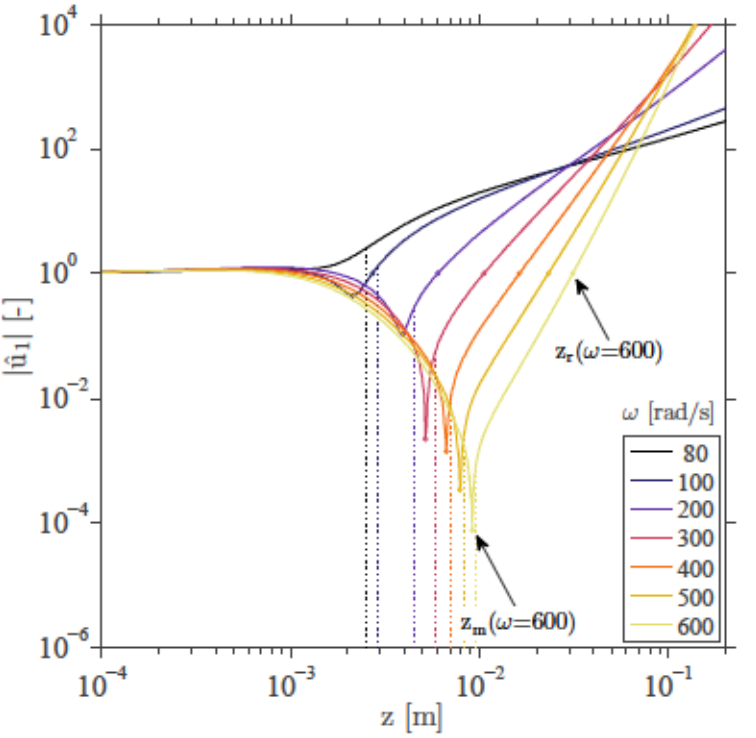

Figure 2.21: Spatial evolution of the normalized amplitude of the perturbed axial speed $|\hat{u}_1|(z)$ on the reference jet for different frequencies ω. For each frequency, dots indicate the position at which minimum and unitary amplitude are reached, z_m and z_r. Vertical dotted lines indicate the position at which each frequency is destabilized according to a local analysis.

place far from the nozzle, justifying a linear approach to estimate the position at which break-up occurs (Kalaaji *et al.*, 2003). The results of the GFRA shown in Figure 2.20 predict the break-up to occur at $z_b = 0.11$ m for $\omega_b = 400$ rad/s when all frequencies present the same initial amplitude $\epsilon = 0.01$. However, it is important to note that break-up could be due to other frequencies if the initial amplitudes were unevenly distributed. This information is presented in Figure 2.22(a), where the break-up position L_b is shown as funtion of ω for different values of ϵ. For a fixed value of ϵ, the minimum break-up length is obtained

for the optimal frequency, but slowly increases for larger ω, suggesting that the dependence of L_b on ω is rather weak. It can also be observed that a given value of L_b can be attained with different (ω, ϵ) combinations, provided that the energy distribution of perturbations of different amplitudes is not even. When the experimental facility presents white noise, larger values of ϵ result in break-up occuring closer to the injector due to lower frequencies, as shown in Figures 2.22(b) and 2.22(c).

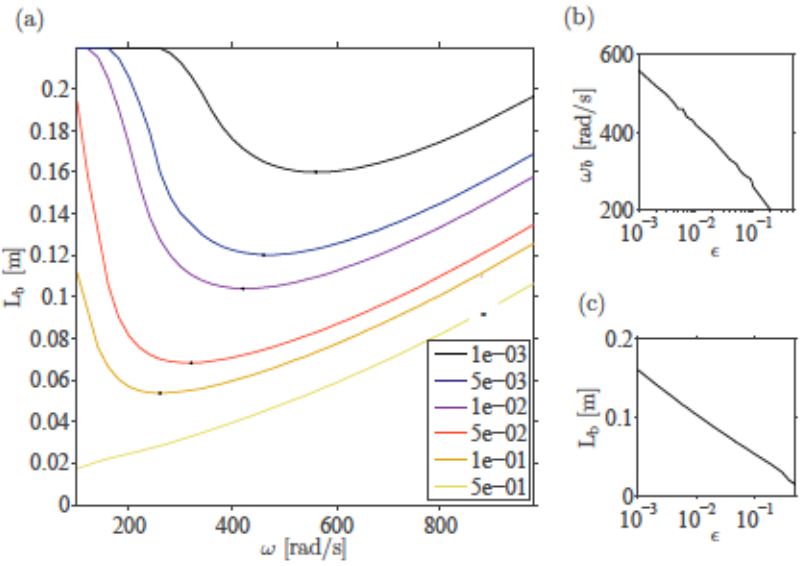

Figure 2.22: (a) Dependence of the break-up length L_b of the reference jet on the frequency ω, for different initial amplitudes of disturbances ϵ. For each value of ϵ, dots indicate the optimal frequency. (b) Optimal frequency ω_b and (c) break-up length due to ω_b, as functions of ϵ.

The results of the GFRA also allow to assess the effect of varying the flow configuration on the spatial evolution for the amplitude of disturbances. Let us fix the frequency of disturbances at $\omega = 400$ rad/s, and study its evolution on the reference case, with $\nu = 50$ cSt, $D_i = 2$ mm and $Q = 0.2$ ml/s, which is plotted as case A in Figure 2.23. First, we examine the effect of injecting

a different flow rate by comparing it to the amplification on a less slender jet with $\nu = 50$ cSt, $D_i = 4$ mm and $Q = 0.9$ ml/s, presented as case B in Figure 2.23. For larger Q the position at which disturbances begin to grow, z_m, moves downstream, and the growth rate also decreases. In this case, perturbations are advected downstream faster, and therefore experience both the initial damping and delayed growth for a shorter time. In case Q and ν are kept as in the reference case, but the injector diameter is increased to $D_i = 6.5$ mm, case C in Figure 2.23, the region close to the injector where damping occurs is also enlarged. Finally, when $Q = 0.2$ ml/s and $D_i = 2$ mm and we compare the amplification on jets generated with $\nu = 50$ and $\nu = 200$ cSt, cases A and D respectively, we observe that, as expected, a higher viscosity delays the growth of disturbances.

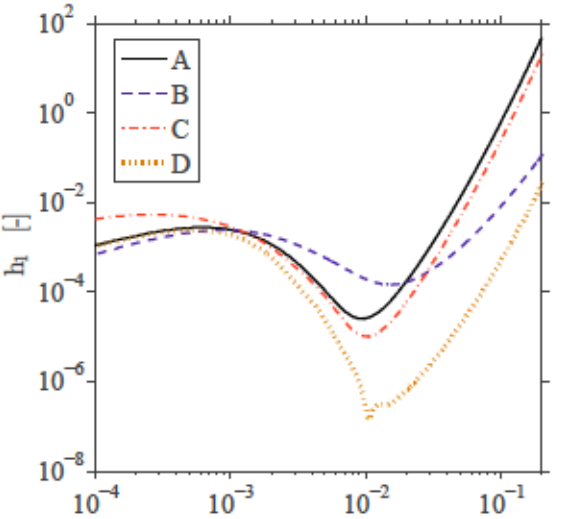

Figure 2.23: Spatial evolution of the normalized amplitude of the radius perturbation, $|\hat{h}_1|(z)$, for different jets and $\omega = 400$ rad/s. Case A corresponds to the reference jet with $\nu = 50$ cSt, $D_i = 4$ mm and $Q = 0.2$ ml/s, B is $\nu = 50$ cSt, $D_i = 4$ mm and $Q = 0.9$ ml/s, C is $\nu = 50$ cSt, $D_i = 6.5$ mm and $Q = 0.2$ ml/s, and D is $\nu = 100$ cSt, $D_i = 4$ mm and $Q = 0.2$ ml/s.

Figure 2.24 illustrates the effect of changing the flow parameters on the break-up behavior. When the same fluid and injector are used but a larger flow rate is injected, Figure 2.24(a), the optimal frequency is higher, since a longer jet allows higher frequencies to amplify. In Figure 2.24(b) a larger nozzle is used, and the $L_b(\omega)$ curves are displaced towards larger intact lengths and break-up frequencies. However, the largest change occurs when considering a more viscous liquid, which according to Figure 2.24(c) results in a more pronounced frequency selection. Note that in general terms ω_b stands out more with respect to other frequencies when a longer nearly parallel region exists in the unperturbed jet.

In the following subsection, the GFRA predictions are compared to experimental measurements.

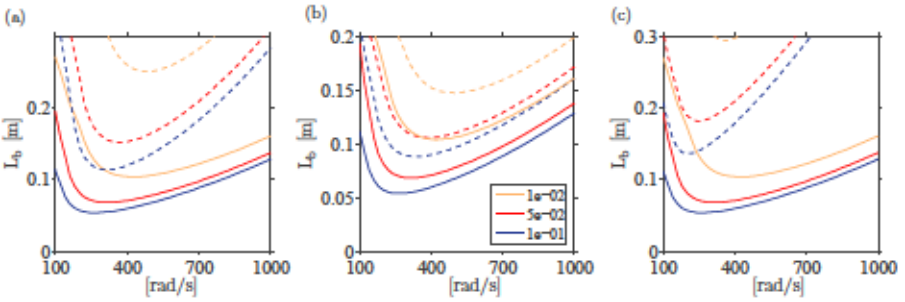

Figure 2.24: Dependence of the break-up length L_b of the reference jet with the frequency ω and initial amplitude of disturbances ϵ, comparing the reference case (solid lines) with different flows (dashed lines). In (a), the flow rate of the jet is increased to $Q = 0.8$ ml/s, in (b) the injector is larger, $D_i = 6.5$ mm, and in (c) a more viscous fluid is used, $\nu = 100$ cSt.

2.4.3 Comparison between the experiments and the linear frequency response analysis

To compare the experiments and the stability results, the noise of the experimental facility must be determined. The noise-reduction features of the experimental set-up, i.e. the vibration isolation table and the PMMA chamber, are

of major importance in reducing the amplitude of disturbances at the injector. However, as discussed before, the governing parameters ν, D_i and Q also influence the value of ϵ. Smaller tube diameters increase the inertia of the feeding line, while viscosity damps the disturbances. Regarding the flow rate, we have found no evidence that the syringe pump has a significative effect on the velocity fluctuations u_1, a fact that has been verified by changing the injection system to a pressurized chamber, and by comparing the pressure fluctuation signals for natural pinching of jets with different Q in the controlled break-up facility. However, for a given value of u_1, higher flow rates result in a reduction of the relative amplitude of disturbances, since $\epsilon = u_1/u_0$. In particular, when Q is swept from 0.1 to 0.9 ml/s, ϵ descreases one order of magnitude. For the same reason the value of ϵ for a fixed flow rate also increases for larger injector diameters, since $u_0 = 4Q/(\pi D_i^2)$.

We have therefore decided to experimentally estimate a value of u_1 for each combination of fluid and injector, whereas ϵ varies with the flow rate. This is accomplished by the least squares method described as follows. A numerical simulation was performed for each experiment, with a dimensionless velocity forcing of unitary amplitude. The dimensionless amplitude of disturbances $h_1(z;\omega)$ was stored for frequencies in the range $\omega \in [80, 1000]$ rad/s. For a test value of u_1, $h_1(z;\omega)$ was dimensionalized and the pinching position, L_b, and break-up frequency, ω_b, were determined. The predicted value of L_b was compared to the experimentally observed one, and the relative squared differences were calculated for each flow rate. The process was repeated for different values of u_1, selecting the one which minimized the sum of the squared differences.

As shown in Figure 2.25, the intact length predicted by the GFRA presents is in good agreement with the experimental results. In Figure 2.25(a) the comparison is made for different injectors, with better agreement for smaller diameters. However, we have checked that in the case of $\nu = 200$ cSt and $D_i = 6.5$ mm (not shown), the agreement is excellent. In Figure 2.25(b) we use the GFRA to make predicions for a fixed injector and two different viscosities. Note that the *only* free parameter of the comparison, namely u_1, remains fixed for a given

fluid and injector diameter. Contrary to what was expected, the fitted value of u_1 increases when either the liquid viscosity or the injector diameter increase. At this point, an explanation of this counterintuitive behavior has not been found.

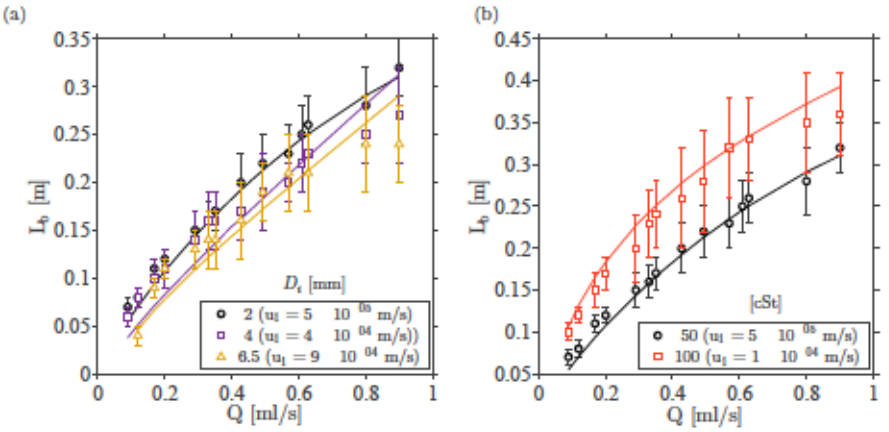

Figure 2.25: Comparison between experimental measurements (symbols) and GFRA predictions (solid lines) of the break-up length L_b as a function of the flow rate Q. The amplitude of velocity fluctuations at the injector u_1 [m/s] for the GFRA predicions is indicated for each (ν, D_i) combination. The jets are (a) $\nu = 50$ cSt, injected through nozzles of different diameters D_i, and (b) obtained using two different working liquids issuing from an injector with $D_i = 2$ mm.

In contrast with the break-up lengths, the frequencies predicted by the GFRA are much lower than those experimentally observed, as displayed in Figure 2.26. This could be related to the behavior of the function $L_b(\omega, \epsilon)$ shown in Figures 2.22, 2.24 and 2.27, where it is deduced that for a fixed value of ϵ there is a wide range of frequencies which could produce the break-up at intact lengths close to the minimum value.

We therefore proposed to obtain u_1 using a different approach. In Figure 2.27, for each flow configuration the contours of $L_b(\omega, \epsilon)$ obtained with the GFRA are displayed together with the experimental intact length and frequency

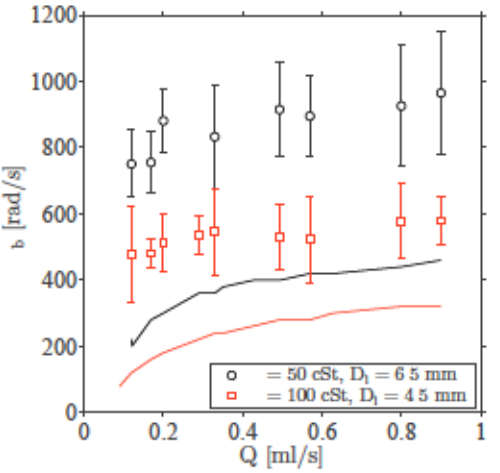

Figure 2.26: Comparison between experimental measurements (markers) and GFRA predictions (solid lines) of the break-up frequency ω_b as a function of the flow rate Q, for two different fluids and injectors. The amplitude of velocity fluctuations at the nozzle exit adopted for the GFRA predictions are $u_1 = 0.0009$ m/s and $u_1 = 0.001$ m/s respectively.

(crosses). The value of ϵ is determined as the interpolated contour that crosses the experimental data point. However, this procedure leads to values of $\epsilon > 0.5$, which besides being unrealistically large, would invalidate a linear analysis. Indeed, note that the perturbations estimated for the facility described in Chapter 3 are much smaller than the values deduced from the procedure explained in the present paragraph.

Optimal frequency Considering the strong disagreement between the linearly predicted and experimentally measured optimal frequency, we have also addressed the frequency selection resorting to a nonlinear stability analysis. The implementation of such analysis, based on the direct simulation of equations (1.9)-(1.11), shall be described in Chapter 3. Figure 2.28 shows the results of the nonlinear stability analysis of a jet whose exit velocity is stimulated with white noise. The maximum relative amplitude of such disturbances is chosen as

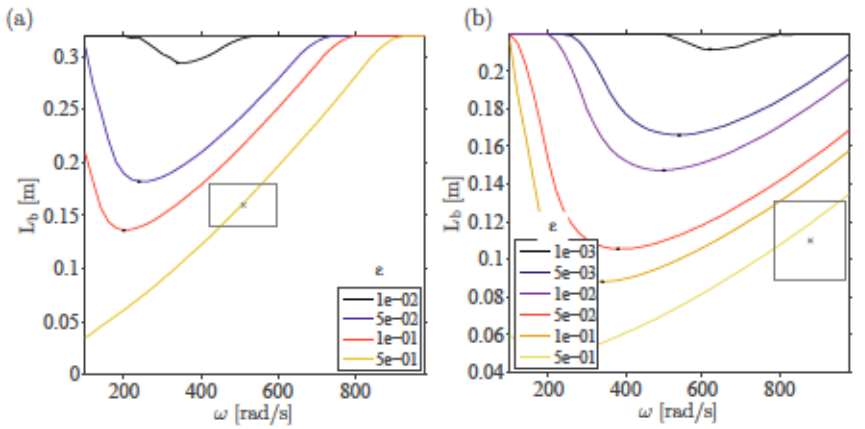

Figure 2.27: Dependence of the break-up length L_b of the jet with the frequency ω, for different initial amplitudes of disturbances ϵ according to the GFRA. The cross and its surrounding box indicate the experimental measurements of L_b and ω_b and their standard deviation. (a) $\nu = 100$ cSt, $D_i = 4$ mm and $Q = 0.2$ ml/s, and (b) $\nu = 50$ cSt, $D_i = 6.5$ mm and $Q = 0.2$ ml/s.

$\epsilon = 1$, in order for the jet to exhibit radial displacements of the interface which can be accurately obtained. As the measuring position moves downstream from Figure 2.28(a) to (b), a frequency selection process becomes evident. In Figure 2.28(c), $h(t)$ shows that perturbations are not sinusoidal anymore. Comparing (b) and (c), we conclude that larger frequencies are more amplified downstream. Although these results are in qualitative agreement with the GFRA computed for the same jet, the latter is unable to capture the nonlinear stages of disturbance evolution.

To sum up, both the linear and nonlinear analyses predict the amplification of perturbations as they are advected along the jet, as well as the emergence of a local preferred frequency from the noisy input whose value increases downstream. The jet thus acts as a noise filter and amplifier.

As a final comment regarding the natural break-up of jets, we have also estimated the amplitude of velocity fluctuations associated with the ambient noise

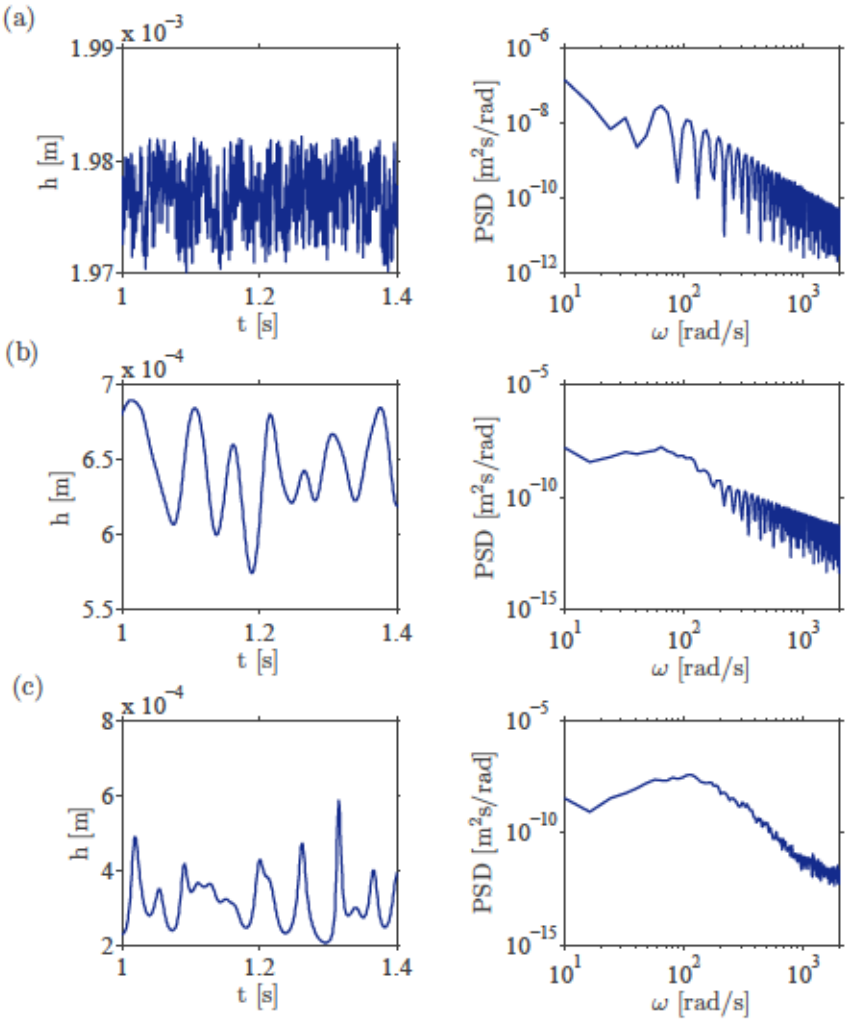

Figure 2.28: Nonlinear analysis of a jet with $\nu = 100$ cSt, $D_i = 4$ mm and $Q = 0.2$ ml/s, and white noise fluctuations of amplitude $\epsilon = 1$ the axial velocity at the injector exit. Temporal evolution of the radius of a jet $h(t)$ (left column), to determine the frequency ω of the most amplified perturbations through a PSD (right column), at three different axial positions (a) $z = 0.1$ cm, (b) $z = 4.5$ cm and (c) $z = 9$ cm.

in the facility described in Chapter 3. Measurements with a pressure sensor were acquired during experiments without controlled forcing. Figure 2.29(a)

shows a typical PSD of a pressure signal $p_{eff}(t)$, which was used to estimate the amplitude of fluctuations $p_1(\omega)$ with frequency increments of $d\omega = 5$ rad/s. Although the spectrum concentrates more energy at higher frequencies, it is quite uniform except for the existence of a peak at $\omega \simeq 315$ rad/s of unknown origin. We estimated the axial velocity fluctuations $u_1(\omega)$, using $p_1(\omega)$ as an input to Bernoulli's extended equation, as will be explained in detail in Chapter 3. In the example of Figure 2.29(a), we observe that disturbances with $\omega = 315$ rad/s present an amplitude $u_1 = 5 \times 10^{-5}$, yielding $\epsilon \simeq 3 \times 10^{-3}$. We determined the noise present in our facility for four flow configurations analyzed in the following chapter, finding that the spectrum of pressure fluctuations is similar, providing values in the range $3 \times 10^{-3} < \epsilon < 1 \times 10^{-2}$. However, the much larger measured values of the break-up frequency remain unexplained.

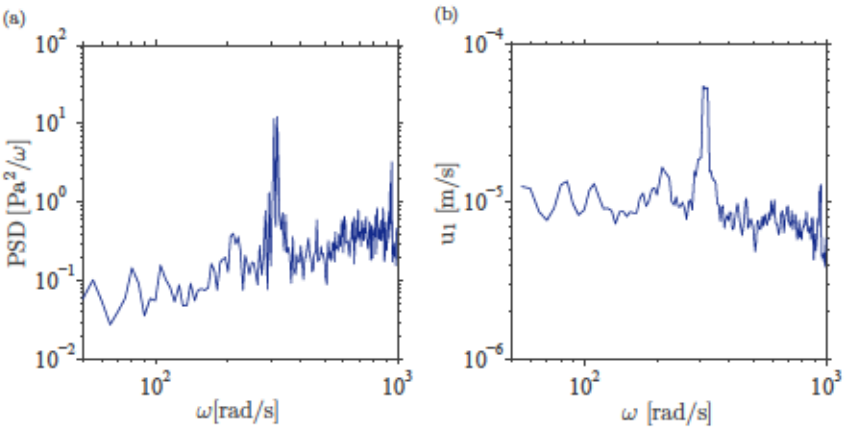

Figure 2.29: Natural noise in the experimental facility described in Chapter 3, when a jet with $\nu = 50$ cSt, $D_i = 4$ mm and $Q = 0.2$ ml/s is established. (a) PSD of the measured pressure $p_{eff}(t)$ in the upstream chamber. The amplitude of pressure fluctuations $p_1(\omega)$ (not shown) is given by the square root of the area under the PSD for frequency ranges $d\omega = 5$ rad/s. (b) Amplitude of fluctuations of the mean axial speed at the injector exit u_1, obtained by replacing the values of $p_1(\omega)$ in equation (3.4).

2.5 Conclusions

In this chapter we have experimentally and numerically characterized the natural break-up of Newtonian liquid jets stretched by gravity.

We carried out an experimental campaign in which the governing parameters of the flow were varied, namely the flow rate, injector size and liquid viscosity. In particular, we focused on the strongly stretched jets obtained by injecting flow rates close to the jetting–dripping transition and using large nozzles. Regarding the break-up length, we observed that it increases when the flow rate or viscosity increase, in agreement with the behavior reported for slender jets by Nonnenmacher & Piesche (2004) and Javadi *et al.* (2013). Meanwhile, when the fluid issues from larger injectors we observed a slight decrease of the pinching length, a behavior which is in qualitative agreement with the numerical findings by Amini *et al.* (2013). We also measured a parameter which had not been previously reported in strongly stretched jets, namely the frequency of the most amplified disturbances, which increases with the flow rate. In all cases, the measured variables exhibit an irregular temporal evolution and a large dispersion around the mean value due to the noisy triggering of the instability process.

Regarding the stability analysis, the small amplitude of initial disturbances justifies the use of a linear approach. The fluid field was accordingly decomposed into a steady basic flow plus small disturbances, and described using the leading order one-dimensional conservation equations due to García & Castellanos (1994) and Eggers & Dupont (1994). First, we adopted the classical quasi-parallel assumptions and implemented a local analysis by deriving a local dispersion relation which accounts for the stretching retaining the non-parallel terms. We discussed the limitations of the classical quasi-parallel approach, and subsequently proposed the formulation of a non-modal stability analysis.

In contrast with eigenvalue analysis, the linear global frequency response analysis (GFRA) makes no hypothesis on the spatial shape of perturbations, except for assuming that they are of small amplitude. Hence, the frequency response

of the governing equations to harmonic inputs at the outlet of the injector is formulated for the first time, with the aim at describing the main features of the break-up of globally stable jets. The generality, simplicity and computational efficiency of this analysis must be highlighted. This procedure admits a wide range of inputs, including perturbations in the radius and/or speed of the jet at any axial coordinate with variable spatial distribution (localized, Gaussian, etc). Moreover, provided an adequate model of the governing equations is available, a GFRA could be implemented for stretched jets generated in different contexts, such as electrosprays or co-flows.

From the physical point of view, our main finding is that the meniscus region near the injector outlet, where the jet experiences the strongest axial stretching, selectively filters the outlet disturbances, providing an optimal frequency responsible for the break-up of the jet downstream. The growth of disturbances is delayed due to a spatial counterpart of the kinematic stabilizing mechanism first described by Tomotika (1936).

The fairly good quantitative agreement between the predicted break-up lengths and those obtained experimentally, with the initial amplitude as the *only* free parameter, gives support to our theory. However, the predicted break-up frequencies present a strong disagreement with those experimentally measured. The fact that the GFRA is unable to capture the nonlinear behavior in the break-up region may not be the main cause of this disagreement, since during most of the process the amplitude of disturbances remains small. It is possible that the interaction of perturbations of different frequencies, which is not taken into account in our analysis, gives rise to differences between predictions and observations. In the case of a slowly varying flow, the maximum growth rate remains confined to a narrow band of frequencies, which subsequently present an amplitude that is significantly larger than that of other disturbances. However, in a non-parallel jet the optimal frequency varies with the axial coordinate, and it is likely that break-up occurs due to a perturbation which is not purely harmonic but exhibits energy within a band of frequencies. Indeed, the sensitivity of the intact length to the amplitude and frequency of disturbances, numeri-

cally assessed herein through the $L_b(\omega, \epsilon)$ contour maps, suggests that the more pronounced frequency selection occurs for longer jets, which present a more extensive parallel region downstream. We also suspect that discrepancies in the predicted frequencies could arise from an uneven energy spectrum of the noise coming from the experimental facility. The work in the next chapter includes forced experiments in order to eliminate these uncertainties concerning the energy distribution of perturbations triggering the response.

References

AMINI, G., IHME, M. & DOLATABADI, A. 2013 Liquid jet instability under gravity effects. *Phys. Rev. E* 87 (053017).

BAGHERI, S., HENNINGSON, D. S., HOEPFFNER, J. & SCHMID, P. J. 2009 Input-output analysis and control design applied to a linear model of spatially developing flows. *Appl. Mech. Rev.* 62 (020803).

CHOMAZ, J. M. 2005 Global instabilities in spatially developing flows: Non-normality and nonlinearity. *Ann. Rev. Fluid Mech.* 37, 357–392.

CHOMAZ, J. M., HUERRE, P. & REDEKOPP, L. G. 1988 Bifurcations to local and global modes in spatially developing flows. *Pys. Rev. Lett.* 60 (1), 25–28.

CLANET, C. & LASHERAS, J. C. 1999 Transition from dripping to jetting. *J. Fluid Mech.* 383, 307–326.

CONSOLI-LIZZI, P. 2012 Análisis de estabilidad espacial de chorros líquidos sometidos a la influencia de la gravedad. Master's thesis, Universidad Carlos III de Madrid.

EGGERS, J. & DUPONT, T.F. 1994 Drop formation in a one-dimensional approximation of the navier-stokes equation. *J. Fluid Mech.* 262, 205–222.

EGGERS, J. & VILLERMAUX, E. 2008 Physics of liquid jets. *Rep. Prog. Phys.* 71, 036601.

FRANKEL, I & WEIHS, D. 1985 Stability of a capillary jet with linearly increasing axial velocity (with application to shaped charges). *J. Fluid Mech.* 155, 289–307.

GARCÍA, F.J. & CASTELLANOS, A. 1994 One-dimensional models for slender axisymmetric viscous liquid jets. *Phys. Fluids* 6 (8), 2676–2689.

GUERRERO, J., GONZÁLEZ, H. & GARCÍA, F.J. 2012 Spatial modes of capillary jets with application to surface stimulation. *J. Fluid Mech.* 702, 354–377.

JAVADI, A., EGGERS, J., BONN, D., HABIBI, M. & RIBE, N. M. 2013 Delayed capillary break-up of falling viscous jets. *Phys. Rev. Lett.* 110 (144501).

KALAAJI, A., LOPEZ, B., ATTANÉ, P. & SOUCEMARIANADIN, A. 2003 Breakup length of forced liquid jets. *Phys. Fluids* 15 (9).

LEE, C. H. 1974 Drop formation in a liquid jet. *IBM J. Res. Develop.* 18 (4).

MARMOTTANT, P. & VILLERMAUX, E. 2004 Fragmentation of stretched liquid ligaments. *Phys. Fluids* 16, 2732.

MIKAMI, T., COX, R. G. & MASON, S.G. 1975 Break-up of extending liquid threads. *Int. J. Multiphase Flow* 2, 113–138.

NONNENMACHER, S. & PIESCHE, M. 2004 Stability behavior of liquid jets under gravity. *Chem. Eng. Technol.* 27 (5), 529–536.

REDDY, S. C., SCHMID, P. J. & HENNINGSON, D. S. 1993 Pseudospectra of the orr-sommerfield operator. *SIAM J. Appl. Math.* 53, 15–47.

RUBIO-RUBIO, M. 2016 Stretching liquid flows: jets, drops and liquid bridges. PhD thesis, Universidad Carlos III de Madrid.

RUBIO-RUBIO, M., SEVILLA, A. & GORDILLO, J.M. 2013 On the thinnest steady threads obtained by gravitational stretching of capillary jets. *J. Fluid Mech.* 729, 471–483.

RUTLAND, D. F. & JAMESON, G. J. 1971 A non-linear effect in the capillary instability of liquid jets. *J. Fluid Mech.* 46 (2), 267–271.

SCHMID, P.J. 2007 Nonmodal stability theory. *Annu. Rev. Fluid Mech.* 39, 129–162.

SENCHENKO, S. & BOHR, T. 2005 Shape and stability of a viscous thread. *Phys. Rev. E* 71 (056301).

TOMOTIKA, S. 1936 Breaking up of a drop of viscous liquid immersed in another viscous fluid which is extending at a uniform rate. *Proc. Roy. Soc.* 153, 302–318.

TREFETHEN, L. N., TREFETHEN, A., REDDY, S. C. & DRISCOLL, T. 1993 Hydrodinamic stability with eigenvalues. *Science* 261, 578–584.

WEIDEMAN, J. A. C. & REDDY, S. C. 2000 A matlab differentiation matrix suite. *ACM Transactions on Mathematical Software* 26 (4).

CHAPTER

THREE

Controlled break-up of gravitationally stretched jets

Contents

3.1 Introduction

Once the natural break-up of gravitationally stretched liquid jets has been studied in Chapter 2, here we focus on their controlled break-up.

The experimental campaign presented in this chapter overcomes the uncertainty regarding the initial energy distribution in unforced experiments, where the theoretically assumed white noise was not guaranteed in practice. In contrast, the controlled harmonic forcing of the jet allows us to unambiguously characterize the input disturbances while exploring the receptivity of the jet.

Regarding the theoretical treatment of the convective instability, a global linear analysis captures the damping of the amplitude of perturbations occuring in the meniscus region, but is not able to describe the final stages before break-up. Moreover, since in the forced experiments which we report we introduce speed fluctuations of $\mathcal{O}(0.1)$, here we propose a one-dimensional nonlinear analysis which is able to describe the stability of large amplitude perturbations.

Measurements from experiments on liquid jets where the input disturbances are unambiguously characterized give robust material against which theoretical predictions can be contrasted. Moreover, the control over the character of the imposed disturbances is of large importance in applied technology, since it determines the wavelength and growth rate of disturbances (Chauhan *et al.*, 2002), and therefore the drop size. As a result, plenty of forcing techniques have been applied to control the break-up of jets. Vibration of the feeding chamber was used in the very early experimental work of Savart (1833). Acoustic waves were used in the work of Donnelly & Glaberson (1966) to experimentally measure the dispersion relation, while Rutland & Jameson (1971) stimulated water–glicerine jets either using a loudspeaker clamped to a steel frame or, with more viscous fluids, a pin fastened to the centre of the speaker contacting the jet. Surface deformation can be induced by electrohydrodynamic stimulation, by applying voltage to a thin electrode and inducing electric pressure on the liquid (García *et al.*, 2014), or by thermocapillary stimulation, where a resistive heater modulates the jet to trigger the Marangoni instability (Hanchak & Furlani, 2010). Pressure fluctuations in the feeding chamber can be introduced using a moving piston when the desired amplitude is large (Meier *et al.*, 1992), or resoting to the oscillations of a piezoelectric transducer when the relative fluctuations are smaller (Chaudhary & Maxworthy, 1980*a*; Chauhan *et al.*, 2002; Cheong & Howes, 2004; Dong *et al.*, 2006). In the case of imposing pressure modulations, González & García (2009) provide a procedure to relate their amplitude to fluctuations of the speed of the jet.

Regarding the character of the imposed disturbances, most previous works deal

with monochromatic harmonic stimulation. However, other possibilities are useful, such as the application of signals consisting of pulses (Hanchak & Furlani, 2010), a fundamental and one harmonic component to prevent satellite formation (Chaudhary & Maxworthy, 1980*a*), or single and double-peak waveforms for drop on demand (DOD) technology (Dong *et al.*, 2006). The variety of stimulation techniques provides different boundary conditions, namely radius modulation, velocity modulation or jet vibration, their equivalences being discussed in the recent work of Moallemi & Mehravan (2016).

These experimental techniques have been used to gather experimental information on the growth rate of disturbances (Donnelly & Glaberson, 1966; Chauhan *et al.*, 2002; González & García, 2009), the break-up length (Meier *et al.*, 1992; García *et al.*, 2014), to characterize nonlinear behavior and drop formation (Rutland & Jameson, 1971; Chaudhary & Maxworthy, 1980*a*,*b*; Mansour & Lundgren, 1990), to explore DOD operation conditions (Bogy & Talke, 1984; Dong *et al.*, 2006), to examine the optimal frequency (Cheong & Howes, 2004), among other applications.

In this chapter we present experiments where fluctuations of the axial speed of the jet at the injector are induced while the contact line remained pinned. With this aim, harmonic fluctuations of controlled frequency and amplitude were mechanically imposed to the pressure of the feeding system. We report the effect of the stimulation parameters on the intact length of strongly stretched jets for different flow configurations, observing a transition from irregular to periodic break-up, and finally revealing the existence of an oscillatory dripping regime when the amplitude of disturbances is large enough.

Although the physical mechanisms governing the nonlinear evolution of disturbances are the same as in the linearized description, the nonlinear theory provides additional quantitative results (Lin & Reitz, 1998). An early nonlinear analysis of the stability of jets was carried out by Yuen (1968), who examined the effect of harmonic modulations on the radius of an inviscid jet, addressing perturbations in the form of an infinite series and developing the solution up to

third order in ϵ. He predicted the existence of satellite drops for all wavenumbers, a theory which was experimentally corroborated by Rutland & Jameson (1971), who observed the occurrence of swellings between the crests of primary disturbances. The results obtained from perturbation expansions were reviewed by Bogy (1979). Chaudhary & Redekopp (1980) also proposed a third order analysis in their weakly nonlinear stability analysis, concluding that near the cut-off wavenumber of the dispersion relation the growth was linear instead of exponential, and reporting the type of initial perturbation which would supress the formation of satellites. Once more, predictions were in agreement with experiments by Chaudhary & Maxworthy (1980*a*). Moreover, besides weakly nonlinear theories where perturbation theory is carried to higher order, it is possible to simulate the free surface flow to describe the evolution of large amplitude disturbances. Besides using computationally intensive CFD analysis of the Navier–Stokes equations (Pan & Suga, 2006), it is also possible to integrate the fully nonlinear one-dimensional conservation equations. For instance, Chuech & Yan (2006) solved a one-dimensional system of equations in a matrix form using a total variation diminishment upwind scheme with fux vector splitting, predicting longer break-up lengths and slower growth rates than linear models. Furlani & Hanchak (2010) also integrated a one-dimensional slender jet model, using the method of lines to predict the nonlinear deformation and break-up when applying thermal modulation in the ink-jet printing technique. In this chapter we adopt a numerical technique similar to that implemented by Furlani & Hanchak (2010) to describe the nonlinear behavior and to predict the intact length of forced stretched jets. We address the evolution of the perturbed fluid field by implementing the method of lines to integrate the one-dimensional equations (1.9)-(1.11). Then, we validate this model by comparing its results to our experimental observations, and examine the agreement of the predictions for the initial growth of perturbations with those of the linear global frequency response analysis presented in Chapter 2.

3.2 Experimental and numerical techniques

3.2.1 Experimental techniques

The aim of the experimental campaign was to perform a parametrical study to characterize the dependence of the jet length on the amplitude and frequency of the velocity stimulation. The effects of liquid viscosity, flow rate and injector diameter were also investigated.

We initially intended to report the volume distribution of the detached drops and ligaments which evolve into drops due to the practical interest on this subject. However, when carrying out the experiments we found that due to the long wavelength of disturbances, a different video acquisition configuration would have been required to record the pinching and evolution of the ligament and drop of a whole detached wavelength.

3.2.1.1 Experimental set-up

Experiments were carried out in a facility sketched in Figure 3.1 which is based on a similar set-up described in García *et al.* (2014). The jet under study and the acquisition camera were located on a leveled vibration isolation table and inside a PMMA chamber, in order to minimize vibrations and external air flows. The liquid flow rate was controlled with a Harvard Apparatus PHD Ultra Syringe Pump (A) and fed through a 4 mm Legris tube. In the stimulation chamber (B) a piston actuated by a TIRA Vibration Test System TV 51120 provided a harmonic pressure stimulation of controlled amplitude and frequency, which is transmitted to the main flow through a 12 mm Legris tube. The large diameter and short length of the latter tube was selected to reduce the inertia of the fluid inside the tube, which is a limiting factor to the amplitude of the stimulation, since overcoming this inertia demands force from the actuator. Both impulse and stimulation lines join just above a pressure-measuring chamber (C), in whose side a Honeywell 40PC Pressure Sensor (E) is placed close

to the bottom. The chamber is 10 cm in height to minimize inlet effects, and with a diameter of 5 cm, much larger than that of the injector, to guarantee a negligible dynamic pressure. All tubes and chambers were transparent to allow for visual detection of undesired bubbles. A coupling in the pressure-measuring chamber's base leads the perturbed flow to the vertical injector (D), whose end is trimmed to ensure that the contact line remained pinned to its inner diameter. The stimulated jet issues from the stainless steel tube, stretches under the gravitational acceleration and breaks-up, and the fluid is collected in a vessel. Images of the region of the jet close to the pinching point were acquired at 1 kHz during five seconds with a high-speed camera (F). A computer (G) recorded the images and monitored the amplitude of the perturbed pressure provided by the sensor, whose response time was 1 ms. The temperature was also registered in each experiment.

The acquired images were analized with a home-made MATLAB® script which is able to distinguish different masses of fluid, namely drops, ligaments and filaments. The main part of the jet that remains attached to the nozzle is the filament, whose length $L(t)$ is a function of time. The pinching length or break-up length L_b is the axial location where a mass of fluid separates from the ligament, and corresponds to local minimum values of $L(t)$. When a mass first breaks-up, it can appear as a drop whose aspect ratio is close to unity, or as a ligament with an undulating and rapidly changing shape which later turns into one or more spherical drops. Our code was developed to measure the temporal evolution of the length and the radius of the jet at selected axial positions.

3.2.1.2 Materials

Jets were generated using Sigma-Aldrich silicone oils injected through stainless steel tubes from Tubca. The working liquids and injector diameters were selected among those used in the study of natural break-up presented in chapter 2, aiming to asess the influence of the viscosity and of the size of the injector,

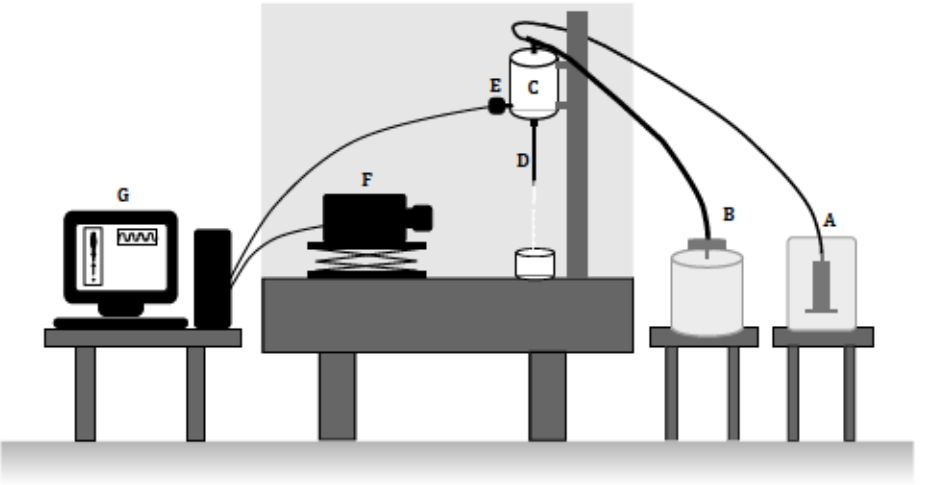

Figure 3.1: Sketch of the forced break-up experimental facility.

and their main properties are listed in Tables 3.1 and 3.2. To compute head losses, it should be stated that the coupling of the injectors to the pressure-measuring chamber is 12 mm long and presents an inner diameter $D_a = 2$ mm.

ν [mm^2 s^{-1}]	ρ [kg m^{-3}]	σ [mN m^{-1}]
50	960	20.8
100	965	20.9

Table 3.1: Properties at 25°C of the silicon oils used in the stimulation experiments.

D_o [mm]	D_t [mm]	l_t [mm]
4.5	4	225
6	5.5	225

Table 3.2: Dimensions of the injectors used in the stimulation experiments.

3.2.1.3 Characterization of the stimulation

To fully characterize the evolution of disturbances and the jet break-up, the initial amplitude and frequency of the imposed disturbances must be known. Regarding the frequency, we have experimentally checked that, provided the amplitude of the stimulation is large enough, the response of the flow presents the same frequency ω as the input of the vibration system by measuring the temporal evolution of the radius of the jet at several axial positions and computing the energy spectrum. Regarding the amplitude of disturbances at the exit of the injector, it has been checked that the contact line remains pinned while the velocity is harmonically modulated, resulting in a purely impulsive boundary condition. Since in our experiments the pressure amplitude is monitored at an upstream chamber, we resort to the model developed by García *et al.* (2014) to relate the hydrodynamics of the chamber with that of the jet at the tube exit.

In our facility, the elements of the fluid line under study are the pressure-measuring chamber, a short coupling, the injector and the jet. Since $ReSt \sim \mathcal{O}(1)$ in our experiments, where $Re = UD_i/\nu$ is the Reynolds number and $St = R\omega/(2\pi U)$ is the Strouhal number, unsteady inertial effects and viscous losses must be taken into account when describing the flow. As explained by García *et al.* (2014), an extended Bernoulli's equation can be deduced to include both effects along a streamline $\Gamma(t)$ connecting a point inside the chamber (labeled with subscript c) and the issuing jet at the exit (subscript j),

$$(p_j - p_c) + \frac{1}{2}\rho\left(v_j^2 - v_c^2\right) + \rho g\left(z_j - z_c\right) + \rho \int_\Gamma \mathrm{d}\mathbf{r} \cdot \frac{\partial \mathbf{v}}{\partial t} + \Delta P_{visc} = 0 \quad (3.1)$$

where p and $\mathbf{v}$ are the pressure and velocity with modulus v as functions of position $\mathbf{r}$ and time t, and z is the vertical coordinate. Further hipotheses are made:

- The kinetic energy at the chamber $1/2\rho v_c^2$ is negligible compared to that of the jet $1/2\rho v_i^2$ due to the difference in cross-sectional areas.
- The unsteady inertial term is evaluated inside the injector of length l_i,

taking into account the harmonic disturbance

$$\rho \int_{\Gamma} d\mathbf{r} \cdot \frac{\partial \mathbf{v}}{\partial t} = \rho l_t \frac{dv_t}{dt} = \rho v_t l_t i\omega \tag{3.2}$$

where the velocity in the tube is the same as the initial speed of the jet.

- The viscous losses include primary losses inside the coupling (length l_a = 12 mm and diameter $D_a = 2$ mm) and injector (l_t, D_t) for a laminar flow friction factor $f = 64/Re$, and taking into account losses due to abrupt changes in geometry,

$$\Delta P_{visc} = 32\nu\rho \left(\frac{l_a}{D_a^2} v_a + \frac{l_t}{D_t^2} v_t \right) + \frac{\rho}{2} \left(K_a v_a^2 + K_t v_t^2 \right) \tag{3.3}$$

where $K_a = 0.5$ is the loss coefficient for fluid entering the coupling from the pressure-measuring chamber, and K_t accounts for losses in the abrupt expansion between the coupling and the injector, taking the value K_t = 0.56 for the $D_t = 4$ mm tube and $K_t = 0.76$ for $D_t = 5.5$ mm (White, 2011).

A thorough explanation of a similar problem is found in García *et al.* (2014), defining an effective pressure inside the chamber $p_{eff}(t) = p_0 + p_1 \cos(\omega t)$, which is measured with the pressure sensor. The amplitude of the perturbed speed with respect to that of the steady basic flow at the exit of the injector, $\epsilon \equiv u_1(0)/u_0(0)$, is determined in terms of the amplitude of the perturbed effective pressure p_1 in each experiment as

$$\epsilon = \frac{p_1}{\rho U \left\{ l_t \omega + \left[32 \frac{\nu}{D_t^2} \left(\frac{l_a}{\alpha^2} + l_t \right) + U \left(\frac{K_a}{\alpha^2} + K_t - 1 \right) \right] \right\}} \tag{3.4}$$

where $\alpha = D_a^2/D_t^2$ relates the diameter of the contracted coupling section with that of the injector, and the speed of the steady basic flow at the injector is calculated according to the flow rate given by the syringe pump Q as $U \equiv u_0(0) = 4Q/(\pi D_t^2)$.

When substituting the experimentally measured pressure fluctuations p_1 into equation 3.4, the relative amplitudes of the perturbed speed for which the jet's response differs from natural break-up are $\epsilon > 10\%$.

Harmonic fluctuations with frequencies between 8 and 1000 Hz can be imposed with our stimulation facility. However, the amplitude of the stimulation presents an important limitation. If Bernoulli's extended equation is applied to a streamline connecting the stimulation chamber and the exit of the injector, it can be deduced that the force provided by the actuator must overcome both head losses and inertia along the line. Although these factors were minimized by mounting the facility using pipings of shorter length and larger area, greater increments of the pressure at the stimulating chamber are required to reach a given value of the velocity amplitude at higher frequencies. As a result, the span of ϵ which can be swept in our facility is narrower for higher frequencies. Moreover, in the case of more viscous jets, the maximum attainable frequencies are lower.

On the other hand, harmonic perturbations with ϵ close to unity can be imposed for values of ω up to 300 rad/s. Beyond this point, oscillations of the meniscus induce significant fluctuations of the capillary pressure at the exit of the injector. Since $We < 1$ for the flow configurations under study, these are comparable to the dynamic pressure. As a result, the pressure fluctuations acquired with the sensor are no longer sinusoidal. Moreover, changes in the curvature of the meniscus damp the amplitude of the flow rate, preventing reverse flow from taking place in spite of largely incrementing the force of the actuator.

3.2.2 Numerical method

Linear approaches admit only disturbances of small amplitude and are unable to capture the downstream region immediately before break-up. A nonlinear model overcomes the limitations regarding the amplitude of disturbances, serving as a tool to validate the previously developed model and to explore the validity of the linear used description, as well as allowing to unambiguously impose the forcing amplitude. In our nonlinear stability analysis, the evolution of the fluid field is obtained by integrating the fully nonlinear leading-order one-dimensional mass and momentum conservation equations, a technique which

has also been implemented in the work of Furlani & Hanchak (2010).

3.2.2.1 Nonlinear Analysis

In our model, the axial velocity field, $u(z,t)$, and the radius of the jet, $h(z,t)$, are described equations (1.9)-(1.11). These equations were discretized and solved resorting to the method of lines, which consists of transfroming the PDEs into a system of ODEs (Schiesser, 1991; Furlani & Hanchak, 2010), where the spatial derivatives are written as finite differences.

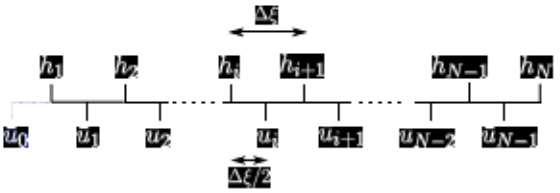

Figure 3.2: Staggered computational grid, including the virtual node $\bar{u}_0$.

The differential equations governing the flow can be conveniently solved using a uniform grid in computational space. We define a staggered computational grid along the jet, where u and h are evaluated on different sets of nodes, $\xi : [0,1]$ and $\bar{\xi} : [\Delta\xi, 1-\Delta\xi]$ respectively. As displayed on Figure 3.2, h is calculated at N nodes, while u is evaluated at $N-1$ nodes which are displaced by an amount $\Delta\xi/2$ from the former. To impose the speed at the injector, the value $\bar{u}_0$ is set at an additional virtual node.

Note that in this section we use the subindexes in the discretized flow field, h_i and $\bar{u}_i$, to indicate the corresponding grid node. In contrast, in the previous chapter, we used subindexes to distinguish the steady base flow and perturbations.

The meniscus zone of the jet requires higher grid resolution ir order to capture the effects of the strong stretching on the evolution of disturbances. Therefore, a non-uniform physical grid with points clustered near the injector is used, with

a mapping defined by

$$\xi = 1 - \frac{\ln\left(\frac{\beta+1-x/L_d}{\beta-1+x/L_d}\right)}{\ln\left(\frac{\beta+1}{\beta-1}\right)}, \tag{3.5}$$

for constant $\beta > 1$ (Farrashkhalvat & Miles, 2003). Its value is selected to provide a similar density of grid points per wavelength both upstream and downstream, as can be appreciated in Figure 3.3. The clustering around the injector is evident by inspecting the derivative $\partial\xi/\partial x$, which is maximum at $x = 0$, with higher grid density as the parameter β approaches the limiting value 1. Since the length of the jet is a function of time, we do not simulate the whole jet down to its tip in order to simplify the numerical formulation of the problem. Instead, the physical grid under study $x \in [0, L_d]$ remains fixed for all time. Future work should extend our model to a fluid domain evolving in time, $L_d(t)$, that also includes the jet tip and the break-up events (Rivero-Rodríguez, 2016).

Once the grid nodes are defined, second-order central differencing is used in the discretization of spatial derivatives, except for a first-order upwind scheme used for the advection terms. The original equations (1.9)-(1.11), expressed in terms of cylindrical coordinates, have to be transformed to the computational coordinates using the chain rule (Farrashkhalvat & Miles, 2003), $\frac{\mathrm{d}}{\mathrm{d}x} = \frac{\partial\xi}{\partial x}\frac{\partial}{\partial\xi}$. The conservation equations (1.9)-(1.11) become

$$\left.\frac{\mathrm{d}\bar{u}}{\mathrm{d}t}\right|_i = -\bar{u}_i \left.\frac{\mathrm{d}\bar{\xi}}{\mathrm{d}x}\right|_i \frac{\bar{u}_i - \bar{u}_{i-1}}{\Delta\xi} - \frac{\sigma}{\rho}\left.\frac{\mathrm{d}\bar{\xi}}{\mathrm{d}x}\right|_i \frac{C_i - C_{i-1}}{\Delta\xi} + g + 3\nu \frac{1}{h_i^2}\frac{1}{\Delta\xi}\left.\frac{\mathrm{d}\bar{\xi}}{\mathrm{d}x}\right|_i \left[h_{i+1}^2 \left.\frac{\mathrm{d}\bar{\xi}}{\mathrm{d}x}\right|_{i+1} \frac{\bar{u}_{i+1} - \bar{u}_i}{\Delta\xi} - h_i^2 \left.\frac{\mathrm{d}\bar{\xi}}{\mathrm{d}x}\right|_i \frac{\bar{u}_i - \bar{u}_{i-1}}{\Delta\xi}\right] \tag{3.6}$$

and

$$\left.\frac{\mathrm{d}h}{\mathrm{d}t}\right|_i = -\frac{1}{2}\left.\frac{\mathrm{d}\xi}{\mathrm{d}x}\right|_i \left[(\bar{u}_i + \bar{u}_{i-1})\frac{h_i - h_{i-1}}{\Delta\xi} + h_i \frac{\bar{u}_i - \bar{u}_{i-1}}{\Delta\xi}\right], \tag{3.7}$$

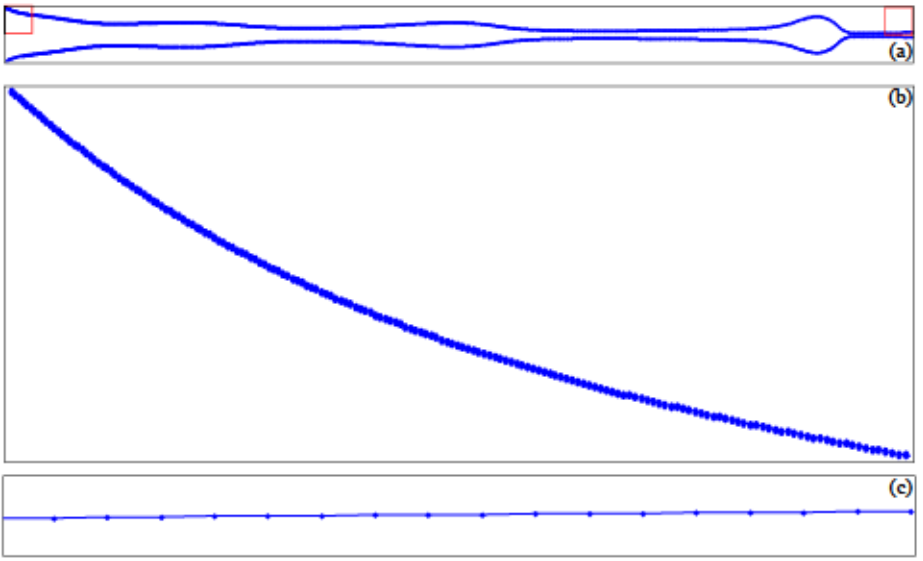

Figure 3.3: ξ nodes distribution on a jet where harmonic stimulation of $\omega = 200$ rad/s and $\epsilon = 0.35$ is applied (a), attained setting $\beta = 1.5$. The domain length is $L_d = 33$ R, and the number of nodes is $N = 1150$. Insets (b) and (c) display in detail the node distribution of upstream and downstream regions inside the red boxes in (a), which are one radius in length.

where overbars are used for magnitudes evaluated at the $\bar{\xi}$ nodes. The curvature $\mathcal{C}$ is computed on the ξ nodes according to

$$\mathcal{C}_i = \frac{1}{h_i} \frac{1}{\left[1 + \left(\frac{\partial h}{\partial x}\Big|_i\right)^2\right]^{1/2}} - \left.\frac{\partial^2 h}{\partial x^2}\right|_i \frac{1}{\left[1 + \left(\frac{\partial h}{\partial x}\Big|_i\right)^2\right]^{3/2}}, \tag{3.8}$$

where the spatial derivatives of h, due to the mapping, are

$$\left.\frac{\partial h}{\partial x}\right|_i = \left.\frac{\mathrm{d}\xi}{\mathrm{d}x}\right|_i \frac{h_{i+1} - h_{i-1}}{2\Delta\xi}, \tag{3.9}$$

and

$$\left.\frac{\partial^2 h}{\partial x^2}\right|_i = \left.\frac{\mathrm{d}^2\xi}{\mathrm{d}x^2}\right|_i \frac{h_{i+1} - h_{i-1}}{2\Delta\xi} + \left(\left.\frac{\mathrm{d}\xi}{\mathrm{d}x}\right|_i\right)^2 \frac{h_{i+1} - 2h_i + h_{i-1}}{\Delta\xi^2}. \tag{3.10}$$

These equations are non-dimensionalized with the inner radius of the injector R, the mean outlet velocity of the basic flow U, and the timescale R/U, and

supplemented with appropriate boundary conditions: at the injector, $\xi = 0$, the radius of the injector remains pinned, $\dot{h}_1 = 0$, where dots indicate time derivatives. To study the stimulation, the outlet velocity is prescribed as $u(0,t) = U[1 + \epsilon \sin(\omega t)]$. However, since u is defined at the $\bar{\xi}$ nodes, a virtual node where the value of the speed is $\bar{u}_0 = 2u(0) - \bar{u}_1$ is used for the discretization of derivatives. At the downstream end of the domain, a Neumann boundary condition is imposed, $u'(L_d) = 0$, so that the discretized derivative in the viscous term $\frac{\bar{u}_{i+1} - \bar{u}_i}{\Delta\xi}$ is null.

With this approach, the partial time derivatives of the variables become time derivatives of each nodal value. The resulting system of ordinary differential equations is integrated using the ode23t solver provided by MATLAB®, suitable for moderately stiff problems and without numerical damping of the solution.

3.3 Results

3.3.1 Experimental results

The experimental campaign focuses on gathering information on the response of the jet to different stimulation frequencies and amplitudes of the liquid velocity at the injector outlet. The explored range of both parameters covers break-up modes different from those occurring in the natural case. The stimulating frequency ω was varied between 50 and 600 rad/s (8-96 Hz), and we report experiments where the relative velocity amplitudes ϵ are high, starting at 10%. Although not reported, our experimental facility has allowed us to explore the response of the jet to values of ϵ below 10 % for the whole range of frequencies. We have not included these results since we have not observed any changes in the stability when compared to the natural case: their corresponding break-up remains irregular and we have been unable to detect the stimulating frequency on the interface displacements. In contrast, Meier *et al.* (1992) have reported

the kinematic break-up of water jets stimulated with $\epsilon = 2.5\%$, but we attribute the lower receptivity found here to the smaller Weber numbers and the higher liquid viscosity. We have also imposed harmonic fluctuations of the velocity up to $\omega = 1000$ rad/s, although in this case the experimental facility limited the maximum amplitude of disturbances to 17 %, for which the jet was not controlled.

As a reference case, we will discuss in detail the receptivity of a jet with $\nu = 50$ cSt issuing from a tube with $D_t = 4$ mm at $Q = 0.2$ ml/s. When the stimulation frequency remains fixed, our observations suggest that natural break-up takes place for ϵ below 10%. The observed behavior does not differ from that described in Chapter 2. When the amplitude is incremented to 15%, the pinching length presents the same values and distribution as the natural case. Break-up remains chaotic, with filaments of diverse length aperiodically detaching, as displayed in Figure 3.4(a). Although the bulge distribution resembles the unforced case, the images show larger mass concentration in the crests corresponding to the stimulating frequency. Indeed, if the temporal evolution of the radius of the jet $h(t)$ at several positions is studied in the frequency domain, its spectrum reveals the presence of energy at the stimulating frequency, not present in the natural case. When ϵ is increased beyond 20%, the pinching length decreases. The experiment in Figure 3.4(b) reveals that the temporal evolution of $L(t)$ is not as irregular as in previous case, and the standard deviation of the pinching length is also reduced. Jets stimulated at frequencies larger than 200 rad/s experience a reduction of their pinching length as ϵ is increased, exhibiting a more pronounced slope for lower frequencies, as will be discussed for Figure 3.8. The fall in the deviation of the pinching length eventually leads to a periodic break-up with only one value of L_b, as shown in Figure 3.4(c). Lower frequencies are more receptive, and for instance this behavior is attained for $\epsilon = 60\%$ when $\omega = 200$ rad/s. As a result, the spectrum of $L(t)$ shows clear peaks at the stimulating frequency and its harmonics. However, we have also observed that for some specific parameter combinations there is a bimodal distribution of

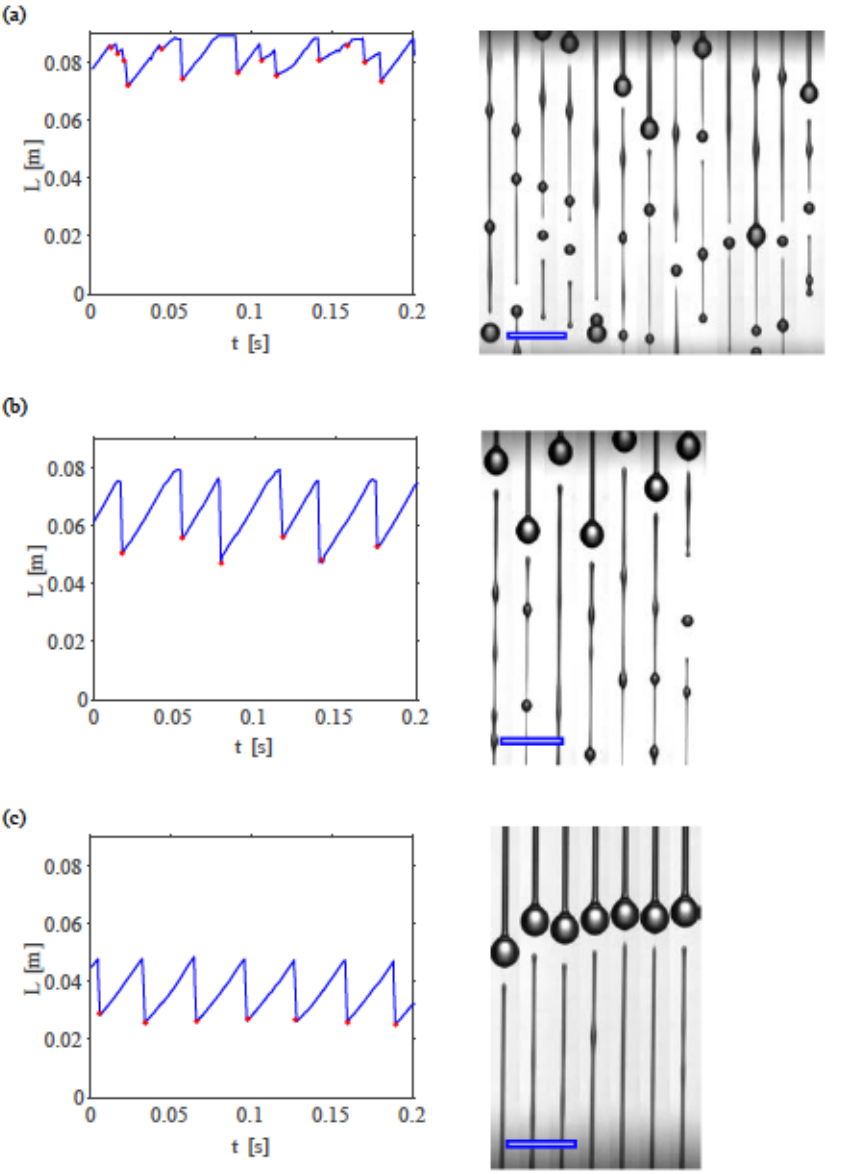

Figure 3.4: Response of the reference jet. Temporal evolution of the jet length $L(t)$ and photographs showing consecutive pinchings marked with dots, for a stimulating frequency $\omega = 200$ rad/s and different perturbation amplitudes, (a) $\epsilon = 0.14$, (b) $\epsilon = 0.31$, and (c) $\epsilon = 0.71$. The scale bar on each set of photographs is 1 cm long.

L_b, a behavior which was seldom observed. The latter occurs when a ligament detaches at the neck formed just downstream of a swell, followed later by the pinching of the bulge, as displayed in Figure 3.5. As a result, satellites and main drops are alternately produced, and the break-up frequency is twice the stimulation one.

In contrast with the behavior explained in the previous paragraph, when the stimulation frequency is below 200 rad/s, the jet undergoes a sudden decrease of the pinching length, and if ϵ is further increased, a dripping regime is established. The possibility of inducing dripping for frequencies above 100 rad/s could not bee explored, since our forcing system limits the maximum values of ϵ that can be attained.

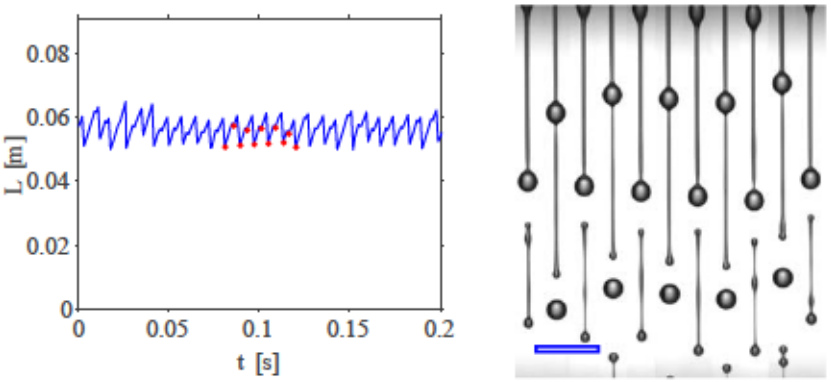

Figure 3.5: Response of a jet with $\nu = 50$ cSt issuing from a tube with $D_i = 6.5$ mm at $Q = 0.2$ ml/s. Temporal evolution of the jet length $L(t)$ and photographs showing consecutive bimodal pinchings marked with dots, for $\epsilon = 0.35$ and $\omega = 400$ rad/s. The scale bar on the set of photographs is 1 cm long.

To assess the sensitivity of the jet to the stimulating frequency, it is useful to consider first a case with a large forcing amplitude of disturbances, $\epsilon = 0.5$, for which the effects of stimulation can be more easily observed. In the particular case with $\omega = 600$ rad/s, the behavior of the jet resembles that observed in a natural break-up. Indeed, as deduced from Figure 3.6(a), the jet exhibits

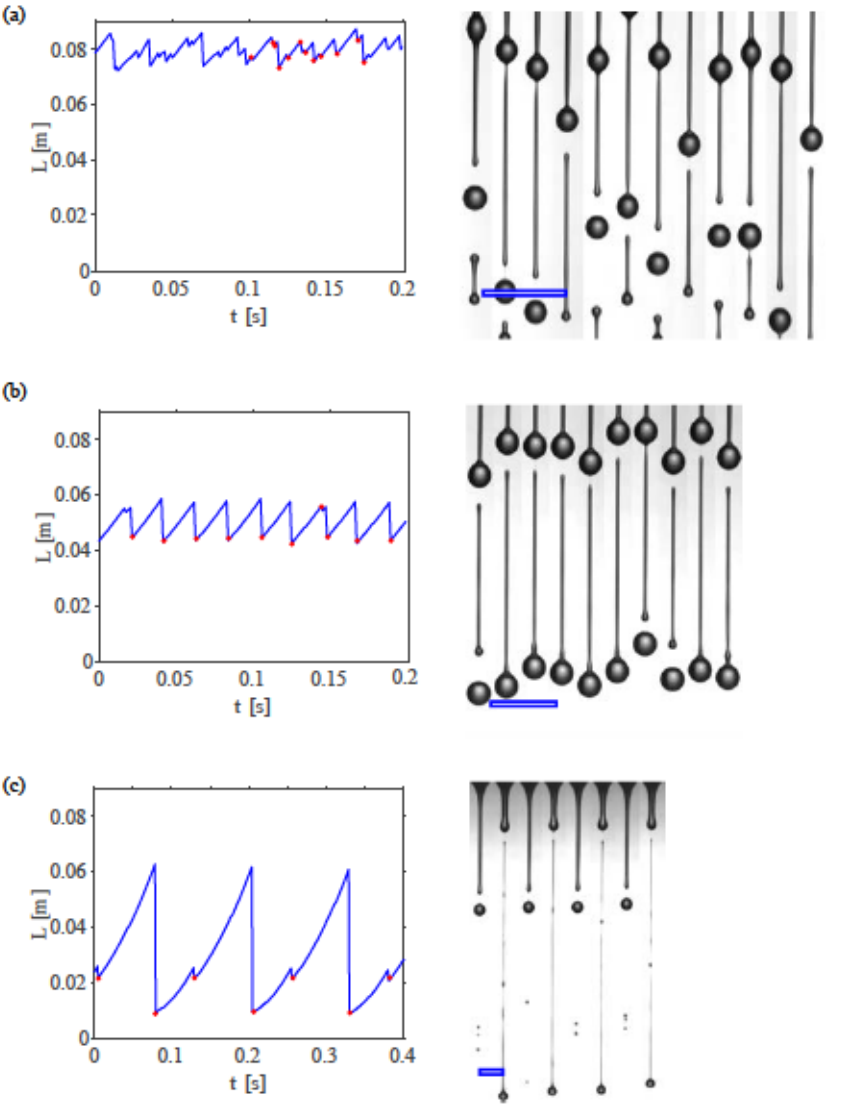

Figure 3.6: Response of the reference jet. Temporal evolution of the jet length $L(t)$ and photographs showing consecutive pinchings marked with dots, for an amplitude of disturbances $\epsilon = 0.5$ and different stimulation frequencies, (a) $\omega = 600$ rad/s, (b) $\omega = 300$ rad/s, and (c) $\omega = 50$ rad/s. The scale bar on each set of photographs is 1 cm long.

a chaotic temporal evolution of the jet length $L(t)$, without a clear preferred frequency, and presents a large standard deviation of the pinching position.
As ω is decreased, the presence of bulges corresponding to the stimulating frequency becomes observable and the pinching length and its variance decrease. For $\omega = 300$ rad/s, Figure 3.6(b) shows that the break-up of the jet becomes more repetitive, and a completely controlled break-up is achieved for $\omega = 200$ rad/s.
If the frequency is decreased to values $\omega \leq 100$ rad/s, the jetting regime experiences a transition to either a simple or complex dripping regime (Subramani *et al.*, 2006) with comparable pinching lengths (Figure 3.6(c)). Note that the Weber number in this particular experiment is $We = 0.02$, which is well above the critical value that delimits the jetting to dripping transition without forcing, $We_c = 0.01$ (Rubio-Rubio *et al.*, 2013). Moreover, in our experiments the flow rate is oscillatory, in contrast with the dripping regimes previously reported in the literature in which the liquid flow rate is kept constant (see for instance Zhang & Basaran, 1995 or Subramani *et al.*, 2006) or impulsively injected in the case of DOD (Bogy & Talke, 1984; Dong *et al.*, 2006).

As previously mentioned, the break-up position L_b and its dispersion depend on the stimulation. In Figure 3.7 we present the three different types of distributions which we have observed. In Figure 3.7(a) where the receptivity of the jet is very low, there exists a most observed value of L_b with a large dispersion which is not completely symmetric. In this case, a Weibull distribution provides a good fit for the experimental data, in agreement with the natural break-up. For higher receptivity, the dispersion of L_b decreases, and we have observed both unimodal and bimodal distributions, which are respectively illustrated in Figures 3.7(b) and 3.7(c). For the sake of presenting our observations, the dispersion in cases (a) and (b) can be quantified by the standard deviation of L_b, but this parameter does not properly describe the bimodal distribution in (c). Therefore, to characterize this different statistical distributions with a unified criterion, we opted to consider the mode and those values of L_b where break-up

takes place with a recurrence of 50% or more of the count of the mode, which are shaded in grey in the figure.

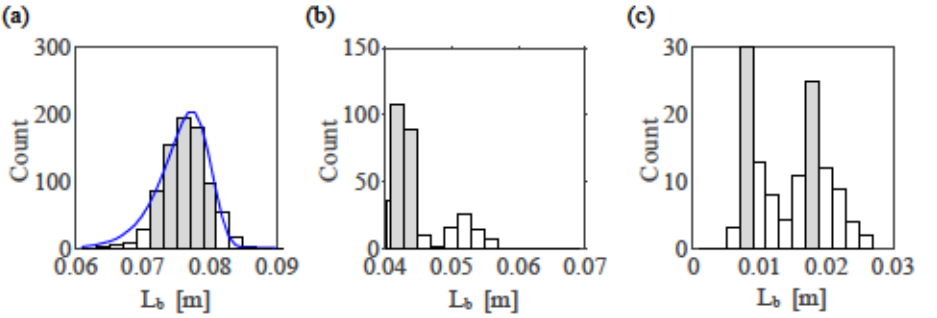

Figure 3.7: Histograms of the pinching length L_b of the reference case for an amplitude of disturbances $\epsilon = 0.5$ and different frequencies. (a) For $\omega = 600$ rad/s a Weibull fit is shown in solid line, (b) for $\omega = 300$ rad/s the distribution is almost unimodal and (c) for $\omega = 50$ rad/s the distribution is bimodal. Elements shaded in grey present an occurrence of 50% or more of the maximum value.

The pinching position L_b provides a good measure to quantify the receptivity of the jet, and is plotted in Figure 3.8 for several values of ω and ϵ. As previously discussed, the mode and values observed 50% of its count are plotted. In the same figure, we have also delimited the zone of dripping regime for $\omega = 50$ and $\omega = 100$ rad/s, which can be identified, following Ambravaneswaran's criterion (Ambravaneswaran *et al.*, 2004), when L_b undergoes a sudden decrease for a small increment of ϵ.

The receptivity of the jet can be clearly visualized by comparing the pinching length under stimulation to that observed in the natural break-up, L_b/L_{bN}, for different amplitudes and frequencies, as displayed in Figure 3.9. The existence of an optimal stimulation frequency, for which the jet length is minimized, can be anticipated.

In order to asses the receptivity of different flow configurations, experiments

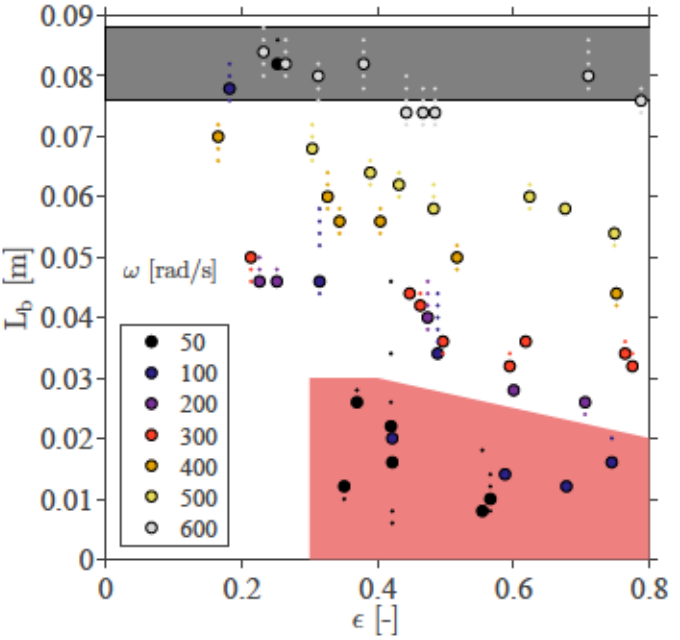

Figure 3.8: Response of the reference jet. Pinching length L_b nondimensionalized in terms of the radius of the injector, as a funtion of the relative amplitude of the perturbed injector speed ϵ for different frequencies ω. Large dots indicate the most observed value of L_b, while smaller ones account for its dispersion, representing those which are observed at least 50% of that count. The grayed zone ranging from 0.076 to 0.088 m states pinching lengths observed in natural break-up. The zone shaded in red indicates the stimulation parameters which trigger dripping.

were also carried out independently varying the flow rate, injector size and viscosity of the fluid.

Let us first consider the case in which the same fluid and injector size are kept constant, $\nu = 50$ cSt and $D_t = 4$ mm, but the flow rate is increased from 0.2 to 0.8 ml/s. As can be observed in Figure 3.10(a), the jet length increases, in agreement with findings for the case of natural break-up, $L_{bN} = 125R$. To facilitate the comparison between the jets at both flow rates, we present the

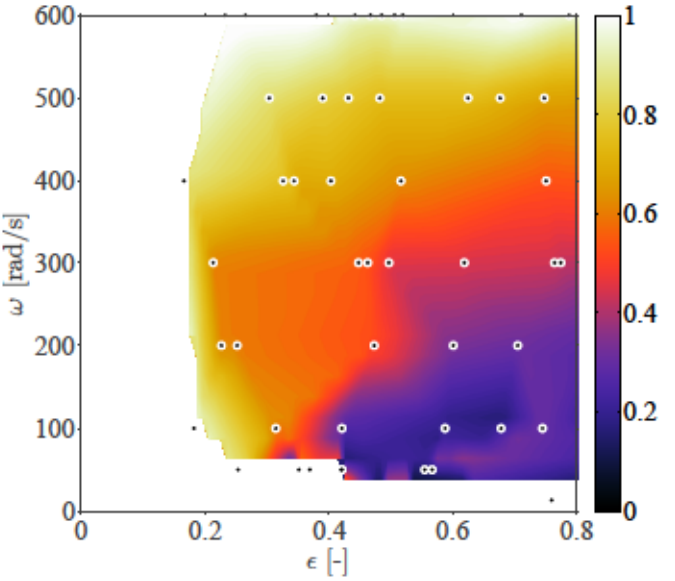

Figure 3.9: Response of the reference jet. Shaded surface plot where colours indicate relative pinching length with respect to its natural counterpart L_b/L_{bN}, for a jet stimulated with amplitudes ϵ at different frequencies ω. Points indicate experimental measurements.

relative pinching length for the case with $Q = 0.8$ ml/s in Figure 3.10(a). When stimulation is applied, the receptivity of the jet qualitatively behaves as in the previous case with $Q = 0.2$ ml/s, increasing for lower values of ω and higher values of ϵ. In contrast, we have not found the oscillatory dripping regime in this case. For the higher flow rate, the periodic break-up is induced inside a larger region of the (ω, ϵ) plane, with very repetitive unimodal break-up behavior at $\omega = 100$ and $\omega = 200$ rad/s, and bimodal pinch-off at $\omega = 75$, 300 and 400 rad/s. These results suggest that increasing the flow rate is desirable for practical purposes. Not only does this jet exhibit a larger region of the (ω,ϵ) plane where its break-up presents less dispersion and lower intact length, but it is also easier to establish due to the fact that its flow rate is well above the jetting-dripping transition.

Let us now consider the case where the working fluid and the flow rate remain

the same while the injector size is increased, namely $\nu = 50$ cSt, $D_i = 4$ mm and $Q = 0.2$ ml/s, the behavior of the jet presents more similarities with the reference case. As in the unforced case, the jet length is not very sensitive to D_i. We have also observed very similar dripping dynamics as in the reference case. The main difference is a slightly higher relative reduction of the pinching length for a given value of ϵ, as can be deduced from Figure 3.10(b).

Finally, we have explored the effect of viscosity by studying the case with $\nu = 100$ cSt, $D_i = 4$ mm and $Q = 0.2$ ml/s. The effect of increasing the viscosity was more pronounced. To start with, the limitations of our stimulating system became evident, since it was not possible to induce significant pressure fluctuations in the stimulation chamber for $\omega > 200$ rad/s. As a result, the effect forcing at high frequencies was not asessed, although the results in Figure 3.10(c) indicate that they would probably have been damped, unaffecting the natural jet length for the range of values of $\epsilon < 0.8$. Figure 3.10(c) clearly illustrates the role of viscosity in damping the disturbances, as the decrease in the normalized pinching length L_b/L_{bN} for any (ω, ϵ) combination is smaller than for any of the previous flow configurations. Furthermore, the selection of an optimum frequency is clear in this case, with the narrowest band of frequencies, close to 75 rad/s, for which the flow is receptive.

3.3.1.1 The oscillatory dripping regime

In our experiments, the dripping regime is induced by harmonic oscillations of the flow rate of jets which are globally stable in the absence of stimulation. In contrast, most of the literature devoted to the dripping regime considers the case of constant flow rate. Different criteria have been proposed to identify the jetting to dripping transition, such as monitoring the jet length and the volume of the detached drop relative to that of the liquid remanent attached to the nozzle for varying flow rates, until they experience sudden changes, as proposed by Ambravaneswaran *et al.* (2004), or assuming that dripping exists

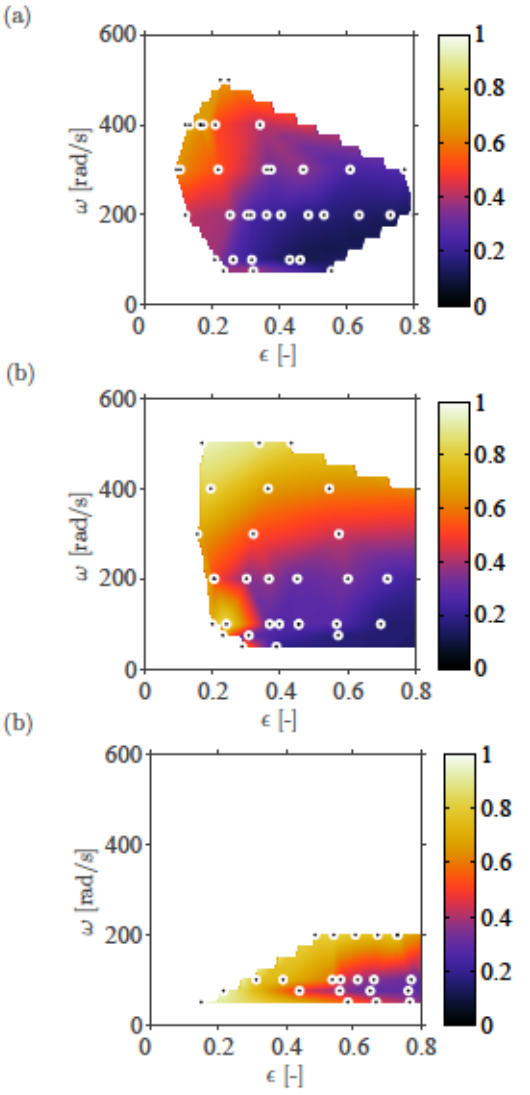

Figure 3.10: Response of jets. Shaded surface plot where colours indicate relative pinching length with respect to its natural counterpart L_b/L_{bN}, for jets stimulated with amplitudes ϵ at different frequencies ω. Points indicate experimental measurements. The jet is established with (a) $\nu = 50$ cSt, $D_i = 4$ mm, $Q = 0.8$ ml/s, (b) $\nu = 50$ cSt, $D_i = 5.5$ mm, $Q = 0.2$ ml/s, and (c) $\nu = 100$ cSt, $D_i = 4$ mm, $Q = 0.2$ ml/s.

when $L_b/R < 20$ proposed for the case of low-viscosity liquids like water, according to Clanet & Lasheras (1999).

To provide a thorough characterization of the oscillatory dripping regime, we measured the evolution of L_b when the jet generated with $\nu = 50$ cSt, $D_i = 4$ mm and $Q = 0.2$ ml/s is stimulated at $\omega = 100$ rad/s with increasing amplitude. As observed in Figure 3.8, the dynamics of the forced jet does not differ much from that of the unforced one for small enough values of epsilon, until a marked decrease in the jet length is observed for $\epsilon \simeq 0.35$. After this transition takes place, the jet length evolves almost periodically with time. As shown in Figure 3.11(a), at the pinch-off instant a short jet with a length between two and three wavelengths remains attached to the injector. The volume of the detached filament is similar to that which remains attached to the injector, since the ligaments comprise a few wavelengths due to the relatively large viscosity of the fluid. For the case $\epsilon = 0.58$, shown in Figure 3.11(b), a ligament with a bulge at its end detaches at the frequency of stimulation, resulting in a a period 1 dripping regime (P1). In contrast with the dripping at constant flow rate (Villermaux *et al.*, 2013), the meniscus that remains attached presents a drop-like structure at its tip. If the amplitude of stimulation is further increased, a period 1 regime with satellite formation (P1S1) takes place, Figure 3.11(c). At this point, oscillations in the curvature of the meniscus become apparent, resulting in a more pronounced influence of the capillary pressure fluctuations at the injector exit.

When ϵ is further increased, flows as the one displayed in Figure 3.12 occur. Although the piston performs a sinusoidal movement of large amplitude, the temporal evolution of the pressure at the measuring chamber has the same frequency as the stimulation but is not sinusoidal. To assess the fluctuations in the flow rate, equation (3.4) is no longer valid. Therefore, we performed an image analysis to compute the temporal evolution of the volume of the pending fluid $V(t)$, and estimated the instantaneous flow rate as $Q_i = (V_i - V_{i-1})/(t_i - t_{i-1})$ where the subindex indicates the frame number in the high-speed movie. As

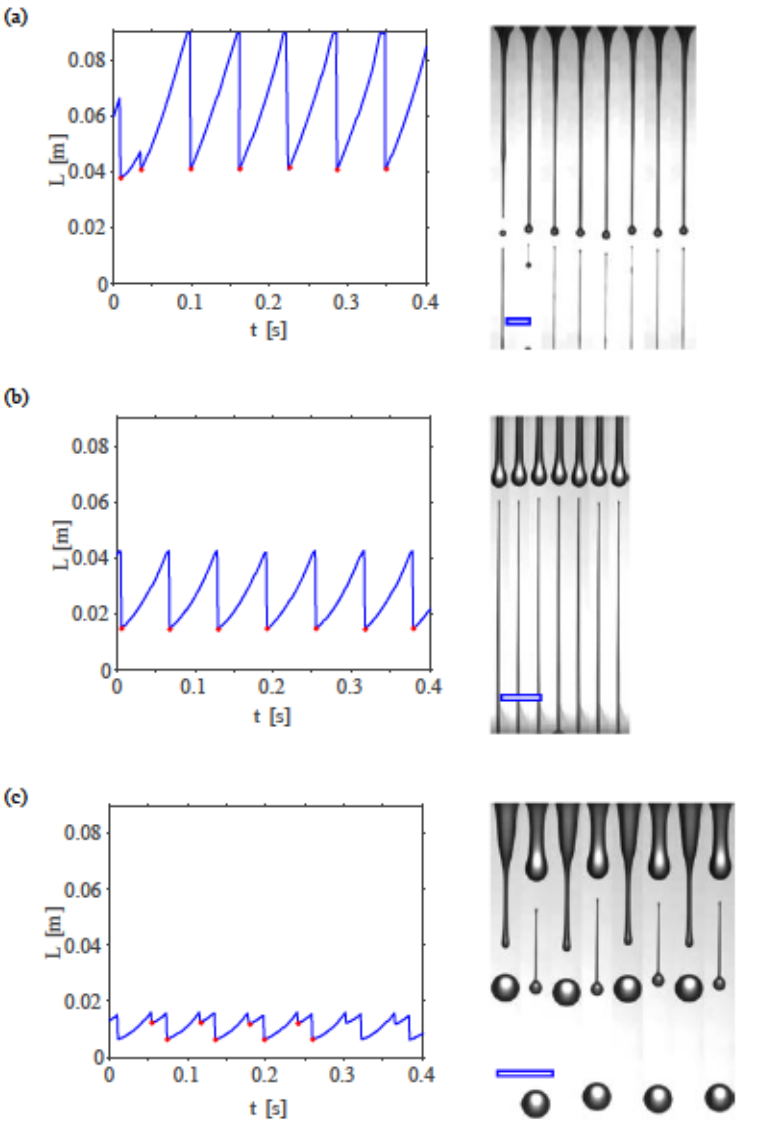

Figure 3.11: Oscillatory dripping of a jet with $\nu = 50$ cSt, $D_i = 4$ mm and $Q = 0.2$ ml/s. Temporal evolution of the jet length $L(t)$ and photographs showing consecutive pinchings marked with dots, for a stimulating frequency $\omega = 100$ rad/s and different perturbation amplitudes, (a) $\epsilon = 0.42$, (b) $\epsilon = 0.59$, and (c) $\epsilon = 0.85$. The scale bar on each set of photographs is 1 cm long.

displayed in Figure 3.12, the flow rate exhibits a periodic behavior and a P2 dripping regime takes place, where identical detachments occur at half the stimulation frequency. For reference, a sinusoidal flow rate $Q_s = Q[1 + \epsilon \sin(\omega t)]$ has been adjusted with $Q = 0.2$ ml/s, $\omega = 100$ rad/s, providing the estimate $\epsilon \sim 1.2$. It can be observed that the experimental flow rate presents a smaller amplitude than the harmonic fit, and a detailed observation of the shape of the meniscus indicates that the measured instantaneous flow rate is higher than expected when its axial curvature is convex ($\mathcal{C}_{axial} < 0$) and larger than the radial one, and lower when the meniscus is rounded ($\mathcal{C}_{axial} > 0$).

Our experiments indicate that a rich variety of dripping dynamics can be induced in forced globally stable jets. Indeed, apart from the already mentioned P1, P2 and P1S1, we have even observed the recently reported P2S2 (Rubio-Rubio, 2016) for $\nu = 50$ cSt, $D_i = 5.5$ mm, $Q = 0.2$ ml/s stimulated with $\omega = 50$ rad/s and $\epsilon = 0.7$. Nevertheless, a detailed parametric analysis of the different oscillatory dripping regimes is left for a future work.

3.3.2 Nonlinear analysis

To study the response of the flow to disturbances, in the first place a steady flow field was obtained for a constant flow rate at the injector and a pinned contact line. This was done resorting to a spectral collocation method (Rubio-Rubio *et al.*, 2013), and the solution was then mapped onto the physical grid. Then, a harmonic perturbation to the outlet speed is applied according to $u(0,t) = U[1 + \epsilon^*(t) \sin(\omega t)]$. The amplitude of the fluctuations $\epsilon^*(t)$ is gradually increased until the target value of ϵ is reached, and then kept constant for several cycles to guarantee a periodic behavior. Specifically, $\epsilon^*(t)$ is a piecewise function prescribing exponential growth of the amplitude during a period of time longer than the advective time it takes for fluid particles to travel the domain, and incidentally manteins the value ϵ for six advective times. These perturbations are convected downstream while their amplitude evolves in space

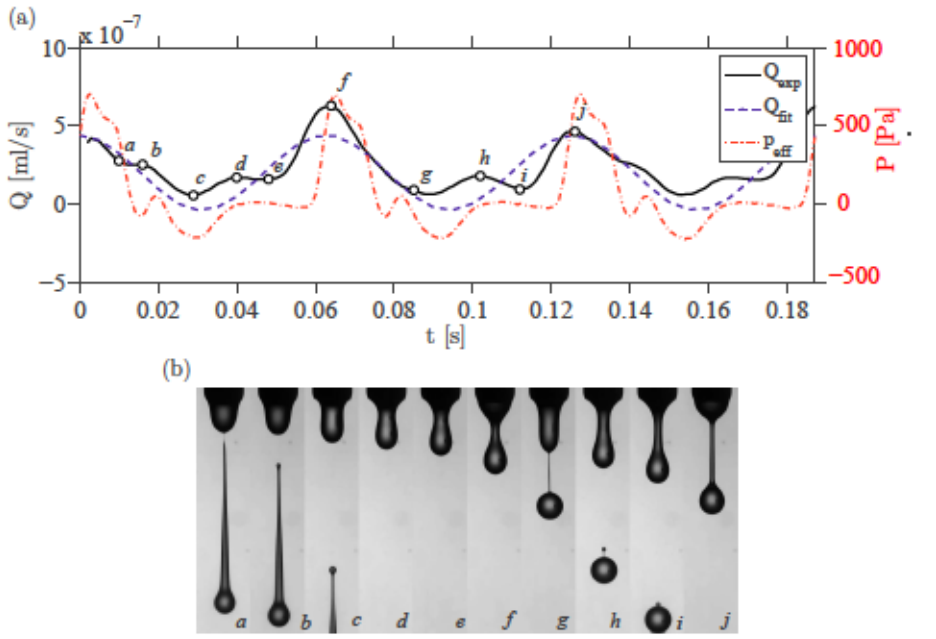

Figure 3.12: Oscillaroty dripping of a jet with $\nu = 50$ cSt, $D_i = 4$ mm and $Q = 0.2$ ml/s, subjected to a stimulating frequency $\omega = 100$ rad/s and perturbation amplitude $\epsilon \sim 1.5$, with a significant contribution of the curvature of the meniscus to the damping and reshaping of the fluctuations. (a) Experimental and harmonic fit of the temporal evolution of the flow rate, Q_{exp} and Q_{fit} respectively, together with the pressure at the sensor chamber p_{eff}. Dots on the experimental curve indicate the corresponding photographs shown below, in (b).

and time. The spatial evolution of the amplitude of disturbances is obtained from the envelope of the radius and speed signals at each axial position.

It was assumed that break-up takes place if the radius of the jet reached a predefined tolerance. In such case, the simulation stopped, the value of ϵ_p^* responsible for the pinching was identified, and a new calculation was launched with a new value $\epsilon < \epsilon_p^*$.

The number of grid points was chosen by succesively increasing the number

of nodes until the obtained solutions converged, finer grids being required for higher wavenumbers and lower initial noise levels. For instance, in simulations where disturbances present $\epsilon \sim \mathcal{O}(10^{-1})$, typical values of the number of nodes are $N = 40L$ when the stimulation frequency is $\omega = 100$ rad/s, where the dimensionless length of the domain L is measured in radius of the injector, and $N = 70L$ when $\omega = 400$ rad/s.

To validate the numerical simulations, we compared several cases with forced experiments and predictions from the linear analysis. Figure 3.13 shows that the structure of the perturbed interface is qualitatively similar to experimental observations, suggesting that this tool will be extremely useful in predicting the nonlinear dynamics of the jet. Moreover, we have checked for different flow configurations that simulations capture the position at which pinching takes place in our experiments, where valleys present the amplitude of the local unperturbed radius.

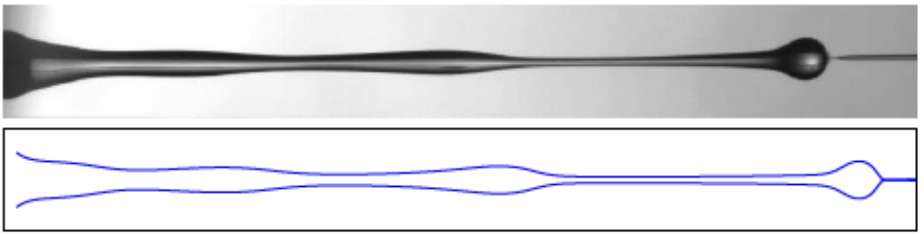

Figure 3.13: Experimental observation (top panel) and numerical calculation (bottom panel) of the break-up of a liquid jet with $\nu = 50$ cSt discharging from an injector with $D_i = 4$ mm at a flow rate $Q = 0.8$ ml/s, subjected to harmonic fluctuations of the injector speed of frequency $\omega = 200$ rad/s and relative amplitude $\epsilon = 0.35$.

Figure 3.14 presents an example of the evolution of the amplitude of disturbances according to the nonlinear model. Close to the injector, their amplitude is small and its evolution exhibits good agreement with the predictions of the linear global frequency response analysis presented in Chapter 2. Therefore,

the nonlinear analysis confirms that the meniscus region damps the amplitude and delays the growth of small disturbances. Downstream, where the relative amplitude of disturbances is not small anymore, the distortion of the jet is no longer harmonic and the amplitude of crests and valleys must be distinguished. Although the disturbance growth follows the tendency predicted by the linear analysis, the latter is unable to capture the dynamics close to break-up. Figure 3.14(d), where the temporal evolution of the jet radius is plotted at a fixed position, shows that that crests present larger amplitude and smaller length than valleys, in contrast with the purely sinusoidal interface assumed in the linear analysis.

3.3.3 Comparison and discussion

In our forced experiments, the amplitude of the perturbed speed at the injector is relatively large, $\epsilon > 10\%$. Therefore, the effects should be retained in the numerical approach to study the dynamics of these jets. Figure 3.15 presents the pinching length L_b resulting from harmonically stimulating a jet with several speed amplitudes ϵ and frequencies ω. It can be observed that there is a good agreement between the numerical predictions and the experiments for $\omega > 200$ rad/s, for which the jet remains globally stable. However, for $\omega = 50$ and $\omega = 100$ rad/s, the agreement is poor. The sudden decrease of the jet length in these cases indicate the transition from jetting to dripping, as described in the previous section. The numerical model can not capture the latter regime without reconstructing the interface after pinch-off, since it would be necessary to simulate several break-up cycles before a periodic dynamics is established. Moreover, the boundary conditions at the injector outlet are sinusoidal, in contrast with the unharmonic oscillations that are measured for values of ϵ close to unity.

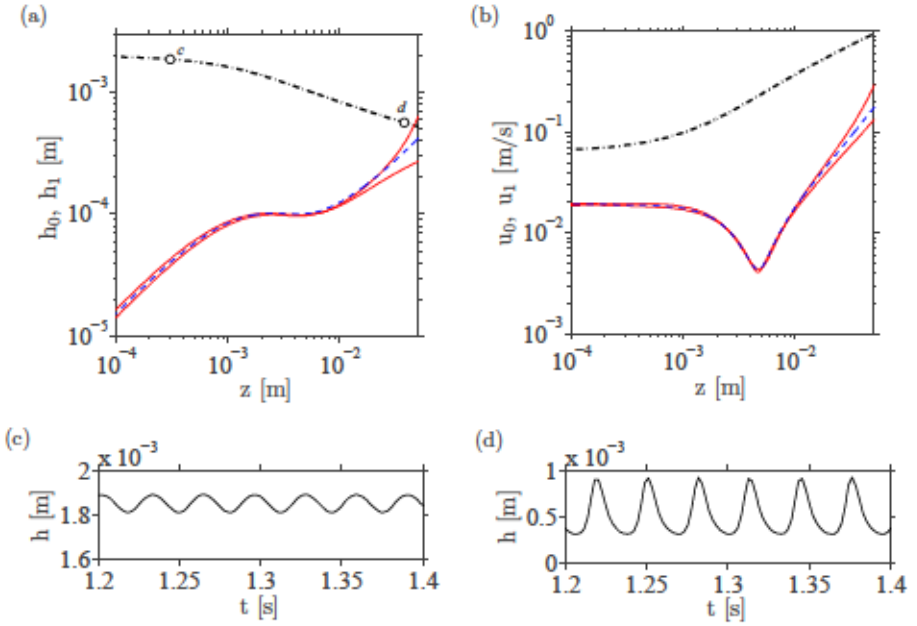

Figure 3.14: Jet with a basic flow h_0, u_0 determined by $\nu = 50$ cSt, $D_i = 4$ mm and $Q = 0.2$ ml/s (dash-dot line in (a) and (b)) stimulated at $\omega = 200$ rad/s with $\epsilon = 0.35$. Amplitude of the radius perturbation h_1 (a) and velocity perturbation u_1 (b) as a function of the axial position z, according to the linear (dashed line) and the nonlinear analysis (solid line). The latter presents two values, for crests and valleys. Insets (c) and (d) show the temporal evolution of the radius $h(t)$ at $z = 0.0003$ m and $z = 0.037$ m, emphasizing the difference between the linear and nonlinear behavior.

The results from numerical simulations were also used to construct contours of constant pinching length, which are displayed in Figure 3.16(a). Recalling that the experimental pinching length for the natural case is $L_{bN} \simeq 0.082$ m, the comparison with Figure 3.9 reveals good agreement, although the numerical results for $\omega < 200$ and ϵ larger than the jetting-dripping transition threshold should be discarded due to the reasons explained above. This information can also be presented as a function $L_b(\omega)$ for fixed values of ϵ, as shown in Figure 3.16, which clearly reveals the existence of an optimal frequency that reduces the pinching length.

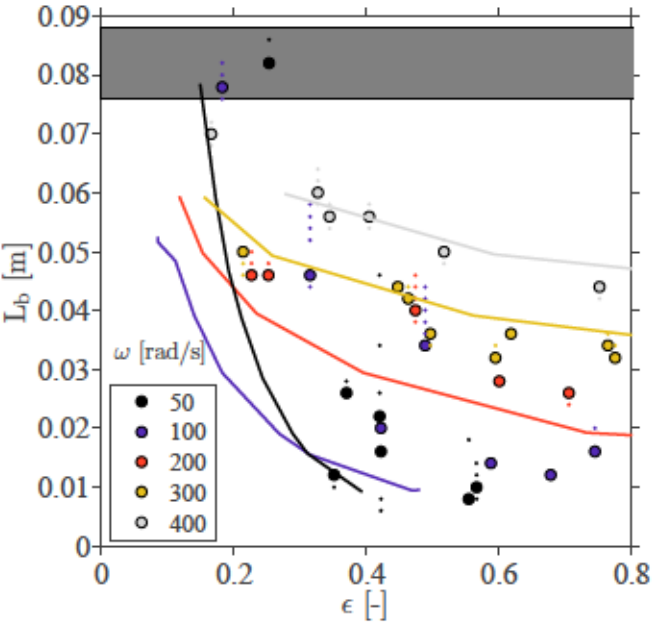

Figure 3.15: Dimensionless pinching length L_b of a jet with $\nu = 50$ cSt, $D_i = 4$ mm and $Q = 0.2$ ml/s, harmonically stimulated with different amplitudes ϵ and frequencies ω. Large dots indicate the most observed value of L_b, while smaller ones account for its dispersion, representing those which are observed at least 50% of that count. Solid lines correspond to the predictions of the 1D numerical simulations. The grayed zone ranging from 0.076 to 0.088 m states pinching lengths observed in natural break-up.

3.4 Conclusions

In this chapter, the nonlinear behavior of stretched liquid jets subjected to harmonic forcing has been numerically and experimentally studied.

Experiments regarding the controlled harmonic stimulation of stretched jets have been carried out, assessing the effect of both the frequency and amplitude of fluctuations of the liquid flow rate. The receptivity of the jet has been

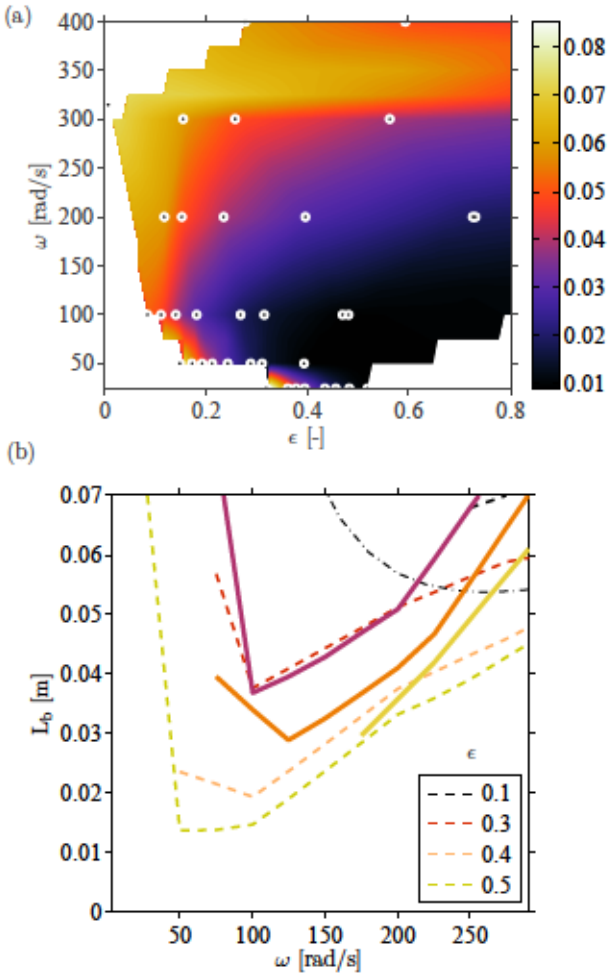

Figure 3.16: Pinching length L_b of a jet with $\nu = 50$ cSt, $D_i = 4$ mm and $Q = 0.2$ ml/s, harmonically stimulated with different amplitudes ϵ and frequencies ω. (a) Isocontours of the pinching length resulting from the numerical simulations. (b) The function $L_b(\omega)$ for fixed values of ϵ, interpolated from experiments (–) and numerical linear (--) and nonlinear (- -) simulations.

evaluated for different mean flow rates, injector sizes and fluid viscosities, and presented in terms of the reduction of the jet length with respect to the natural break-up corresponding to unforced cases. The experiments confirm the

existence of an optimal frequency for which the intact length is minimized, in agreement with the $L_b(\omega, \epsilon)$ dependence revealed by the global frequency response analysis developed in the previous chapter. The measurement of these frequencies also extends the work of Cheong & Howes (2004) by suggesting $\omega_{op} \lesssim 100$ rad/s for four jets under very strong gravitational effects. When the stimulation amplitude is increased for a given frequency, we have observed the transition from the chaotic break-up dynamics similar to the unforced case to a periodic break-up regime, and finally to a new *oscillatory dripping* for frequencies $\omega \leq 100$ rad/s and $\epsilon \geq 0.4$ in the reference case. The latter regime exhibits both simple and complex dynamics and has been described for the first time in the present work.

The forced experiments overcome the limitations identified in the experimental campaign dedicated to the natural break-up, where it was not possible to guarantee that the initial frequency spectrum corresponded to the white noise, as assumed for numerical computations. Therefore, the boundary conditions at the injector needed in the numerical simulations are imposed without uncertainty, allowing the validation of the nonlinear model.

A nonlinear numerical model has been developed and validated with our experiments. To that end, equations (1.9)-(1.11) were integrated resorting to the method of lines, in a formulation inspired by the numerical model by Furlani & Hanchak (2010). The simulations confirm the stabilizing role of the highly-stretched meniscus region, in agreement with the linear analysis, and allows to capture the final stages of the growth of disturbances prior to break-up, accurately predicting the pinching length of strongly stretched globally stable jets.

Future work should focus on improving the numerical code for the nonlinear analysis, extending the physical domain to one evolving in time, to capture the temporal evolution of the tip of the jet and thus capture break-up events. This can be implemented by incorporating an additional term in the numerical method to account for grid advection, and programming appropriate interface

reconstruction algorithms. This improvement will allow the computation of the volume of the detached drops, as well as simulating several break-up events to properly capture the transition and dynamics of the new oscillatory dripping regime.

Regarding the experiments, the volume of the detached filaments and drops should be measured. To that end, if the current experimental facility and equipment is used, the length of the ligaments has to be reduced in order to capture the full axial extension of the detached volume without losing resolution in the radial direction. This can be achieved, for instance, with fluids of lower viscosity than those used in the present work. Also, a more detailed experimental study of the newly found oscillatory dripping regime should be made.

References

AMBRAVANESWARAN, B., SUBRAMANI, H. J., PHILLIPS, S. D. & BASARAN, O. A. 2004 Dripping-jetting transitions in a dripping faucet. *Phys. Rev. Lett.* 93, 034501.

BOGY, D. B. 1979 Drop formation in a circular liquid jet. *Ann. Rev. Fluid Mech.* (11), 207–228.

BOGY, D. B. & TALKE, F. E. 1984 Experimental and theoretical study of wave propagation phenomena in drop-on-demand ink jet devices. *IBM J. Res. Dev.* 28 (3), 314–321.

CHAUDHARY, K. C. & MAXWORTHY, T. 1980*a* The nonlinear instability of a liquid jet. Part 2. Experiments on jet behaviour before drodrop formation. *J. Fluid Mech.* 96, 275–286.

CHAUDHARY, K. C. & MAXWORTHY, T. 1980*b* The nonlinear instability of a liquid jet. Part 3. Experiments on satellite drop formation and control. *J. Fluid Mech.* 96, 287–297.

CHAUDHARY, K. C. & REDEKOPP, L. G. 1980 The nonlinear instability of a liquid jet. Part 1. Theory. *J. Fluid Mech.* 96, 257–274.

CHAUHAN, A., MALDARELLI, C., RUMSCHITZKI, D. & PAPAGEORGIEU, D. 2002 An experimental investigation on the convective instability of a jet. *CES* 58, 2421–2432.

CHEONG, B.S. & HOWES, T. 2004 Capillary jet instability under the influence of gravity. *CES* 59, 2145–2157.

CHUECH, S. G. & YAN, M. 2006 Application of the tvd scheme to the nonlinear instability analysis of a capillary jet. *Int. J. Numer. Meth. Fluids* 52, 1159–1174.

CLANET, C. & LASHERAS, J. C. 1999 Transition from dripping to jetting. *J. Fluid Mech.* 383, 307–326.

DONG, H., CARR, W. W. & MORRIS, J. F. 2006 An experimental study of drop-on-demand drop formation. *Phys. Fluids* 18 (072102).

DONNELLY, J. & GLABERSON, W. 1966 Experiments on the capillary instability of a liquid jet. *Proc. R. Soc. Lond. A Math. Phys. Sci.* 290, 547–556.

FARRASHKHALVAT, M. & MILES, J. P. 2003 *Basic structured grid generation.* Butterworth-Heinemann.

FURLANI, E. P. & HANCHAK, M. S. 2010 Nonlinear analysis of the deformation and breakup of viscous microjets using the method of lines. *Int. J. Numer. Meth. Fluids* .

GARCÍA, F. J., GONZÁLEZ, H., CASTREJÓN-PITA, J. R. & CASTREJÓN-PITA, A. A. 2014 The break-up of harmonically stimulated capillary jets. *App. Phys. Lett.* 105 (094104).

GONZÁLEZ, H. & GARCÍA, F.J. 2009 The measurement of growth rates in capillary jets. *J. Fluid Mech.* 619, 179–212.

HANCHAK, M. S. & FURLANI, E. P. 2010 Modeling drop generation at the microscale. *NSTI Nanotech* 2.

LIN, S. P. & REITZ, R. D. 1998 Drop and spray formation from a liquid jet. *Annu. Rev. Fluid Mech.* (30), 85–105.

MANSOUR, N. N. & LUNDGREN, T. S. 1990 Satellite formation in capillary jet break-up. *Phys. Fluids A* 2 (7), 1141–1144.

MEIER, G.E.A., KLOPPER, A. & GRABITZ, G. 1992 The influence of kinematic waves on jet break down. *Exp. Fluids* (12), 173–180.

MOALLEMI, N. & MEHRAVAN, K. 2016 Breakup of capillary jets with different disturbances. *Phys. Fluids* 28 (012101).

PAN, Y. & SUGA, K. 2006 A numerical study on the breakup process of laminar liquid jets into a gas. *Phys. Fluids* 18 (5), 052101.

RIVERO-RODRÍGUEZ, J. 2016 Estudio numérico de modelos unidimensionales en la interacción fluido-estructura y en la dinámica de chorros y gotas electrificados. PhD thesis, Universidad de Sevilla.

RUBIO-RUBIO, M. 2016 Stretching liquid flows: jets, drops and liquid bridges. PhD thesis, Universidad Carlos III de Madrid.

RUBIO-RUBIO, M., SEVILLA, A. & GORDILLO, J.M. 2013 On the thinnest steady threads obtained by gravitational stretching of capillary jets. *J. Fluid Mech.* 729, 471–483.

RUTLAND, D. F. & JAMESON, G. J. 1971 A non-linear effect in the capillary instability of liquid jets. *J. Fluid Mech.* 46 (2), 267–271.

SAVART, F. 1833 Memoire sur la constitution des veines liquides lancées par des orifices circulaires en mince paroi. *Ann. de Chim.* 53, 337–386.

SCHIESSER, W. E. 1991 *The numerical method of lines. Integration of partial differential equations.* Academic Press, Inc.

Subramani, H. J., Yeoh, H. K., Suryo, R., Xum, Q., Ambravaneswaran, B. & Basaran, O. A. 2006 Simplicity and complexity in a dripping faucet. *Phys. Fluids* 18, 032106.

Villermaux, E., Pistre, V. & Lhuissier, H. 2013 The viscous savart sheet. *J. Fluid Mech.* 730, 607–625.

White, F. M. 2011 *Fluid mechanics*. McGraw-Hill.

Yuen, M. 1968 Non-linear capillary instability of a liquid jet. *J. Fluid Mech.* 33, 151–163.

Zhang, X. & Basaran, O. 1995 An experimental study of dynamics of drop formation. *Phys. Fluids* 7, 1184.

CHAPTER
FOUR

Concluding remarks

4.1 Summary and conclusions

In this Thesis the capillary instability of Newtonian liquid jets stretched by gravity has been studied. The novelty of our work is that we consider flow configurations with a strongly non-parallel region, and assess the stabilizing role of the meniscus using experimental, theoretical and numerical approaches.

In the globally stable jets under study, the strong stretching is attained by setting the control parameters of the flow, namely the viscosity of the working fluid, the injector diameter and the flow rate, close to the critical values at which jetting to dripping transition occurs. We consider two distinct sources of perturbations, the ambient noise and specifically imposed harmonic forcing, and examine the effect of the governing parameters on the evolution of perturbations by performing a parametric sweep.

To carry out the experiments, the design and construction of two experimental facilities has been necessary. Experimental observations provided information regarding the qualitative stability behaviour of jets, and measurements of the intact length and most amplified frequency have been acquired. On the other hand, the characterization of the detached drops, which is of major importance for applications, could not be achieved. In the unforced experiments, the breakup parameters exhibit an irregular temporal evolution and large dispersion. In addition, the passive minimization of disturbances does not seem to guarantee that the jet is subject to white noise. In contrast, in the mechanically forced jets initial disturbances are unambiguously characterized, providing robust ev-

idence against which numerical calculations and stability analyses have been validated. We have shown that appropriate combinations of the stimulation parameters allow the establishment of a periodic controlled break-up, and can result under certain conditions in a new oscillatory dripping regime. The latter exhibits both simple and complex dynamics and has been described for the first time in the present work. In both natural and harmonically stimulated jets, the parametric dependence of the break-up is in qualitative agreement with trends of more slender jets covered by the literature (Nonnenmacher & Piesche, 2004; Cheong & Howes, 2004; Javadi *et al.*, 2013).

The theoretical and numerical approach to the stability of stretched jets presented in this thesis does not rely on classical quasi-parallel assumptions, which are manifestly violated in the meniscus region. Instead, we first developed a global linear frequency response analysis to properly address the strong spatial variations of the flow close to the injector. Then, we also abandoned the assumption of the small amplitude of disturbances and developed a stability analysis where the fully nonlinear one-dimensional equations were integrated using the method of lines.

Regarding the mathematical description of the jet, we have verified that the one-dimensional mass and momentum equations due to García & Castellanos (1994) and Eggers & Dupont (1994), where the full expression for the interfacial curvature is kept, are able to describe the stability of gravitationally stretched liquid jets. Both the linear damping of disturbances in the meniscus region and the nonlinear behavior just before break-up can be captured, while keeping the computational costs to a minimum. Nevertheless, it should be mentioned that this model does not account for velocity profile relaxation.

Numerical calculations revealed the damping of the amplitude and stretching of the wavelength of perturbations in the meniscus region, an effect which was not directly measurable in experiments. From the physical point of view, the frequency selection and stabilizing role of the meniscus was confirmed, and represents the spatial counterpart of the temporal kinematic mechanism described by Tomotika (1936). Since the most amplified disturbance varies with the axial

coordinate, the sensitivity of the pinching length to the amplitude and frequency of stimulation has also been explored. The good agreement between experimental and numerical results gives support to our theory.

4.2 Future work

For completeness, we summarize the main lines of investigation which arise from the present thesis.

Our research was motivated by the fact that stretched jets can produce thin filaments and small drops without resorting to micron-sized injectors that can easily become obtructed. For practical applications, a monodisperse drop production is desirable, hence, drop formation from gravitationally stretched jets should be properly characterized. Regarding the forced experimental campaign, the volume of the detached drops and filaments should be obtained, taking into account the evolution of the latter into satellite drops. Also, the developed nonlinear analysis is an adequate tool to describe break-up and drop formation, and should be improved to incorporate interface reconstruction.

Another phenomenon which would be of interest to consider is the previously unreported oscillatory dripping. Further experimental investigation is required, particularly oriented towards understanding pressure and speed fluctuations due to deformations of the meniscus as well as establishing the critical conditions for the transition in a larger region of parameter space. The enhanced nonlinear model would be a useful tool for this task.

Finally, we have shown that the linear global frequency response analysis (GFRA) presents remarkable computational advantages and versatility. It can be easily extended to other flow configurations and initial disturbances. Provided that an adequate model of the governing equations is available, a GFRA can be implemented to study the stability of stretched jets generated resorting to other techniques, such as flow focusing or electrospinning. This procedure admits a wide range of inputs, including perturbations in the radius and/or speed of the

jet at any axial coordinate with variable spatial distribution.

References

CHEONG, B.S. & HOWES, T. 2004 Capillary jet instability under the influence of gravity. *CES* 59, 2145–2157.

EGGERS, J. & DUPONT, T.F. 1994 Drop formation in a one-dimensional approximation of the navier-stokes equation. *J. Fluid Mech.* 262, 205–222.

GARCÍA, F.J. & CASTELLANOS, A. 1994 One-dimensional models for slender axisymmetric viscous liquid jets. *Phys. Fluids* 6 (8), 2676–2689.

JAVADI, A., EGGERS, J., BONN, D., HABIBI, M. & RIBE, N. M. 2013 Delayed capillary break-up of falling viscous jets. *Phys. Rev. Lett.* 110 (144501).

NONNENMACHER, S. & PIESCHE, M. 2004 Stability behavior of liquid jets under gravity. *Chem. Eng. Technol.* 27 (5), 529–536.

TOMOTIKA, S. 1936 Breaking up of a drop of viscous liquid immersed in another viscous fluid which is extending at a uniform rate. *Proc. Roy. Soc.* 153, 302–318.

Alphabetical list of references

References

Ambravaneswaran, B., Subramani, H. J., Phillips, S. D. & Basaran, O. A. 2004 Dripping-jetting transitions in a dripping faucet. *Phys. Rev. Lett.* 93, 034501.

Ambravaneswaran, B., Wilkes, E. D. & Basaran, O. A. 2002 Drop formation from a capillary tube: Comparison of one-dimensional and two-dimensional analyses and occurrence of satellite drops. *Phys. Fluids* 14, 2606–2621.

Amini, G., Ihme, M. & Dolatabadi, A. 2013 Liquid jet instability under gravity effects. *Phys. Rev. E* 87 (053017).

Bagheri, S., Henningson, D. S., Hoepffner, J. & Schmid, P. J. 2009 Input-output analysis and control design applied to a linear model of spatially developing flows. *Appl. Mech. Rev.* 62 (020803).

Barbagallo, A., Sipp, D. & Schmid, P.J. 2011 Input-output measures for model reduction and closed loop control: application to global modes. *J. Fluid Mech.* 685, 23–53.

Basaran, O. 2002 Small-scale free surface flows with break-up: Drop formation and emerging applications. *AIChE J.* 48 (9), 1842–1847.

Bogy, D. B. 1979 Drop formation in a circular liquid jet. *Ann. Rev. Fluid Mech.* (11), 207–228.

Bogy, D. B. & Talke, F. E. 1984 Experimental and theoretical study of wave propagation phenomena in drop-on-demand ink jet devices. *IBM J. Res. Dev.* 28 (3), 314–321.

BOYD, J. P. 2000 *Chebyshev and Fourier Spectral Methods.* DOVER Publications, Inc.

CANUTO, C., HUSSAINI, M.Y., QUARTERONI, A. & ZANG, T.A. 2007 *Spectral Methods. Evolution to Complex Geometries and Applications to Fluid Dynamics.* Springer.

CHAUDHARY, K. C. & MAXWORTHY, T. 1980*a* The nonlinear instability of a liquid jet. Part 2. Experiments on jet behaviour before drodrop formation. *J. Fluid Mech.* 96, 275–286.

CHAUDHARY, K. C. & MAXWORTHY, T. 1980*b* The nonlinear instability of a liquid jet. Part 3. Experiments on satellite drop formation and control. *J. Fluid Mech.* 96, 287–297.

CHAUDHARY, K. C. & REDEKOPP, L. G. 1980 The nonlinear instability of a liquid jet. Part 1. Theory. *J. Fluid Mech.* 96, 257–274.

CHAUHAN, A., MALDARELLI, C., RUMSCHITZKI, D. & PAPAGEORGIEU, D. 2002 An experimental investigation on the convective instability of a jet. *CES* 58, 2421–2432.

CHEONG, B.S. & HOWES, T. 2004 Capillary jet instability under the influence of gravity. *CES* 59, 2145–2157.

CHOMAZ, J. M. 2005 Global instabilities in spatially developing flows: Non-normality and nonlinearity. *Ann. Rev. Fluid Mech.* 37, 357–392.

CHOMAZ, J. M., HUERRE, P. & REDEKOPP, L. G. 1988 Bifurcations to local and global modes in spatially developing flows. *Pys. Rev. Lett.* 60 (1), 25–28.

CHUECH, S. G. & YAN, M. 2006 Application of the tvd scheme to the nonlinear instability analysis of a capillary jet. *Int. J. Numer. Meth. Fluids* 52, 1159–1174.

CLANET, C. & LASHERAS, J. C. 1999 Transition from dripping to jetting. *J. Fluid Mech.* 383, 307–326.

CLARKE, N.S. 1968 Two-dimensional flow under gravity in a jet of viscous fluid. *J. Fluid Mech.* 31 (part 3), 481–500.

COENEN, W., SEVILLA, A. & SÁNCHEZ, A. L. 2008 Absolute instability of light jets emerging from circular injector tubes. *Phys. Fluids* 20 (074104).

CONSOLI-LIZZI, P. 2012 Análisis de estabilidad espacial de chorros líquidos sometidos a la influencia de la gravedad. Master's thesis, Universidad Carlos III de Madrid.

DONG, H., CARR, W. W. & MORRIS, J. F. 2006 An experimental study of drop-on-demand drop formation. *Phys. Fluids* 18 (072102).

DONNELLY, J. & GLABERSON, W. 1966 Experiments on the capillary instability of a liquid jet. *Proc. R. Soc. Lond. A Math. Phys. Sci.* 290, 547–556.

DOSHI, J. & RENEKER, D. H. 1995 Electrospinning process and applications of electrospun fibers. *J. Electrostatics* 35, 151–160.

DRAZIN, P.G. 2002 *Introduction to hydrodynamic stability*. Cambridge University Press.

EGGERS, J 1993 Universal pinching of 3d axisymmetric free-surface flow. *Phys. Rev. Lett.* 71, 3458.

EGGERS, J 1997 Nonlinear dynamics and breakup of free surface flows. *Rev. Mod. Phys.* 69, 865–929.

EGGERS, J. & DUPONT, T.F. 1994 Drop formation in a one-dimensional approximation of the navier-stokes equation. *J. Fluid Mech.* 262, 205–222.

EGGERS, J. & VILLERMAUX, E. 2008 Physics of liquid jets. *Rep. Prog. Phys.* 71, 036601.

FARRASHKHALVAT, M. & MILES, J. P. 2003 *Basic structured grid generation*. Butterworth-Heinemann.

FRANKEL, I & WEIHS, D. 1985 Stability of a capillary jet with linearly increasing axial velocity (with application to shaped charges). *J. Fluid Mech.* 155, 289–307.

FURLANI, E. P. & HANCHAK, M. S. 2010 Nonlinear analysis of the deformation and breakup of viscous microjets using the method of lines. *Int. J. Numer. Meth. Fluids* .

GAÑÁN-CALVO, A.M. 1998 Generation of steady liquid microthreads and micron-sized monodisperse sprays in gas streams. *Phys. Rev. Lett.* 80 (2), 285–288.

GARCÍA, F.J. & CASTELLANOS, A. 1994 One-dimensional models for slender axisymmetric viscous liquid jets. *Phys. Fluids* 6 (8), 2676–2689.

GARCÍA, F. J., GONZÁLEZ, H., CASTREJÓN-PITA, J. R. & CASTREJÓN-PITA, A. A. 2014 The break-up of harmonically stimulated capillary jets. *App. Phys. Lett.* 105 (094104).

GARNAUD, X., LESSHAFFT, L., SCHMID, P. J. & HUERRE, P. 2012 The preferred mode of incompressible jets. *J. Fluid Mech.* 716, 189–202.

GONZÁLEZ, H. & GARCÍA, F.J. 2009 The measurement of growth rates in capillary jets. *J. Fluid Mech.* 619, 179–212.

GUERRERO, J., GONZÁLEZ, H. & GARCÍA, F.J. 2012 Spatial modes of capillary jets with application to surface stimulation. *J. Fluid Mech.* 702, 354–377.

GUERRERO, J., GONZALEZ, H. & GARCIA, F. J. 2016 Spatial modes in one dimensional models for capillary jets. *Phys. Rev. E* 93 (033102), 1–9.

HANCHAK, M. S. 2009 One dimensional model of thermo-capillary driven liquid jet break-up with drop merging. PhD thesis, University of Dayton.

HANCHAK, M. S. & FURLANI, E. P. 2010 Modeling drop generation at the microscale. *NSTI Nanotech* 2.

HIRSCH, C. 2007 *Numerical computation of internal and external flows.* Butterworth-Heinemann.

JAVADI, A., EGGERS, J., BONN, D., HABIBI, M. & RIBE, N. M. 2013 Delayed capillary break-up of falling viscous jets. *Phys. Rev. Lett.* 110 (144501).

KALAAJI, A., LOPEZ, B., ATTANÉ, P. & SOUCEMARIANADIN, A. 2003 Breakup length of forced liquid jets. *Phys. Fluids* 15 (9).

KAMINSKI, T. S., SCHELERAB, O. & GARSTECKI, P. 2016 Droplet microfluidics for microbiology: techniques, applications and challenges. *Lab Chip* 16, 2168–2187.

KELLER, J.B., RUBINOW, S.I. & TU, Y.O. 1972 Spatial instability of a jet. *Phys. Fluids* 16, 2052–2055.

LE DIZÈS, S. 1997 Global modes in falling capillary jets. *Eur. J. Mech. B/Fluids* 16, 761–778.

LEE, C. H. 1974 Drop formation in a liquid jet. *IBM J. Res. Develop.* 18 (4).

LEIB, S. J. & GOLDSTEIN, M. E. 1986*a* Convective and absolute instability of a viscous liquid jet. *Phys. Fluids* 29 (4), 952–954.

LEIB, S. J. & GOLDSTEIN, M. E. 1986*b* The generation of capillary instabilities on a liquid jet. *J. Fluid Mech.* 168, 479–500.

LIN, S. P. & REITZ, R. D. 1998 Drop and spray formation from a liquid jet. *Annu. Rev. Fluid Mech.* (30), 85–105.

MANSOUR, N. N. & LUNDGREN, T. S. 1990 Satellite formation in capillary jet break-up. *Phys. Fluids A* 2 (7), 1141–1144.

MARMOTTANT, P. & VILLERMAUX, E. 2004 Fragmentation of stretched liquid ligaments. *Phys. Fluids* 16, 2732.

MEIER, G.E.A., KLOPPER, A. & GRABITZ, G. 1992 The influence of kinematic waves on jet break down. *Exp. Fluids* (12), 173–180.

MEIER, G. E. A., LOOSE, S. & STASICKI, B. 1998 Unsteady liquid jets. *Applied Scientific Research* 58, 207–216.

MIKAMI, T., COX, R. G. & MASON, S.G. 1975 Break-up of extending liquid threads. *Int. J. Multiphase Flow* 2, 113–138.

MOALLEMI, N. & MEHRAVAN, K. 2016 Breakup of capillary jets with different disturbances. *Phys. Fluids* 28 (012101).

MONTANERO, J. M., HERRADA, M. A., FERRERA, C., VEGA, E. J. & NÁN CALVO, A. M. GA} 2011 ON THE VALIDITY OF A UNIVERSAL SOLUTION OF VISCOUS CAPILLARY JETS. *Phys. Fluids* 23, 122103.

NONNENMACHER, S. & PIESCHE, M. 2004 STABILITY BEHAVIOR OF LIQUID JETS UNDER GRAVITY. *Chem. Eng. Technol.* 27 (5), 529–536.

PAN, Y. & SUGA, K. 2006 A NUMERICAL STUDY ON THE BREAKUP PROCESS OF LAMINAR LIQUID JETS INTO A GAS. *Phys. Fluids* 18 (5), 052101.

PEARSON, J.R.A. & MATOVICH, M.A. 1969 SPINNING A MOLTEN THREADLINE. *I&EC fundamentals* 8, 605–609.

PLATEAU, J. 1873 *Statique Expérimentale et Théorique des Liquides*. GAUTHIER-VILLARS ET C^{ie}, PARIS.

RAYLEIGH, W. S. 1878 ON THE INSTABILITY OF JETS. *Proc. London Math. Soc.* 10, 4–13.

REDDY, S. C., SCHMID, P. J. & HENNINGSON, D. S. 1993 PSEUDOSPECTRA OF THE ORR-SOMMERFIELD OPERATOR. *SIAM J. Appl. Math.* 53, 15–47.

RIVERO-RODRÍGUEZ, J. 2016 ESTUDIO NUMÉRICO DE MODELOS UNIDIMENSIONALES EN LA INTERACCIÓN FLUIDO-ESTRUCTURA Y EN LA DINÁMICA DE CHORROS Y GOTAS ELECTRIFICADOS. PHD THESIS, UNIVERSIDAD DE SEVILLA.

RUBIO-RUBIO, M. 2016 STRETCHING LIQUID FLOWS: JETS, DROPS AND LIQUID BRIDGES. PHD THESIS, UNIVERSIDAD CARLOS III DE MADRID.

RUBIO-RUBIO, M., SEVILLA, A. & GORDILLO, J.M. 2013 ON THE THINNEST STEADY THREADS OBTAINED BY GRAVITATIONAL STRETCHING OF CAPILLARY JETS. *J. Fluid Mech.* 729, 471–483.

RUTLAND, D. F. & JAMESON, G. J. 1971 A NON-LINEAR EFFECT IN THE CAPILLARY INSTABILITY OF LIQUID JETS. *J. Fluid Mech.* 46 (2), 267–271.

SAVART, F. 1833 MEMOIRE SUR LA CONSTITUTION DES VEINES LIQUIDES LANCÉES PAR DES ORIFICES CIRCULAIRES EN MINCE PAROI. *Ann. de Chim.* 53, 337–386.

SCHIESSER, W. E. 1991 *The numerical method of lines. Integration of partial differential equations*. ACADEMIC PRESS, INC.

SCHMID, P.J. 2007 NONMODAL STABILITY THEORY. *Annu. Rev. Fluid Mech.* 39, 129–162.

SENCHENKO, S. & BOHR, T. 2005 SHAPE AND STABILITY OF A VISCOUS THREAD. *Phys. Rev. E* 71 (056301).

SEVILLA, A 2011 THE EFFECT OF VISCOUS RELAXATION ON THE SPATIOTEMPORAL STABILITY OF CAPILLARY JETS. *J. Fluid Mech.* 684, 204–226.

STERLING, A. M. & SLEICHER, C. A. 1975 THE INSTABILITY OF CAPILLARY JETS. *J. Fluid Mech.* 68, 477–495.

SUBRAMANI, H. J., YEOH, H. K., SURYO, R., XUM, Q., AMBRAVANESWARAN, B. & BASARAN, O. A. 2006 SIMPLICITY AND COMPLEXITY IN A DRIPPING FAUCET. *Phys. Fluids* 18, 032106.

TOMOTIKA, S. 1936 BREAKING UP OF A DROP OF VISCOUS LIQUID IMMERSED IN ANOTHER VISCOUS FLUID WHICH IS EXTENDING AT A UNIFORM RATE. *Proc. Roy. Soc.* 153, 302–318.

TREFETHEN, L. N. 2000 *Spectral methods in MATLAB*. SIAM.

TREFETHEN, L. N., TREFETHEN, A., REDDY, S. C. & DRISCOLL, T. 1993 HYDRODINAMIC STABILITY WITH EIGENVALUES. *Science* 261, 578–584.

Utada, A. S., Chu, L.-Y., Fernandez-Nieves, A., Link, D. R., Holtze, C. & Weitz, D. A. 2007 Dripping, jetting, drops, and wetting: The magic of microfluidics. *MRS Bull.* 32, 702–708.

Van Dyke, M. 1982 *An album of fluid motion*. The parabolic press.

Villermaux, E., Pistre, V. & Lhuissier, H. 2013 The viscous savart sheet. *J. Fluid Mech.* 730, 607–625.

Weideman, J. A. C. & Reddy, S. C. 2000 A matlab differentiation matrix suite. *ACM Transactions on Mathematical Software* 26 (4).

White, F. M. 2011 *Fluid mechanics*. McGraw-Hill.

Yuen, M. 1968 Non-linear capillary instability of a liquid jet. *J. Fluid Mech.* 33, 151–163.

Zhang, X. & Basaran, O. 1995 An experimental study of dynamics of drop formation. *Phys. Fluids* 7, 1184.